Sulfur-bearing species in Sagittarius B2 (Main)

Inaugural Dissertation
zur
Erlangung des Doktorgrades
der Mathematisch-Naturwissenschaftlichen Fakultät
der Universität zu Köln
vorgelegt von

Thanh Liem Ngo
aus Binh Duong, Vietnam

April 02, 2022

Berichterstatter: Prof. Dr. Peter Schilke
Prof. Dr. Stephan Schlemmer

Tag der mündlichen Prüfung: 20^{th} June 2022

Abstract

The search for interstellar molecules and the effect of physical and chemical properties of ISM on the abundance of molecules lie at the heart of Astrochemistry. One essential motivation is to understand how the molecules can be found and the physical properties of the ISM can be affected and traced by the chemistry of the high mass star-forming region. While the number of species detected in the interstellar medium is increasing, we require understanding the chemistry inside the interstellar medium.

In high-mass star-forming regions, the density and temperature of molecules are high, leading to more complex molecules such as methanol, ethanol, Nitrogen-bearing molecules, and Sulfur-bearing molecules. In particular, Sagittarius B2 (Sgr B2) is the most active high mass star-forming region in our Galaxy. Moreover, Sgr B2 is embedded in the Center Molecular Zone (CMZ)region, which leads to Sgr B2 is an excellent target to study the production of complex molecules under extreme physical conditions (high densities, strong radiation field, high cosmic-ray flux) has long been a favorite region to search for new molecules.

In this research, we take advantage of the high angular resolution and high sensitivity of the Atacama Large Millimeter/submillimeter Array (ALMA). In astonishing detail, the observed ALMA data allow us to examine the spatial distribution and structure of molecules in the massive star-forming regions Sgr B2 (Main). I concentrate on sulfur-bearing molecules and derive the physical and chemical properties of the molecules in Sgr B2(Main).

The second part of the thesis analyzes their physical evolution from the cold pre-stellar phase to the warm-up phase. Using the astrochemical code Saptarsy, we simulate the chemical evolution of selected sulfur-bearing molecules in 10^6 years and analyze the impacts of physical conditions of the molecular cloud. We can constrain the physical parameter of the cloud, such as the cosmic-rays, the density distribution of the molecular cloud, the thermal evolution of the cloud, and the minor impacts of the molecules' abundance: the binding energy of species to water ice surfaces, which is the intrinsic parameter of the molecules and impact the gas-grain chemical models.

In addition, among the physical parameters of the cloud that we have constrained, we found that cosmic rays ionization is essential, which significantly influences the cloud chemistry producing the ions H^+,H_3^+,H_2^+,He^+. These ions take part in the formation and destruction processes of COMs.

We ran the astrochemical models and investigated the dependence of the abundances on the cosmic-rays ionization rate inside the molecules cloud. We compared the astrochemical model results to the abundances of molecules derived from the observations toward the hot cores. Our results showed that cosmic-rays ionization rates equal to $1.3 \times 10^{-16} s^{-1}$ match the observed abundance of Sulfur-bearing molecules in Sgr B2(Main).

Zusammenfassung

Die Suche nach interstellaren Molekülen und der Einfluss der physikalischen und chemischen Eigenschaften des Interstellaren Mediums ISM auf die Häufigkeit von Molekülen stehen im Mittelpunkt der Astrochemie. Eine wesentliche Motivation besteht darin, zu verstehen, wie die Moleküle gefunden werden können und wie die physikalischen Eigenschaften des ISM durch die Chemie der massereichen Sternentstehungsregion beeinflusst und nachverfolgt werden können. Während die Zahl der im interstellaren Medium nachgewiesenen Spezies zunimmt, müssen wir die Chemie innerhalb des interstellaren Mediums verstehen.

In massereichen Sternentstehungsgebieten sind die Dichte und Temperatur der Moleküle hoch, was zu komplexeren Molekülen wie Methanol, Ethanol, stickstoffhaltigen Molekülen und schwefelhaltigen Molekülen führt. Insbesondere Sagittarius B2 (Sgr B2) ist das aktivste Sternentstehungsgebiet mit hoher Masse in unserer Galaxie. Darüber hinaus ist Sgr B2 in die Region der Zentralen Molekularen Zone (CMZ) eingebettet, was dazu führt, dass Sgr B2 ein hervorragendes Ziel für die Untersuchung der Produktion komplexer Moleküle unter extremen physikalischen Bedingungen (hohe Dichte, starkes Strahlungsfeld, hoher kosmischer Strahlungsfluss) ist und seit langem eine beliebte Region für die Suche nach neuen Molekülen ist.

Diese Arbeit nutzt die hohe Empfindlichkeit der abbildenden Spektrallinienvermessung, die durch das Atacama Large Millimeter/Sub Millimeter Array (ALMA) ermöglicht wird. Sie ermöglicht es, die räumliche Struktur und den chemischen Gehalt aktiver Sternentstehungsgebiete in Sgr B2 in erstaunlicher Detailtreue zu untersuchen. Ich konzentriere mich auf schwefelhaltige Moleküle in Sgr B2(Main). In einer detaillierten vergleichenden Studie bestimmen wir ihre chemische Zusammensetzung, Dichte, Masse, Temperatur und räumliche Struktur.

Im zweiten Teil der Arbeit analysieren wir ihre physikalische Entwicklung von der kalten prästellaren Phase bis zur Aufwärmphase.

Mit Hilfe des astrochemischen Codes Saptarsy berechnen wir die zeitabhängigen chemischen Häufigkeiten ausgewählter schwefelhaltiger Moleküle und untersuchen die chemischen Reaktionen und Prozesse, die an ihrer Bildung unter den extremen Bedingungen beteiligt sind, die für Sgr B2(M) charakteristisch sind.

Wir können auch die physikalischen Parameter der Wolke einschränken, wie die kosmische Strahlung, die Dichteverteilung der Molekülwolke, die thermische Entwicklung der Wolke und die geringfügigen Auswirkungen der Häufigkeit der Moleküle: die Bindungsenergie von Spezies an Wassereisoberflächen, die der intrinsische Parameter der Moleküle ist und die chemischen Modelle des Gas-korns beeinflusst.

Darüber hinaus haben wir unter den physikalischen Parametern der Wolke, die wir bestimmt haben, herausgefunden, dass die Ionisierung durch kosmische Strahlung eine wesentliche Rolle spielt, die die Chemie der Wolke erheblich beeinflusst und die Ionen H^+,H_3^+,H_2^+,He^+ erzeugt. Diese Ionen sind an den Entstehungs- und Zerstörungsprozessen der COMs beteiligt.

Wir führten die astrochemischen Modelle durch und untersuchten die Abhängigkeit der Häufigkeiten von der Ionisierungsrate der kosmischen Strahlung innerhalb der Molekülwolke. Wir verglichen die Ergebnisse der astrochemischen Modelle mit den Häufigkeiten der Moleküle, die aus den Beobachtungen in Richtung der heißen Kerne abgeleitet wurden. Unsere Ergebnisse zeigen, dass die Ionisierungsrate der kosmischen Strahlung $1,3 \times 10^{-16} s^{-1}$ mit der beobachteten Häufigkeit von schwefelhaltigen Molekülen in Sgr B2(Main) übereinstimmen.

Contents

List of Figures

List of Tables

Part I

Introduction

Chapter 1

Interstellar medium and the formation of stars

1.1 Interstellar medium (ISM) in the Milky Way

The interstellar medium includes:

- Matter (gas, dust, and cosmic rays).
- Electromagnetic radiation.
- A gravitational field.
- A magnetic field in the interstellar space in a galaxy.

The matter in ISM includes ions, atoms, molecules in the gas phase, and dust particles. The interstellar medium consists of 99% of gas, including any gas such as ions, atoms, molecules, and 1% of the dust particles. The interstellar gas consists of 91% of hydrogen, 8.9% of helium, and 0.1% of atoms of elements heavier than hydrogen and helium. Hydrogen and helium are mainly the results of Big Bang nucleosynthesis, while the heavier elements in ISM are primarily the result of enrichment during stellar evolution. The interstellar dust particles are tiny grains, which are less than a micron in size, mainly consisting of silicates, carbon, ice, and iron compounds. Because the dust particles' size is approximately the wavelength of blue light, those dust particles can effectively block out visible light. If the dust is dense enough, the light could be blocked entirely by dust, and the cloud would show up as a dark cloud.

ISM plays an essential role in astrophysics mainly because of its mediating role between the star and galactic scales. Stars form in the ISM's densest regions, eventually contributing to molecular clouds and adding matter and energy to the ISM through planetary nebulae, stellar winds, outflows, UV radiation, and supernovas. This mutual interaction between stars and the ISM helps determine the rate at which a galaxy depletes its gas content and the life span of active star formation. The interstellar medium consists of many phases distinguished by matter, ions, atoms, or molecules and the temperature and density of matter.

Interstellar matter in the Galaxy concentrate in clumps and filaments of various scales called clouds. The interstellar medium's clouds are divided into diffuse atomic clouds and molecular clouds, which differ in their physical conditions.(Yamamoto, 2017)

1.1.1 Diffuse Clouds

Diffuse atomic hydrogen clouds are a significant repository of gas in the ISM and play an essential role in galaxies' ecology. The diffuse atomic clouds are characterized by relatively low densities ($\sim$ 50 cm^{-3}), moderate temperatures ($\sim$ 80 K), column densities up to 5×10^{21} H-nuclei cm^{-2}, and low molecular abundances ($n_{\mathrm{H}_2}/n_{\mathrm{H}} < 1$). The typical sizes of diffuse clouds are ~ 0.5 pc, masses are $\sim 3M_\odot$, and column densities are $\sim 10^{20}$ cm^{-2}. The density of H_2 (or H) of diffuse cloud is from 10 cm^{-3} to 100 cm^{-3}, and the standard visual extinction A_v of the cloud is a few magnitudes, so the interstellar UV radiation penetrates deeply into the cloud. (Yamamoto, 2017)

1.1.2 Molecular clouds

Molecular clouds are the place where protostars form. The H_2 density ranges from $10^2 - 10^6$ cm^{-3} and the cloud size is from 0.1 to 10 pc. The H_2 density of the dense core, which is the dense part of a molecular cloud, is higher than 10^4 cm^{-3}. (Yamamoto, 2017)

1.2 Star formation

The stars are formed by the gravitational compression of molecular cloud cores. The protostars will evolve into main-sequence stars, and planetary systems are also created.

There are two kinds of star: high-mass star and low-mass star.

- low-mass $M_* \leq 8M_\odot$
- high-mass ($> 8M_\odot$) and luminosity $\geq 10^3 L_\odot$

The formation processes of low-mass stars: It takes $10^7 - 10^8$ years for low-mass protostars to evolve into main-sequence stars.

The high-mass protostars evolve much faster ($\sim 10^5$ years). Because of the high luminosity of high-mass protostars, they have extreme physical and chemical properties, which highly affect their parent cores. High-mass stars radiate intense UV radiation, ionizing the surrounding gas to form HII regions, which are not created in low-mass star-forming areas.

1.2.1 Low-mass Star formation

Astrophysics divided low-mass star formation into four observationally defined 'Classes,' corresponding to evolutionary stages initially based on the Spectral Energy Distribution (SED) classification (Evans et al., 2009).

- Class 0 object

  Introduced as an early protostar stage, the parent molecular cloud fragments from gravity or external forces and forms a first protostar core.

- Class I object

Supported by turbulent motion (begun by fall on filaments, collapsing dense cores, expansion around young stars) and magnetic fields. The core starts to collapse in a free-fall scenario into a protostar at the center.

- Class II object

  The H_2 density and the temperature at the center of the cloud start to increase. The star formation process continues; the disk of gas and dust forms around the protostar within the core. The protostar is growing by accreting gas. Then an outflow begins from the protostellar, which is perpendicular to the protostar disk.

- Class III object

  Finally, hydrogen starts to fuse in the star's core. The planetary system is formed around the host star after the remaining disk has been primarily dispersed, ending the protostar phase and beginning the main-sequence star.

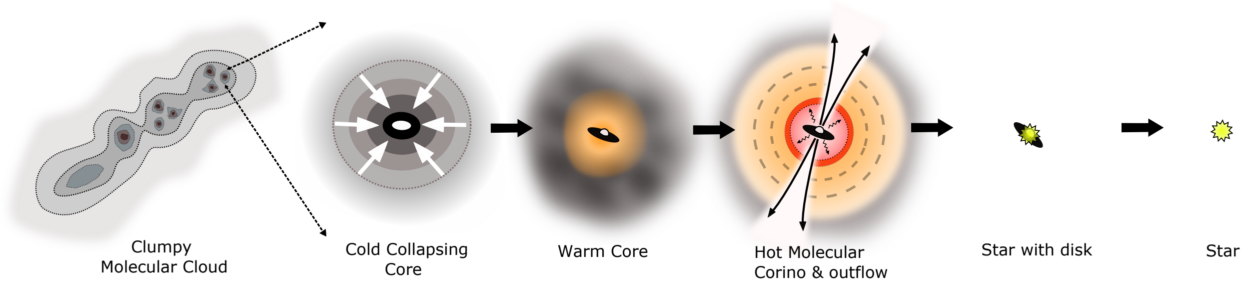

Figure 1.1: Low-mass star formation. Credit: Original cartoon by Cormac Purcell, modified by Adam Ginsburg.

1.2.2 High-mass star formation

According to the initial mass function (IMF) of stars (Kroupa, 2001), the number of low-mass stars is much larger than the number of high mass stars consisting of galaxies. However, the high-mass stars dominate the luminosity of galaxies, which plays an essential role in the Galaxy's physical, chemical, and morphological evolution.

The details of high-mass stars' evolution are not well understood, so there are many controversial about the formation of high-mass stars.

There are two main theories: Monolithic collapse and Competitive accretion

1. Monolithic collapse: high-mass stars are formed through the gravitational collapse of giant molecular clouds.(McKee & Tan, 2003)

2. Competitive accretion in embedded stellar clusters. The stellar embryos form within a low-mass protostar cluster in a protocluster cloud. In the beginning, the low-mass protostars are created at the center of the stellar cluster, and then the core gathers the material inside the cloud to become more and more massive. (Bonnell, Bate, Clarke, & Pringle, 2001)

The massive stars formation can be divided into four evolutionary stages (Gerner et al., 2014):

1. The first stage corresponds to infrared dark clouds (IRDCs). These clouds are regions of high extinction viewed against the bright diffuse mid-infrared galactic background: the molecular material in these regions is cold (25 K), dense (4×10^5 cm^{-3}).
2. The second stage is referred to as a high mass proto- stellar object (HMPO) which is still IR dark but already contains signatures of star formation, which already shows internal emission sources, such as masers.
3. The third stage referred to hot molecular core phase (HMC). The protostar at the central heats the surrounding environment. The material in the surrounding is strongly irradiated and warmed, evaporating molecular-rich ices and giving rise to molecular complexity in the gas.
4. In the final stage, the Ultra-compact HII (UCHII) regions are formed. The embedded protostars radiate UV radiations, which ionize surrounding gas. Many complex organic molecules formed in the last stage are no longer detected in these objects because they are destroyed by ionizing radiation.

The evolution of high mass stars is based on the temperature rising from IRDCs to HMPOs to UCHII regions.

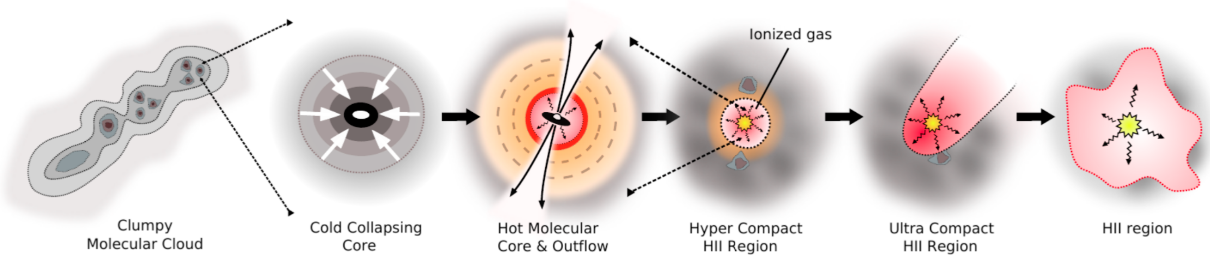

Figure 1.2: The evolutionary stages of massive stars formation. Credit: Original cartoon by Cormac Purcell, modified by Adam Ginsburg.

Chemical processes

High mass star-forming regions have more complex molecules because they have high density, high-temperature structures, high luminosity (HII region), and complex structures, producing complex molecules. Therefore, the chemical properties of the massive mass star-forming region are usually characterized by abundances of complex organic molecules (COMs) such as CH_3CH_2OH, CH_3OH, CH_3CH_2CN, and $CH_3{-}O{-}CH_3$. Moreover, the extreme conditions in massive star formation regions also impact the sulfur-bearing molecules' abundance, such as SO, SO_2, OCS, CS, and H_2CS which are mainly focused in this research. (Yamamoto, 2017)

1.3 Chemistry in ISM

Molecular clouds are characterized by low temperatures (10 - 100 K) and low density ($10 - 10^7$ cm^{-3}). Because of the low density, only 2-body reactions can happen, and then energy and momentum conservation demand that also two bodies come out (1.1).

$$\mathrm{A + B \longrightarrow C + D} \tag{1.1}$$

The chemical reaction in ISM can be classified into bond formation, bond breaking, and rearrangement reactions (Vallance, 2017):

Bond formation :	Radiative association (neutral or ionic)	$\mathrm{A + B \longrightarrow AB + h\nu}$
	Associative detachment	$\mathrm{A + B \longrightarrow AB + e}$
	Dust – grain – catalysed reaction(neutral or ionic)	$\mathrm{A + B + grain \longrightarrow AB + grain}$
Bond breaking :	Photodissociation	$\mathrm{AB + h\nu \longrightarrow A + B}$
	Collisional dissociation (neutral or ionic)	$\mathrm{AB + M \longrightarrow A + B + M}$
	Dissociative recombination	$\mathrm{AB^+ + e^- \longrightarrow A + B}$
Rearrangement :	Ion – molecule reaction	$\mathrm{A^+ + BC \longrightarrow AB^+ + C}$
	Charge transfer	$\mathrm{A^+ + B \longrightarrow A + B^+}$
	Neutral reaction	$\mathrm{A + BC \longrightarrow AB + C}$

1.4 Sulfur-bearing molecules in ISM

Sulfur-bearing molecules: sulfur dioxide (SO_2), sulfur monoxide (SO), carbonyl sulfide (OCS), carbon monosulfide (CS), hydrogen sulfide (H_2S), and thioformaldehyde (H_2CS) have been detected in the interstellar environment, such as infrared dark clouds, hot molecular cores, and shocked regions. The relative abundance ratios of Sulfur-bearing molecules strongly depend on temperature and density. In previous studies, researchers have used sulfur-bearing molecules as the chemical clock to understand molecular clouds' chemical and physical properties.

- **Infrared dark clouds (cold collapse phase)**

  With their low temperatures and high densities, the cloud has been recognized as massive stars forming regions.

  There were many observations detecting and tracing the S-bearing molecules in dark cloud. According to the previous research ((Ragan et al., 2006)) found that CS is a common molecule in IRDCs and the CS emissions in clouds that may be the precursor sites of intermediate-mass and high-mass star formation. (Vasyunina et al., 2011) found weak ^{13}CS(2-1) (and other COMs) emissions in IRDCs, and they explained that the cause of the low detection rate of ^{13}CS(2-1) is the low ratio of ^{13}CS/CS (equal to 50).

- **Hot molecular cores (warm-up phase)**

  (Blake, Sutton, Masson, & Phillips, 1987) analyzed molecules in hot cores in clouds like OMC-1, Sgr B2, and TMC-1. They derived column density and temperature of molecules which include Sulfur-bearing (SO_2, SO, CS, OCS) and compared the results with astrochemistry models. The models simulate the gas-phase and grain-surface process in the hot core.

  The chemistry process produces SO, CS, OCS from grain-mantle evaporation into warm gas in hot cores, which can achieve significant SO_2, H_2CS abundances. The model predictions can logically explain the S-bearing molecule abundances observed in hot cores such as the Orion Hot Core, the Orion Compact Ridge, and Sgr B2(N). (Charnley, 1997)

(Garrod, Weaver, & Herbst, 2008) developed the warm-up model to analyze the complex molecules. This model can explain the observed abundances and temperatures of complex organic molecules. By including the gas phase and grain surface chemistry and a two-stage physical model of the cold-collapse and warm-up phases, they could explore the chemical complexity observed in low-mass to high-mass star-forming regions. They investigated the abundance of numerous COMs molecules such as methanol (CH_3OH) formaldehyde (CH_3CHO) under the physical conditions in hot-core and compared the model and observations results. In our research, we use the astrochemical models with the enhanced multilayer gas-grain models to investigate the chemistry of S-bearing molecules in Sgr B2(Main).

- **Shock regions**

  Sulfur-bearing molecules exist in the gas phase and on the surface of the grains. These molecules in the gas phase can be derived and analyzed through observation. However, the sulfur molecules locked onto dust grains is unknown. To understand the ratio of S-bearing molecules in the gas and on grain, researchers can base the short timescales of shocks in young molecular outflows, and they could derive the main form of sulfur on the grains.

  The chemistry of sulfur-bearing species in shocks that propagate in dense interstellar clouds has been considered by several authors. In the first phases of high mass star formation, the outflowing gas strikes the ambient material, often causing molecular shocks. These shocks can partially destroy molecules, usually frozen onto the grain surfaces, which can be released into the gas phase. The interaction of shocks, which increases the temperature of the neutral species, can initiate some critical neutral-neutral chemical reactions possessing high activation energies. (Pineau des Forêts, Roueff, Schilke, & Flower, 1993)

  For instance:

$$\mathrm{S} + \mathrm{H_2} \longrightarrow \mathrm{SH} + \mathrm{H}$$

$$\mathrm{SH} + \mathrm{H_2} \longrightarrow \mathrm{H_2S} + \mathrm{H}$$

  Depending on the shock velocity, magnetic field, and pre-shock density, the shocks may dissociate the existing molecules (J-type shocks) or form many molecules in the "gently" shocked gas (C-type shocks)

1.4.1 Cosmic rays

Cosmic rays mainly consist of very-high-energy protons (MeV-TeV), primarily originate from the supernova explosions of high-mass stars (Ackermann et al., 2013) or accelerated through shock processes (Padovani, Marcowith, Hennebelle, & Ferrière, 2016) within protostellar sources. In the dense parts of the ISM, interstellar UV radiation becomes shielded at the center of the cloud. However, cosmic-ray particles can penetrate the center of the cloud, which is the primary source of ionization. They may ionize H, H_2, and He, which are mainly affected due to their high abundances in the ISM to create H^+, H_2^+ and

He^+. The molecular hydrogen ion H_2^+ react with the hydrogen molecule H_2 to form H_3^+. H_3^+ molecule is a stable triangular ion protonated dihydrogen that has low proton affinity. So H_3^+ is capable of donating a proton to many other species, for example:

$$H_3^+ + O \longrightarrow OH^+ + H_2 \tag{1.2}$$

Chapter 2

Sagittarius B2

2.1 Physical structure of Sagittarius B2

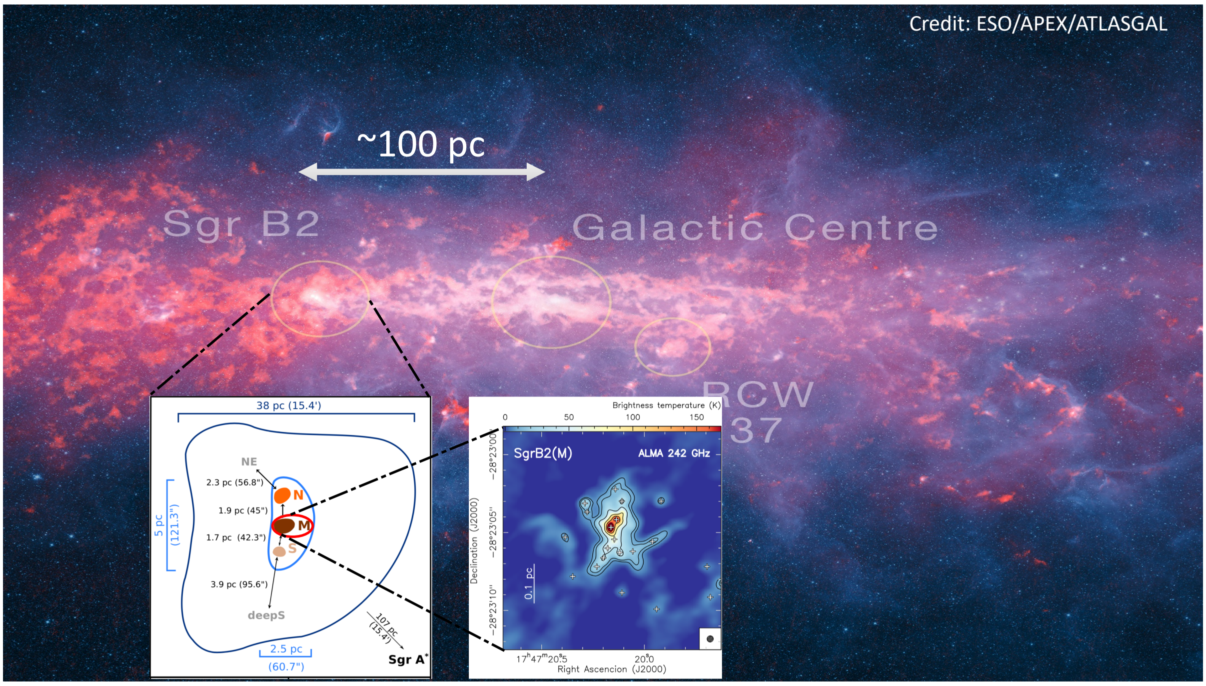

Figure 2.1: The star-forming complex Sagittarius B2 is embedded inside the Central Molecular Zone of the Milky Way. The background shows the southern plane of the Milky Way from the ATLASGAL survey. Within the cloud, there are three main spots of star formation Sgr B2(M), Sgr B2(N), and SgrB2(S), which were shown in the sketch of the Sgr B2 region (Schmiedeke et al., 2016). The SgrB2 (M) star-forming region is the target of my analysis. The ALMA 242 GHz continuum emission toward Sgr B2(M) was produced by (Sánchez-Monge et al., 2017).

The complex molecular cloud Sagittarius B2 (Sgr B2) is one of our Galaxy's most massive molecular clouds. The first observation of Sgr B2 (Martin & Downes, 1972) used Cambridge One-Mile Telescope, and the cloud was observed in the 2.7 and 5 GHz frequency range. The research found high mass stars (O stars) were forming in the cloud, and the compact ionized regions in Sgr B2 were more significant than in Orion nebular. Then (Benson & Johnston, 1984) observed Sgr B2's continuum emission with an angular resolution exceeding one arcsec. Furthermore, they found that Sgr B2 had three emission centers containing twelve individual compact HII regions.

Sagittarius B2 is the perfect targets for studying massive star formation under extreme conditions in our local environment. Due to its density structure, it was suggested that Sgr B2 consists of three different parts:

1. A low-density envelope with density $n_{\mathrm{H}_2} \sim 10^3\ \mathrm{cm}^{-3}$,
2. Medium density regions, which extends around local hot molecular nuclei, with density n_{H_2} is $\sim 10^5\ \mathrm{cm}^{-3}$,
3. The most compact and densest regions, which have density $n_{\mathrm{H}_2} \sim 10^7\ \mathrm{cm}^{-3}$.

There are two sites of active star formation in Sgr B2: Sgr B2 (Main) and Sgr B2 (North) embedded at the center of the cloud Sgr B2, the position of Sgr B2 (Main) and Sgr B2 (North) are show in figure 2.2. The star formation regions were observed and analyzed by researcher (Mehringer, Palmer, Goss, & Yusef-Zadeh, 1993); (Martín-Pintado, Gaume, Rodríguez-Fernández, De Vicente, & Wilson, 1999); (McGrath, Goss, & De Pree, 2004); (Caswell et al., 2010); (Rolffs et al., 2010); (Comito et al., 2010). The sizes of Sgr B2 (M) and Sgr B2 (N) are two pc in radii. They contain > 70 high massive stars and are the best place for searching for new chemical species in high mass star-forming regions (Schmiedeke et al., 2016). The differences between Sgr B2 (N) and Sgr B2 (M) can be attributed to different physical conditions and chemical histories or evolutionary effects in kinematics and chemistry.

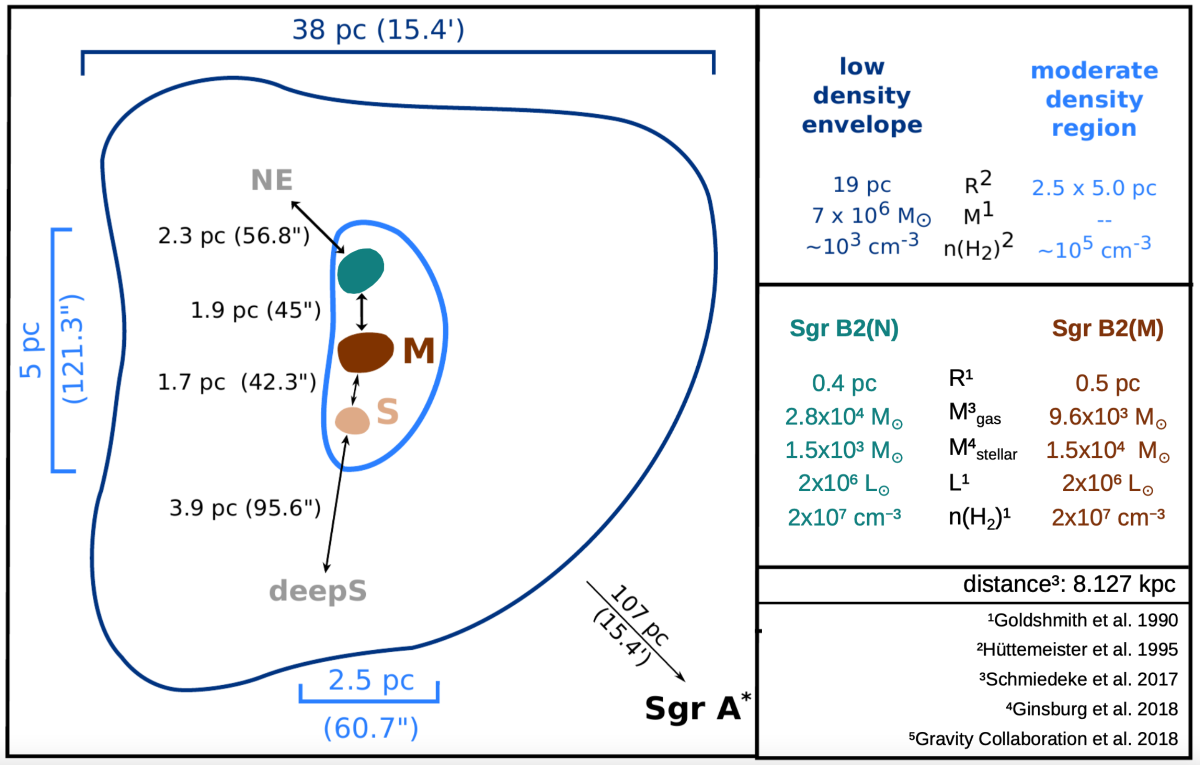

low density envelope		moderate density region
19 pc	R^2	2.5 x 5.0 pc
$7 \times 10^6\ M_\odot$	M^1	--
$\sim 10^3\ \mathrm{cm}^{-3}$	$n(H_2)^2$	$\sim 10^5\ \mathrm{cm}^{-3}$

Sgr B2(N)		Sgr B2(M)
0.4 pc	R^1	0.5 pc
$2.8 \times 10^4\ M_\odot$	M^3_{gas}	$9.6 \times 10^3\ M_\odot$
$1.5 \times 10^3\ M_\odot$	M^4_{stellar}	$1.5 \times 10^4\ M_\odot$
$2 \times 10^6\ L_\odot$	L^1	$2 \times 10^6\ L_\odot$
$2 \times 10^7\ \mathrm{cm}^{-3}$	$n(H_2)^1$	$2 \times 10^7\ \mathrm{cm}^{-3}$

distance[3]: 8.127 kpc

[1]Goldshmith et al. 1990
[2]Hüttemeister et al. 1995
[3]Schmiedeke et al. 2017
[4]Ginsburg et al. 2018
[5]Gravity Collaboration et al. 2018

Figure 2.2: Sketch of the Sgr B2 region, based on (Hüttemeister et al., 1995), adapted from (Schmiedeke et al., 2016) and finally updated.

Due to their extraordinary properties, SgrB2 (M) and SgrB2 (N) were targeted by numerous spectral line surveys with instruments such as the IRAM 30m telescope, ALMA, and the Herschel space observatory.

Previously, researchers were trying to understand the physical and chemical structure of Sgr B2 (North) and Sgr B2 (Main). By using the Submillimeter Array (SMA) with a high spatial resolution, submillimeter (Qin et al., 2011a) observed the continuum of the Sagittarius B2 cloud. They found multiple compact sources in Sgr B2(N) and Sgr B2(M), and the column densities of the two sources are above 10^{25} cm^{-2}. Moreover, they found that Sgr B2(M) is fragmented, and Sgr B2 (N) is a monolithic structure. Thus, following the theory of molecular evolution, they believe that the Sgr B2 cloud forms in a homogeneous core at the beginning, and then after a time, it was fragmented its structure. Moreover, the Heterodyne Instrument for the Far-Infrared (HIFI) instrument on the Herschel Space Observatory is also used to observe and study chemistry, molecules abundance, and physical structure of SgrB2 (North) and SgrB2 (Main). (Neill et al., 2014) observed the Sagittarius B2 (N) cloud, which is the first high spectral resolution look at the source in a frequency range (480–1910 GHz). They found significantly higher abundances of amine and amide-bearing molecules toward Sgr B2(N) than Orion KL and lower abundances of some complex oxygen-bearing molecules. Furthermore, (Möller et al., 2021) used the (HIFI) instrument to observe the Sagittarius B2 (M) cloud in a spectral line survey from 480 to 1907 GHz at a spectral resolution of 1.1 MHz. They simulated the molecular emission from the submillimeter to the far-infrared using the XCLASS program, which assumes local thermodynamic equilibrium to get the temperature and velocity distributions are analyzed and the derived abundances of each molecule. They compared those results with the results of Sgr B2(N) from a similar HIFI survey.(Neill et al., 2014). They found less complex molecules but more simple molecules such as CN, CCH, SO, and SO_2. However, some sulfur-bearing molecules such as H_2CS, CS, NS, and OCS are more abundant in Sgr B2 (N) than Sgr B2 (M).

In addition, the IRAM 30 m telescope was also used to observe and analyze SgrB2. For instance, (Belloche, Müller, Menten, Schilke, & Comito, 2013) used the IRAM 30 m telescope to survey complex organic molecules (COMs) by using spectral lines toward two high-mass stars, forming region Sgr B2(N) and (M).

Moreover, with the Atacama Large Millimeter/submillimeter Array (ALMA), the main Array consists of 50 12 m antennas and provides maximum baselines up to 16 km. The powerful interferometry array can observe the astronomical object in high angular resolution, helping us to understand more about the physical and chemical properties of the interstellar medium (ISM). (Bonfand, Belloche, Menten, Garrod, & Müller, 2017) used (ALMA) to characterize the hot core population in Sgr B2(N) and analyze the star formation in the high star-forming region, and (Xue, Remijan, Burkhardt, & Herbst, 2019) used the high spatial-resolution ALMA data to study spatial distribution the $C_2H_4O_2$ such as $HCOOCH_3$, CH_2OHCHO, and CH_3COOH in SgrB2 (North).

2.2 ALMA observations

In my thesis, I used observation data from ALMA (The Atacama Large Millimeter/submillimeter Array), which the telescope array is located at 5000 m altitude on the Chajnantor plateau in the Atacama desert in Chile. The main Array consists of 50 antennas with 12m diameter each, which provide maximum baselines up to 16 km. The frequency range covered by ALMA is divided into several receiver bands, currently starting at wavelengths of 3.6 mm (band 3: 84 GHz - 116 GHz) and ending at 0.3 mm (band 10: 787 GHz - 950 GHz).

Figure 2.3: The Atacama Large Millimeter/submillimeter Array (ALMA). Credit: ESO/C. Malin.

ALMA comprises many interferometer telescopes, and those antennas can work together and be simulated as a single giant telescope. The array telescope can provide higher angular resolution images of astronomical objects. Those high-angle images can help astronomers analyze the physical and chemical properties of the stars' formation and planetary formation in the Universe.

SgrB2 includes two high-mass stars forming region Main and North was observed by ALMA (Atacama Large Millimeter/submillimeter Array during Cycle 2 led by the PI P. Schilke (project number 2013.1.00332.S) in June 2014 June 2015. The observation used 34-36 antennas with baselines ranging from 30 to 650 m, which provided a high angular resolution of 0.3-0.7 (corresponding to $\sim$ 3300 AU). The observations achieved the spectral, which covered the whole ALMA band 6 (frequency range from 211 GHz to 275 GHz) and provided a resolution of 0.5-0.7 km/s across the whole frequency band. Sgr B2 (Main) source was observed with phase center at $\alpha(\mathrm{J2000}) = 17^{\mathrm{h}}47^{\mathrm{m}}20^{\mathrm{s}}.157$, $\delta(\mathrm{J2000}) = -28^{\circ}23'04''.53$.

The calibration and imaging processes were accomplished by using CASA version 4.4.0. The SgrB2 (M) images were reconstructed by using a standard Gaussian beam size of $0''.4$. The observations, calibration, and imaging are presented in (Sánchez-Monge et al., 2017).

The continuum emission towards Sgr B2(M) and Sgr B2(N) of this dataset has already been analyzed and published (see (Sánchez-Monge et al., 2017)). The physical structure and kinematic properties of Sgr B2(N) was characterized by using various molecules

(Schwörer et al., 2019).

Continuing the series "The physical and chemical structure of Sagittarius B2", I analyze the data to understand the physical properties and S-bearing molecules spatial distribution, which are highly abundant in Sgr B2 (Main).

Chapter 3

Goals and outline of the thesis

In the previous sections, high-mass stars are essential ingredients of our Galaxy. It is necessary to enhance our understanding of their formation the physical and chemical properties of the high-mass star-forming regions. In particular, we want to constrain better the physical and chemical processes during the stages of the high-mass star formation.

With the radio interferometry telescope's high sensitivity and high angular resolution, we can observe more detail of molecular cloud and overcome the observational difficulties that limit the study of high-mass star-forming regions. Furthermore, with the assistance of computers and softwares, we can derive the physical and chemical properties of the molecules cloud, and the astrochemistry code simulates the physical and chemical process inside the molecular cloud and the constraints of observation and astrochemical models that can help us understand better about physics and chemistry inside the high-mass molecular cloud.

My thesis focuses on the star-forming region Sgr B2 (M), which contains high abundances of sulfur-bearing species such as SO_2, SO, OCS, H_2S, H_2CS, and CS. Our primary goal is to derive the region's chemical and physical properties and investigate the effects of cosmic rays, density distribution, and kinetic temperature on the chemical evolution of S-bearing species in high-density molecular clouds.

The thesis is structured as follows:

- In Part II, I present the analysis methods used to extract the properties of the investigated sources and the astrochemical code used to simulate the molecular cloud.
- In Part III, I present the observational results. We derive the chemical abundance of molecules by using XCLASS to analyze the molecules' line emission and construct the column density and temperature maps.
- Part IV shows the astrochemical modeling of the sources. The astrochemical code, saptarsy, is used to simulate the physicochemical evolution of the molecular cloud. The simulations explore the influence of physical properties (cosmic-ray ionization rate, density distribution, thermal evolution, and desorption binding energy of molecules) on the chemical evolution in the molecular cloud.
- In Part V, I compared the observational results and the astrochemical models by

constraining the cosmic-ray ionization rate, the density distribution, the thermal evolution that best reproduces the observations.

- Finally, I present the conclusion and the outlook in part VI, which provides some possibilities for improving our prospect of high-mass star formation.

Part II

Methods

Chapter 4

Deriving molecular column densities

We use spectroscopy to study the interaction between electromagnetic radiation and matter to derive astronomical objects' chemical composition and physical conditions such as stars, molecular clouds, and high-mass and low-mass star-forming regions. Spectroscopy is used to identify the physical properties of molecules from their unique spectral fingerprints, such as determining the abundance, structure, and temperature of molecules by analyzing spectral lines of atoms and molecules. The frequency of the spectral lines can be observed across the electromagnetic spectrum, from radio waves to gamma rays:

- The radiofrequency to microwave region correspond mostly to rotational transitions in molecules and fine structure transition of atoms.
- Infrared quanta correspond to the vibrational motion in molecules.
- Electronic transitions occur in the visible/UV range.

To analyze species' physical and chemical properties in a molecular cloud, we can use molecules' rotational and vibrational state, which can be detected in the mm-submm range with radio telescopes.

Rotational levels of a molecule can be described by a vibrational quantum number v and the rotational quantum number J. In the case of a diatomic or linear molecule, such as CO, OCS, C_2H_2, a rotational transition between the upper and lower states J_u (upper) and J_l (lower) and in the vibrational state v will be related to as $Xv(J_u, J_l)$ (Bonfand, 2019) (Yamamoto, 2017).

For symmetric top molecules, if there are two out of the three moments of inertia of a nonlinear molecule that is identical by symmetry

- If $I_{bb} = I_{cc}$, the molecule is called a prolate symmetric top (for example CH_3CN),
- If $I_{aa} = I_{bb}$, the molecule is called an oblate symmetric top(for example NH_3)

and within the vibrational state v, the molecules will be referred to as $X_v(J_u(K) - J_l(K)$, and K represents the quantum number projected onto the symmetry axes of the molecule (Yamamoto, 2017).

In the case of asymmetric molecules and within the vibrational state v, the molecules will be referred to as $X_v(J_u(K_a, K_c) - J_l(K_a, K_c)$. K_a is the absolute value of the projection quantum number when the molecule is considered a prolate symmetric top, and K_c is the absolute value of the projection quantum number when the molecule is considered an oblate symmetric top.(Yamamoto, 2017)

4.1 Deriving molecular column densities by using rotational diagrams

Energies are distributed in two level (upper and lower), E_u and E_l ($E_u > E_l \; and \; E_u - E_l = h\nu$) and statistical weights g_u and g_l.

Number of molecules in the upper state related t line opacity:

$$N_u = \frac{8\pi\nu^3}{c^3 A_{ul}} \left[e^{\left(\frac{h\nu}{k_b T_{ex}}\right)} - 1 \right]^{-1} \int \tau_\nu dv \tag{4.1}$$

A_{ul} is Einstein coefficient of spontaneous emission

When the gas density > critical density $(n_{cr})(n_{cr} = A_{ul}/C_{ul}, \; where \; C_{ul}$ is the collisional rate coefficient), colisions excitation dominate radiative processes. Two-level system (upper and lower state) is in local thermodynamic equilibrium (LTE), level populations follow a Boltzman distribution:

$$\frac{n_u}{n_l} = \frac{g_u}{g_l} e^{\left(-\frac{h\nu}{k_b T_{ex}}\right)} \tag{4.2}$$

Gas density $\geq n_{cr} \rightarrow T_{ex} \approx T_K$(kinetic temperature of the gas)
Gas density $< n_{cr} \rightarrow T_{ex} < T_K$, energy levels are sub-thermally populated

At thermal equilibrium: $N_u \sim N_{tot}$ total colum density of molecule

$$\frac{N_{tot}}{N_u} = \frac{Q_{rot}(T_{ex})}{g_u} e^{\frac{E_u}{k_b T_{ex}}}, \tag{4.3}$$

Q_{rot} is the rotational partition function:

$$Q_{rot} = \sum_i g_i e^{-\frac{E_i}{k_b T_{ex}}} \tag{4.4}$$

We can derive the kinetic temperature, and the total column density of molecules by using population diagram analysis (Goldsmith & Langer, 1999) for multiple observed line transitions. Under LTE and optically thin conditions, we can take the natural logarithm of both sides of the equation 4.3 and get the equation 4.5. From the plot of the natural logarithm of N_u/g_u versus E_u/k_b in equation 4.5, we can generate a straight line which slope is proportional to the inversed temperature $(1/T_{rot})$, and the intercept is $\ln\left(\frac{N_{tot}}{Q_{rot}}\right)$. From the intercept, we can derive the total column density of the given molecule.

$$\ln\left(\frac{N_u}{g_u}\right) = -\frac{E_u}{k_b T_{rot}} + \ln\left(\frac{N_{tot}}{Q_{rot}}\right) \tag{4.5}$$

Because of the high column density and complex structure's Sgr B2 (M), we could not use the rotational diagram to derive the column density of S-bearing molecules. Moreover, the temperature based on rotation diagram analysis can be wrong due to a neglect of the line opacity and the line blending problems in the high-mass stars forming regions. Therefore, we used the eXtended CASA Line Analysis Software Suite (XCLASS) (Möller, Endres, & Schilke, 2017). This software uses the myXCLASS program, a one-dimensional radiative transfer program using CDMS/JPL molecular data, and XCLASS can get the corrected temperature using the opacity correction.

4.2 Using XCLASS to determine the column density and temperature of molecules

XCLASS can model and fit the line of molecules based on the radiative transfer equation and easily calculate column density and temperature velocity under LTE and molecules in optically thin conditions. (Möller et al., 2017).

$$\begin{aligned} T_{\mathrm{mb}}(\nu) = \sum_{m,c \in i} \left[\eta(\theta^{m,c}_{\mathrm{source}}) \left[S^{m,c}(\nu) \left(1 - e^{-\tau^{m,c}_{\mathrm{total}}(\nu)} \right) \quad + I_{\mathrm{bg}}(\nu) \left(e^{-\tau^{m,c}_{\mathrm{total}}(\nu)} - 1 \right) \right] \right] \\ + \left(I_{\mathrm{bg}}(\nu) - J_{\mathrm{CMB}} \right) \end{aligned}$$

where the sums go over the indices m for molecule, and c for component, respectively. Here, $\eta\left(\theta^{m,c}\right)$ indicates the beam filling (dilution) factor, $S^{m,c}(\nu)$ the source function $\tau^{m,c}_{\mathrm{total}}(\nu)$ the total optical depth of each molecule m and component c. I_{bg} represents the background intensity J_{CMB} the intensity of the cosmic microwave background.

Under the LTE assumption, the kinetic temperature of the gas can be estimated from the rotation temperature: $T_{\mathrm{rot}} \approx T_{\mathrm{kin}}$.

As these high-mass star-forming regions have high H_2 densities $n_{H_2} > 10^5$ cm^{-3}, LTE conditions can be assumed (Mangum & Shirley, 2015).

Line profiles are assumed to be Gaussian, but finite source size, dust attenuation, and optical depth effects are also considered. Molecular parameters (such as transition frequencies, Einstein A coefficients, partition functions) are taken from an embedded SQLite database containing entries from the Cologne Database for Molecular Spectroscopy (Müller, Thorwirth, Roth, & Winnewisser, 2001) (Müller, Schlöder, Stutzki, & Winnewisser, 2005), and Jet Propulsion Laboratory database (Pickett et al., 1998) using the Virtual Atomic and Molecular Data Center (Endres, Schlemmer, Schilke, Stutzki, & Müller, 2016). The line profiles are assumed as Gaussian function, and other cloud parameters such as source size, dust attenuation, and optical depth are also considered.

Moreover, we assume that the Sgr B2 (Main) is local thermodynamic equilibrium (LTE). Under the LTE presumption, the gas' kinetic temperature assumed to be equal to the rotation temperature: ($T_{rot} \sim T_{kin}$).

Because Sgr B2 (M) is the high mass star formation region, high density, and high temperature, the molecules have high abundances. Many complex molecules and their isotopes make the area have a line-rich source. Due to the formation of massive stars, this process affects the structure of the cloud, causing the cloud to have a complex system such as having many velocity components. For calculating the column density of molecules in Sgr B2 (M), we must determine the velocity structure of the cloud. By using the line stacking method developed by our group (Schwörer et al., 2019), we can determine the velocity component of each pixel, based on which we can use the data cube to fit the molecular lines and find out the column density and temperature of the S-bearing molecules.

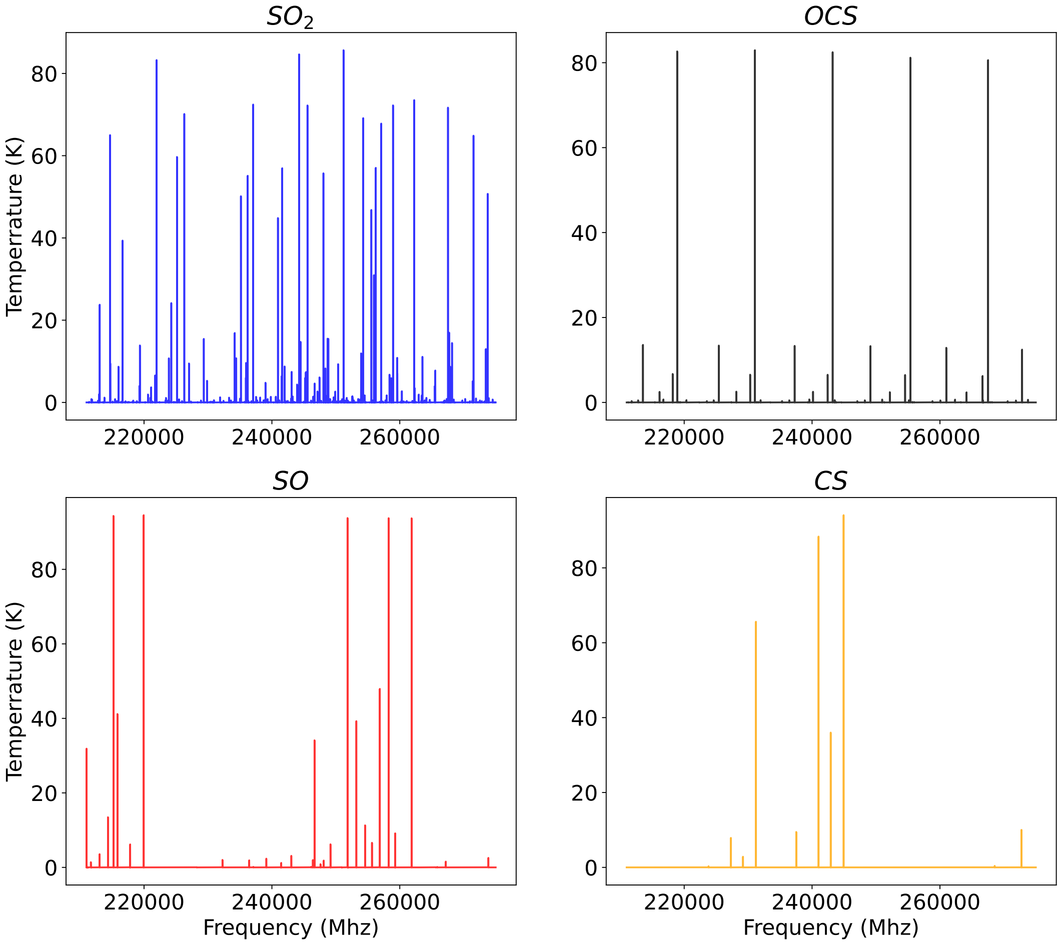

Figure 4.1: The spectra of S-bearing molecules (in the frequency range ALMA band 6) created by using XCLASS. The parameters were used: Temperature T =100 (K) column density $N_{molecules} = 10^{17}(\ \mathrm{cm}^{-2})$, and velocity shift = 0 (km/s).

Firstly, we used XCLASS to model spectra of molecules in the observational frequency range (211 - 275 GHz); the spectra of molecules are shown in Fig 4.1. We then select lines with high intensity to use as input parameters for the next step (we choose threshold > 10 K). Using the line stacking method, we predicted the number of components and each molecule's velocity width and velocity shift at each pixel. However, since Sgr B2 (M) is a high mass star-forming region, many other molecules exist concurrently with the one to be calculated, so the phenomena line blended and might be biased by a different line of other molecules, and line stacking is partly taking care of it. Moreover, for the molecule SO_2 there are many lines in the observation region, so it is easier to use the line stacking method than other molecules. For OCS and SO, the number of lines with high intensity is small (< 12 transition lines), determining the number of components is difficult.

After calculating the number of velocity components in each pixel, we use XCLASS to calculate the column density and temperature of molecules. In our data (Sgr B2

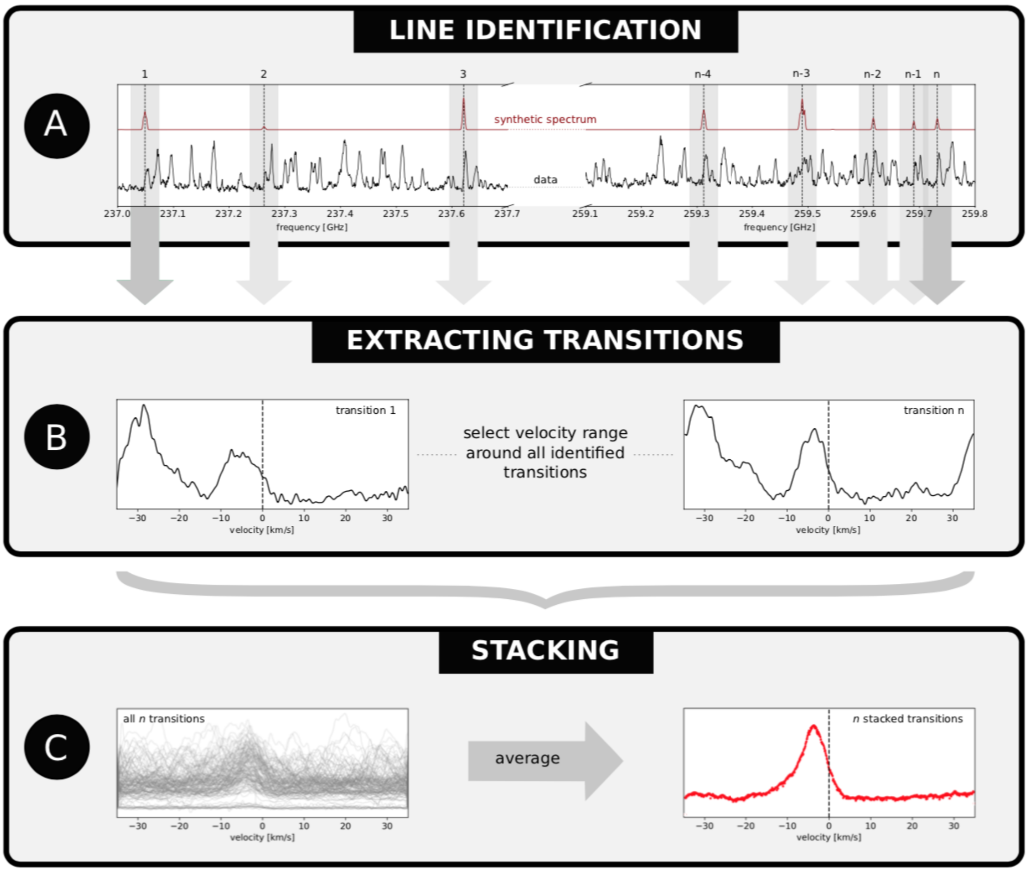

Figure 4.2: The illustration of the line stacking method, from the observed data in each pixel to the stacked transition(Schwörer et al., 2019)

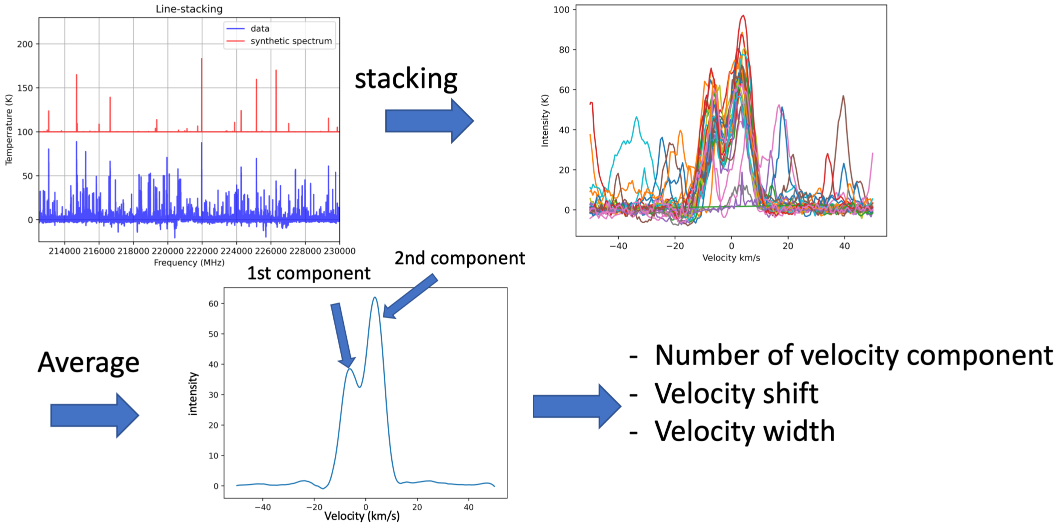

Figure 4.3: The illustration of line stacking shows how to define the velocity component of SO_2 molecules in a single pixel. We can determine the number of velocity components (two components) and the velocity of the first and second components.

(M) ALMA Band 6), we found that SO_2 is the highest number of line transitions and intensity ($\sim$ 76 lines which intensity larger than 10) in SgrB2 (M), and we found SO_2 molecules almost everywhere in Sgr B2 (M). In addition, SO_2 molecules is an asymmetric top molecule which is more promising for spectroscopic investigations to derive the kinetic temperature of the molecular cloud since SO_2 molecules have more transitions spanning a more extensive range of excitation energies than linear molecules such as OCS, CS, SO molecules. Because the number of transition lines of H_2S and H_2CS molecules is relatively small, we cannot use those molecules to determine the kinetic temperature of the cloud.

For those reasons, we fitted SO_2 lines first by XCLASS to derive the temperature and column density of SO_2 in the cloud, and then we derive the column density of remaining molecules, using the temperature derived from SO_2.

The algorithm we use is Levenberg Marquardt (LM) (Marquardt, 1963) is a hybrid between the Gauss-Newton algorithm and the method of gradient descent. The LM can find a local minimum and strongly depends on the starting values of the parameters to be optimized. With this algorithm, XCLASS can fit line emission of molecules quickly.

Chapter 5

Saptarsy - the astrochemical model

5.1 Saptarsy

The astrochemistry code Saptarsy was developed by (Choudhury et al., 2015), which was used to simulate the Spatio-temporal evolution of complex organic molecules' abundances in hot molecular cores. Then (Stéphan et al., 2018) extended Saptarsy's functionalities to study chemistry in HII regions. The astrochemistry code uses the solver DVODPK and MA28, the solver of the sparse system of linear equations from (HSL), to solve the ordinary differential equations.

Saptarsy can simulate Spatio-temporal evolution molecules using the thermal and radiation field evolution obtained from RADMC-3D (Dullemond et al., 2012)[1] . The inputs of Saptarsy include the chemical network (gas-phase and grain surface chemical network from KIDA and OSU (Garrod et al., 2008)) and the initial abundances.

5.1.1 Reaction rate approach

The chemical reaction of two molecules can be written like equaA + B $\longrightarrow$ C + D. The reaction rate depends on A and B concentration or density (noted as [A] and [B]) and on a rate constant or rate coefficient k. Thus, the reaction rate for the chemical reaction can be given as follows:

$$\frac{d[A]}{dt} = \frac{d[B]}{dt} = -\frac{d[C]}{dt} = -\frac{d[D]}{dt} = -k[A][B] \tag{5.1}$$

The use of Saptarsy is computing the reaction rates for every species in every specific timestep. Saptarsy is based on the rate equation approach, which is derived from the Arrhenius law. This law describes the temperature dependence on the rate constant k :

$$k\left(T_{\mathrm{g}}\right) = A \exp\left(-\frac{E_{\mathrm{A}}}{RT_{\mathrm{g}}}\right) \tag{5.2}$$

Where T_{g} is the gas temperature, A is the frequency - or collision factor (i.e., number of molecules per second), E_{A} is the activation energy of the reaction (in Kelvin) and R is the ideal gas constant.

---

[1] The code package RADMC-3D is a tool for characteristic radiative transfer in astrophysics https://www.ita.uni-heidelberg.de/~dullemond/software/radmc-3d/

The astrochemical codes numerically solve the equations of chemical kinetics describing the formation and destruction of molecules:

$$\frac{\mathrm{d}n_i}{\mathrm{d}t} = \sum_{l,m} k_{lm} n_l n_m - n_i \sum_{i \neq l} k_l n_l + k_i^{\mathrm{des}} n_i^s - k_i^{\mathrm{acc}} n_i \tag{5.3}$$

$$\frac{\mathrm{d}n_i^s}{\mathrm{d}t} = \sum_{l,m} k_{lm}^s n_l^s n_m^s - n_i^s \sum_{i \neq l} k_l^s n_l^s - k_i^{\mathrm{des}} n_i^s + k_i^{\mathrm{acc}} n_i \tag{5.4}$$

where

- n_i and n_i^s are the gas-phase and surface concentrations of the i th species (cm^{-3}),
- k_{lm} and k_l are the gas-phase reaction rates
- k_i^{acc} and k_i^{des} express the accretion and desorption rates (s^{-1}),
- k_{lm}^s and k_l^s are surface reaction rates (cm^3 s^{-1})

5.1.2 Gas-phase reactions in the simulation

Gas-phase two-body processes

In two chemical reactants reacted in gas-phase processes such as ion-molecular and neutral-neutral reaction (reaction type 2 → type 12 in table 5.2). The reaction rates can be computed by using the Arrhenius equation 5.2 which can also be written as in the following form (Semenov et al., 2010):

$$k\left(T_{\mathrm{g}}\right) = \alpha \left(\frac{T_{\mathrm{g}}}{300K}\right)^{\beta} \exp\left(-\frac{\gamma}{T_{\mathrm{g}}}\right) \tag{5.5}$$

Where α, β, and γ are experimentally determined parameters

- α is the reaction rate value at a room temperature of 300 K,
- β defines the temperature dependence of the rate and is normalized to the room temperature,
- γ is the activation energy.

Cosmic ray (CR) ionization and dissociation

To compute the ionization and dissociation rates of molecules by the cosmic ray (reaction type 1 in table 5.2), we use the following equation to calculate the reaction rate coefficient:

$$k_{\mathrm{CR}} = \alpha \zeta_{\mathrm{CR}} \tag{5.6}$$

Photo-dissociation

To compute photo-dissociation rates in a molecular cloud (reaction type 13 in table 5.2), we utilize (Dishoeck, 1988) precomputed fits for a 1D plane-parallel slab, using the Draine FUV IS radiation field. The reaction rate coefficient can be computed as

$$k_{\mathrm{FUV}} = \alpha \exp(-\gamma \cdot A_v) G_0 \tag{5.7}$$

- A_V is the visual extinction (mag)
- G_0 the unattenuated FUV flux expressed in units of the FUV interstellar radiation field G_0 of (Draine, 1978).

Photodestruction due to cosmic rays

The flowing equation can compute the rate coefficient of the cosmic-ray induced ultraviolet flux.

$$k = \alpha \cdot n_H \cdot \zeta \cdot \left(\frac{T_g}{300K}\right)^{\beta} \tag{5.8}$$

Here, and below, $n_H = 2n(\mathrm{H_2})/[n(H) + 2n(\mathrm{H_2})]$ is the relative abundance of hydrogen to total hydrogen nuclei, and ζ is the cosmic rays ionization rate.

5.1.3 Grain-phase reactions in the simulation

The gas-grain reactions are shown in Table 5.2, with the abbreviation JX is the X molecule on grain surfaces.

Accretion on grain surfaces (reaction type 99)

Our model considers the accretion of particles into the dust surface by physisorption, and we neglect chemisorption. The calculation of the rate constant 5.9 is used from (Hasegawa, Herbst, & Leung, 1992)

$$k = \alpha P_{\text{stick}}\, v_{\text{th}}(i) n_{\text{d}} \tag{5.9}$$

, where $\sigma_{\mathrm{d}} = \pi \left(r_{\mathrm{d}} + l d_{\text{site}}\right)^2$ is the geometric cross section of the dust grain.

The thermal velocity v_{th}(i) is the average velocity of a collection of the particles. The following equation gives this average velocity:

$$v_{\text{th}} = \sqrt{\frac{8k_{\mathrm{B}}T_{\mathrm{g}}}{\pi\mu(i)m_{\mathrm{p}}}} \tag{5.10}$$

, where

- k_{B} is the Boltzmann constant,
- T_{g} the gas temperature,
- μ the reduced mass of species i,
- m_{p} the proton mass.

Thermal Desorption (reaction type 15)

When the dust temperature rises, the molecules evaporate into the gas phase. This desorption type is the primary source of evaporated material for dust temperatures above 100 K. The rate of the thermal desorption process is mainly affected by the desorption energy E_{D}, usually given in Kelvin.

$$k = \alpha v_0(i) \exp\left(\frac{-E_{\mathrm{D}}(i)}{T_{\mathrm{d}}}\right) \tag{5.11}$$

The characteristic frequency $v_0(i)$ of the vibrational mode causes the desorption, and it can be derived by using a harmonic oscillator approximation.

$$v_0(i) = \sqrt{\frac{2\Sigma_{\mathrm{sites}}\, k_{\mathrm{B}} E_{\mathrm{D}}(i)}{\pi^2 m(i) m_{\mathrm{p}}}} \tag{5.12}$$

where

- Σ_{sites} is the surface density of sites ,
- E_{D} is the desorption energy,
- $m(i)$ is the mass of the desorbing species ,
- k_{B} is the Botzmann constant
- m_{p} is the proton mass.

Cosmic ray desorption (reaction type 16)

Cosmic rays affect the surface of the entire dust grain. Cosmic ray desorption is treated with a straightforward procedure, first introduced by (Hasegawa & Herbst, 1993). They assumed that a cosmic ray particle with average energy 0.4MeV interacts with a dust grain which size 0.1μm, and heating the dust to 70 K. The rate of cosmic ray induced desorption can compute via this equation:

$$k = f k_{\mathrm{des}}(70\ \mathrm{K}) \tag{5.13}$$

where

- k_{des} is the thermal desorption rate at 70 K
- f is the fraction of time the dust temperature, which stays close to 70 K. The used value of f is 3×10^{-19}.

Photodesorption

Molecules can be desorbed into the gas phase by UV photons originating from the protostars or produced as secondary photons by cosmic rays. The rate of this process can be calculated through the following equation (Le Petit, Nehmé, Le Bourlot, & Roueff, 2006):

$$\mathrm{k} = \alpha \left(F_{\mathrm{star}} + F_{2^{\mathrm{md}}\mathrm{photon}} \cdot \frac{2\mathrm{n}\left(\mathrm{H}_2\right)}{\mathrm{n}(\mathrm{H}) + 2\mathrm{n}\left(\mathrm{H}_2\right)}\right) \sigma_{\mathrm{g}}$$

where

- $F_{\rm star} = G_0 \cdot 2.69916 \times 10^8$ JyDraine $^{-1}$ is the flux of the protostar, G_0 is the radiation field , and $F_{2^{\rm nd}\ \rm photon} = \zeta_{\rm CR} 10^{20}$ Jys is the flux of secondary photons,
- $\sigma_{\rm g}$ is the geometric cross section of the dust
  $\sigma_{\rm g} = \frac{\pi {\rm r}_{\rm d}^2}{}$ $\rm N_s$ $\rm r_d$ is the radius of the dust grain, and $\rm N_S$ is the number of sites in the surface layer.

And other grain-surface processes:

- Neutral, neutral reaction on the grain surface. (reaction type 14)
- Formation of H_2 – for small networks when no H_2 on grains (Le Bourlot, Le Petit, Pinto, Roueff, & Roy, 2012) (reaction type 22)

5.1.4 The multilayer approach for simulating dust grain chemistry.

Dust grains absorb atoms and molecules on their surface, provide the surface for molecules to interact with each other, and increase chemical reactions chance, which plays an essential role in producing complex molecules and increasing the chemical complexity of molecular clouds.

The most simplistic model for dust is the so-called two-phase model. It only consists of a gas phase and a grain phase. This model has drawbacks when more molecules absorb on the grain surface, leading to more molecules than the number of grain sites. When molecules on the grain desorb, all inner and outer molecules on the grain can quickly evaporate to the gas phase.

Those drawbacks led us to the three-phase model that classified the mantle and surface phases. The molecules in the mantle phase are buried inside the grain and recognized as chemically inert. Still, the surface phase is an outer layer, and molecules in this phase are chemical activity.

(Taquet, Ceccarelli, & Kahane, 2012) improve the three-phase model into a multiphase or multilayer model. Thus, the mantle phase is divided into multiple monolayers, and each layer in the mantle is considered. Nevertheless, this model cannot simulate the desorption process throughout the warm-up phase of the molecular cloud's evolution.

(Vasyunin & Herbst, 2013) used the macroscopic Monte Carlo approach to model the cold and the warm-up phase of the molecular cloud. However, with this approach, the calculation requires more time than the reaction rate approach (several hours or even days versus a few minutes in the reaction rate approach).

(Schaefer, 2017) improved the three-phase model into the multi-phase model, which was the rate equation approach, including absorption and desorption. We can simulate astrochemistry more accurately and faster with this improvement than previous models.

5.1.5 Chemical Model

Using RADMC-3D and the (Hosokawa & Omukai, 2009) models, we can calculate the temperature as a function of radius for each time step.

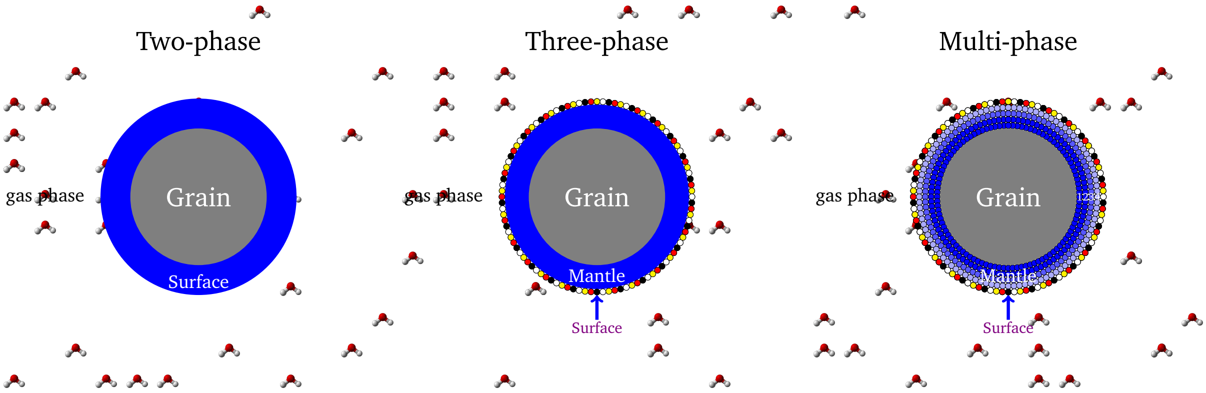

Figure 5.1: The three primary model approaches for simulating dust grain chemistry in the molecular cloud: the two-phase model, the three-phase model, and the multi-phase. (adapted from Master thesis Dirk Schaefer (Schaefer, 2017)).

This thesis uses the reaction rate approach to compute the chemical evolution. Using this approach, we can calculate the chemical abundances rapidly, and the results are within the acceptable range.

Providing chemical network (including $\alpha, \beta,$ and γ in equation 5.5) and initial abundances (Table 5.1), we can use saptarsy to compute the evolution of the abundances of molecules. Saptarsy also can calculate the reaction rate and reaction rate coefficient. Using the reaction rate and chemical network, we can understand which reaction is more important than others.

Table 5.1: Elemental Abundances with Respect to n_H (Wakelam & Herbst, 2008)

Species	n_i/n_H
He	9.0×10^{-02}
H_2	5.0×10^{-01}
C^+	1.2×10^{-04}
N	7.6×10^{-05}
O	2.6×10^{-04}
S^+	5.0×10^{-05}
Si^+	8.0×10^{-09}
Fe^+	3.0×10^{-09}
GRAIN0	1.0

In the chemical model, We use reduced Ohio State University (OSU) networks (334 molecules) (Garrod et al., 2008) which has a large number of reactions (>3600 chemical reactions)

Table 5.2: Chemical reaction type (Schaefer, 2017)

Reaction Type	No
Cosmic Ray ionization. A(J)=scaling factor	01
Ion-molecule reactions and charge exchange reactions	02
Negative ion - neutral species reactions	03
Radiative association: ion-neutral	04
Electron ejection: negative ion - neutral	05
Neutral + neutral $\longrightarrow$ ion + e^- (only one reaction)	06
Neutral + Neutral chemical reaction	07
Neutral + Neutral radiative association	08
Dissociative recombination	09
Radiative recombination (No dissociation) atomic, molecular ion + e^-	10
Positive-ion .vs. Negative-ion Recombination	11
Electron attachment (neutral + $e^-$$\rightarrow$negative ion)	12
Photo-ionization and photo-dissociation	13
Grain-surface chemical reactions	14
Thermal evaporation JX$\rightarrow$X	15
Cosmic Ray induced general desorption JX $\longrightarrow$ X	16
Photodissociation by CR: JNO $\longrightarrow$ JN + JO corresponds to NO$\rightarrow$N + O	17
Photodissociation by CR: JNO $\longrightarrow$ JN + JO corresponds to NO$\rightarrow$$NO^+$ + e^-	18
Photodissociation by background photons: JC_2 $\longrightarrow$ JC + JC corresponds to $C_2$$\rightarrow$C + C	19
Photodissociation by background photons: $JC_2$$\rightarrow$JC + JC corresponds to $C_2$$\rightarrow$$C_2^+$ + e^-	20
Photo-desorption (discriminate or indiscriminate)	21
Formation of H2 when not present as a grain species (Le Bourlot et al., 2012)	22
Second photon processes	23
Surface accretion X$\rightarrow$JX	99

In our simulation, the chemical network of S-bearing molecules is relatively large. We have to divide them into two part:

- the S-bearing molecules which also bearing Oxygen atom (such as SO_2, SO molecules), which is shown in Fig 5.2
- the S-bearing molecules without bearing Oxygen atom (such as CS, H_2S, H_2CS), which is shown in Fig 5.3

5.2 The Physical Model

We will illustrate our models' physical properties: conditions, particularly temperature, density, and visual extinction, which evolved during high mass stars formation processing molecular cloud. We categorized the star's formation process into two phases: the cold collapse and warm-up phases.

- Initially, the density and temperature of the molecular cloud are relatively low, and then the cloud will collapse, which generates high density and cold-core.

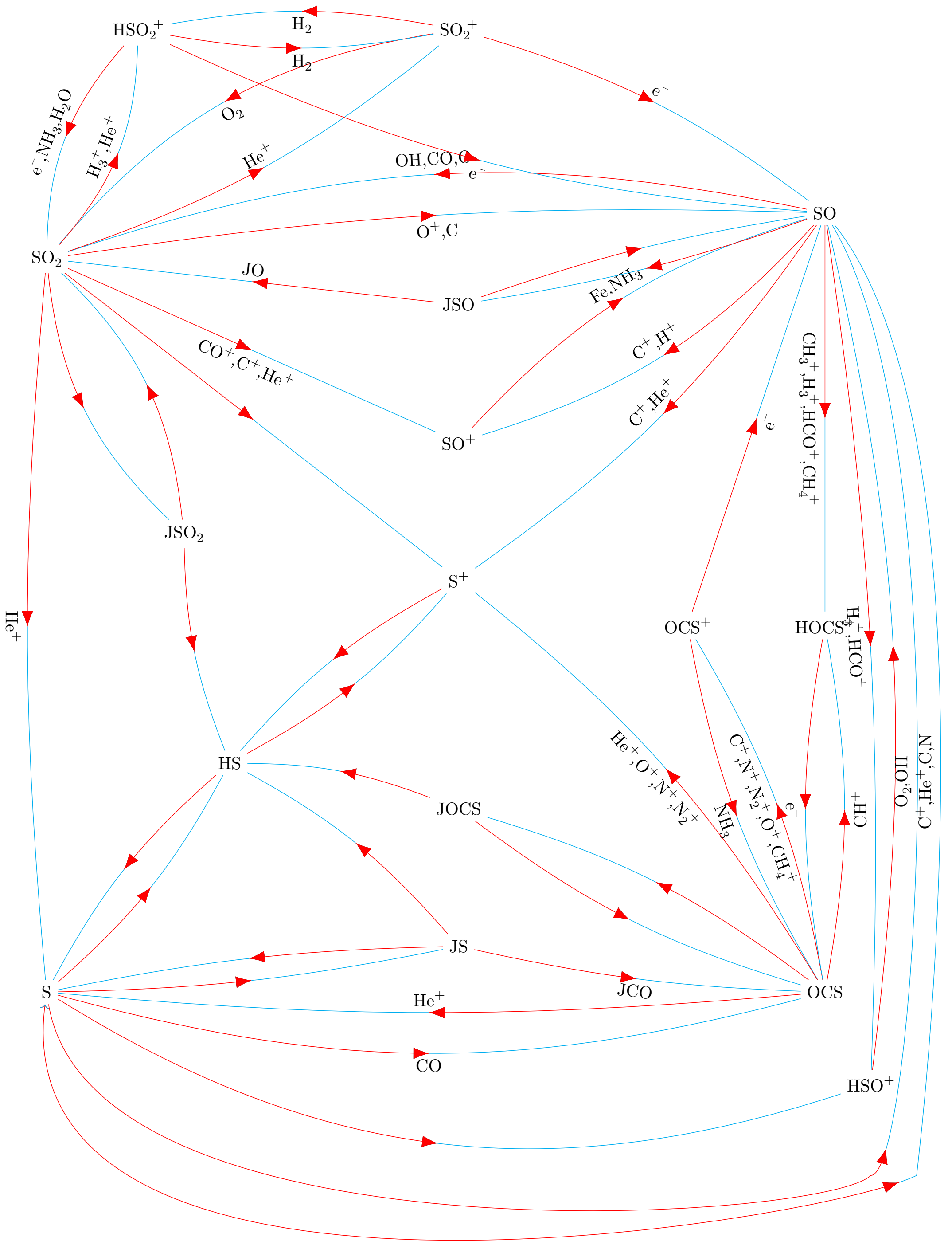

Figure 5.2: The chemical network of sulfur-bearing molecules, which we used to compute in saptarsy. The network covers all S-bearing molecules which are also bearing Oxygen

- Secondly, the core will be heated until the protostellar forms and evolves at the center of the core.

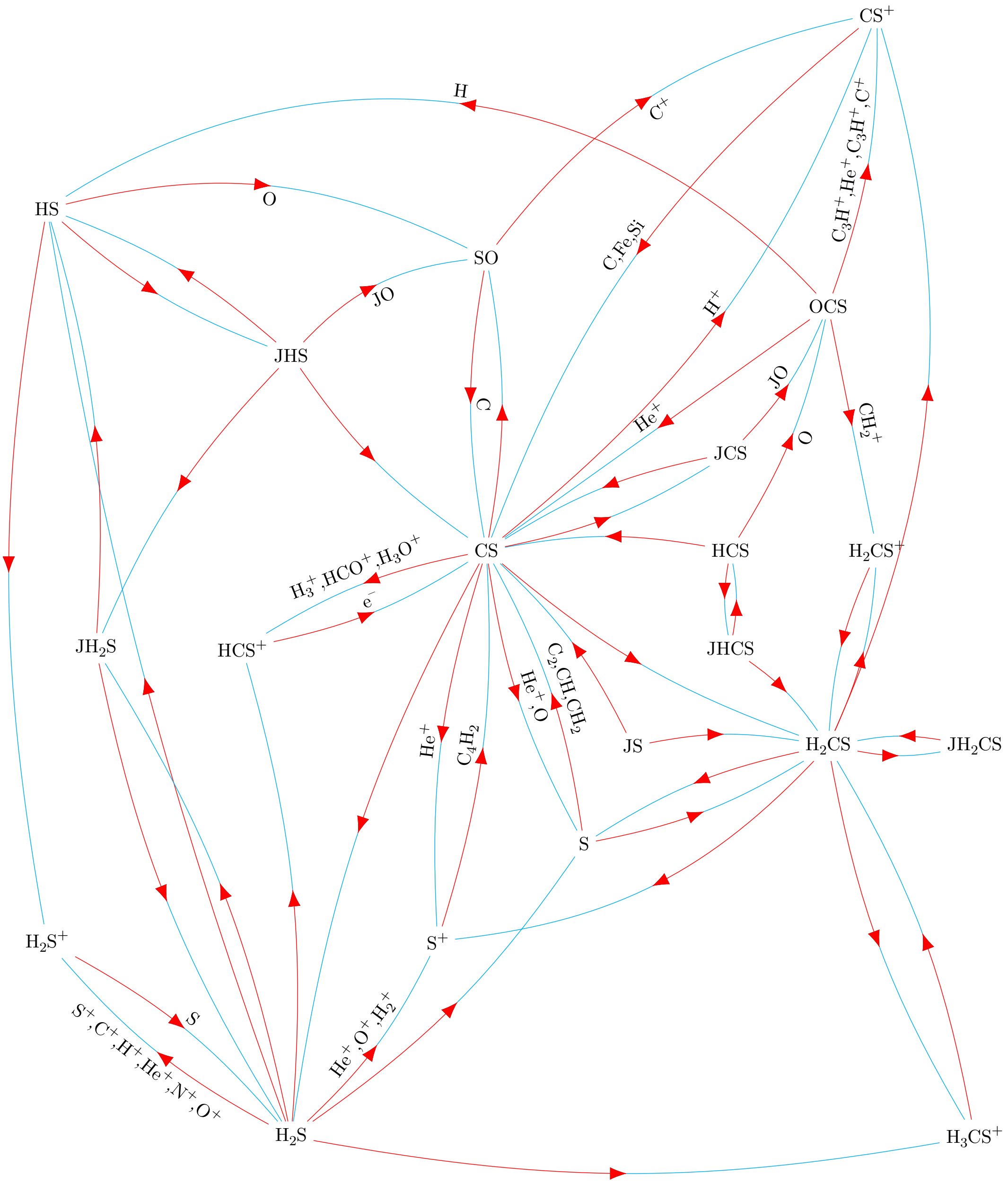

Figure 5.3: The chemical network of sulfur-bearing molecules, which we used to compute in saptarsy. The network covers all S-bearing molecules without Oxygen

5.2.1 Density and thermal evolution of molecular cloud

The Cold Collapse Phase

The hydrodynamical code is the most accurate for dealing with the molecular cloud's physical evolution. Using the hydrodynamical code to analyze the ISM can be done today. Still, it has a high calculation cost and is not proper for a large parameter grid in different models. Consequently, this thesis uses the Spitzer model (Spitzer Jr & Arny, 1978) to implement the cold-collapse phase.

Spitzer's model can derive an equation for the density evolution of a gravitationally collapsing cloud with a constant temperature. Rotating and magnetic effects in the cold-

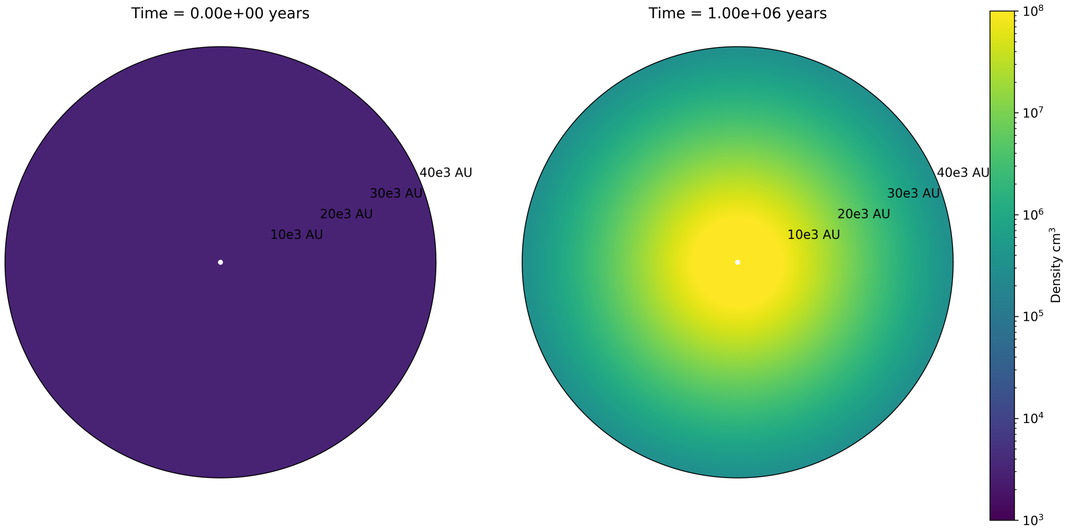

Figure 5.4: Density evolution of the molecular cloud in cold collapse phase in 1 million years.

collapse phase are ignored.

Based on Spitzer's ideas and after some transformations, the resulting equation reads as follows:

$$\frac{dn_{\mathrm{H}}}{dt} = R\left(\frac{n_{\mathrm{H}}^4}{n_{\mathrm{H},0}}\right)^{1/3}\left(24\pi G m_{\mathrm{H}} n_{\mathrm{H},0}\left[\left(\frac{n_{\mathrm{H}}}{n_{\mathrm{H},0}}\right)^{1/3} - 1\right]\right)^{1/2} \tag{5.14}$$

, where

- $\mathrm{n}_{\mathrm{H},0}$ is the initial density,
- n_{H} the final density at the end of the collapse phase,
- m_{H} the mass of a hydrogen atom,
- G the gravitational constant,
- The dimensionless factor $R \in [0, 1]$, called the retardation factor

By employing a numerical integration of the time derivative of the density, we obtain the density evolution of the cloud. We have the free choice of our initial and final density of the collapse. Our simulation uses 22 zones, represented as 22 parts of the molecular cloud in different radii.

Firstly, we input the initial values for the initial molecular cloud, such as radius, temperature, and visual extinction, which are homogeneous for the entire zone. The zones are also not spinning and moving, and we likewise ignore the magnetism of the cloud.

We are using the initial density of $n_{H_0} = 3.10^3$ cm^{-3} in each zone, and the final density depends on the final density of each zone (computed by using the Plummer-like function

Table 5.3: Different zone with varied density amplitude, retardation factors (R), and the distance of each zone.

Zone ID	Density (cm^{-3})	Retardation factor R	Distance (AU)
Zone-001	1.80×10^8	0.93778568	5.00×10^2
Zone-002	1.78×10^8	0.93721697	1.00×10^3
Zone-003	1.73×10^8	0.93747688	2.00×10^3
Zone-004	1.54×10^8	0.93685789	4.00×10^3
Zone-005	1.28×10^8	0.93777910	6.00×10^3
Zone-006	9.94×10^7	0.93765267	8.00×10^3
Zone-007	7.37×10^7	0.93775419	1.00×10^4
Zone-008	5.26×10^7	0.93400167	1.20×10^4
Zone-009	3.65×10^7	0.93576560	1.40×10^4
Zone-010	2.49×10^7	0.93638177	1.60×10^4
Zone-011	1.68×10^7	0.93129444	1.80×10^4
Zone-012	1.13×10^7	0.93498304	2.00×10^4
Zone-013	7.55×10^6	0.93278624	2.20×10^4
Zone-014	5.08×10^6	0.92155313	2.40×10^4
Zone-015	3.44×10^6	0.92467114	2.60×10^4
Zone-016	2.34×10^6	0.91786688	2.80×10^4
Zone-017	1.61×10^6	0.92948069	3.00×10^4
Zone-018	1.12×10^6	0.92729188	3.20×10^4
Zone-019	7.86×10^5	0.91353156	3.40×10^4
Zone-020	5.57×10^5	0.90255178	3.60×10^4
Zone-021	3.99×10^5	0.90845926	3.80×10^4
Zone-022	2.88×10^5	0.89569911	4.00×10^4

to determine the cloud's density structure) after a characteristic time scale equal 10^6 years. By changing the retardation factor R, we can manipulate each zone's final density in this phase. The table 5.3 shows the changing of the density of each zone depending on the retardation factor R.

To change the density evolution of the density in the cloud, we modified the retardation factor R . For instance, we use the R in inner zones higher than the outer zones, after 10^6 years in the cold collapse phase, the density in the internal zones are higher than the outer zone. By scaling the density (Fig. 5.4) and temperature (changing from 20 to 10 Kelvin) of each zone evolves in 10^6 years, we have the evolution of the entire cloud but not realistic because there is no mass transport in the simulation.

Moreover, we are using the equation which can compute the visual extinction A_v evolution by using the formula provided by (Garrod & Pauly, 2011),

$$A_{\mathrm{v}} = A_{\mathrm{v},0} \left(\frac{n_H}{n_{H,0}} \right)^{2/3} \tag{5.15}$$

The main goal of the cold collapse is to increase the density of the cloud from 3×10^3 cm^{-3} to the final density to use for the following step, the warm-up phase.

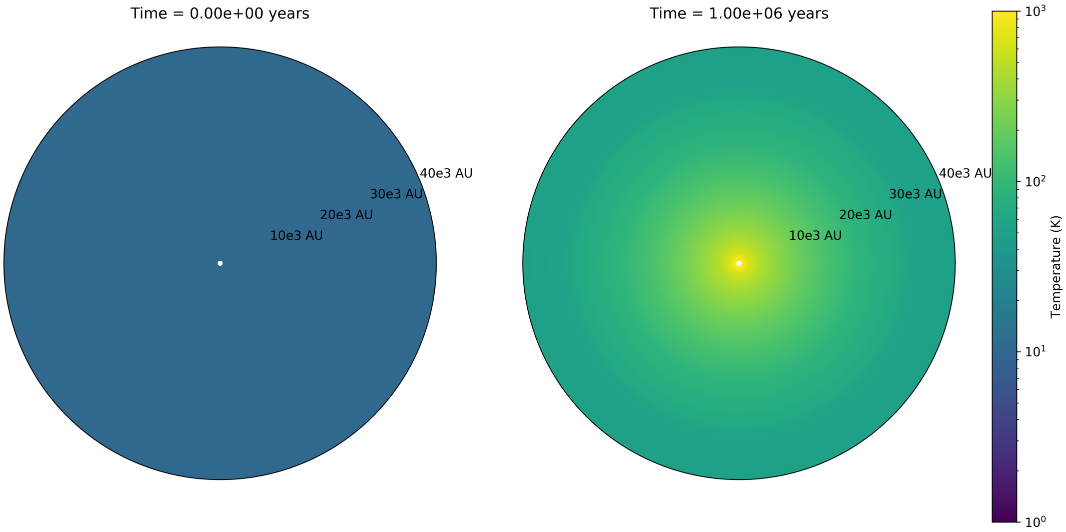

Figure 5.5: Thermal evolution of the molecular cloud in warm-up phase in 1 million years.

The Warm-up Phase

The main goal of the warm-up phase is to increase the temperature and keep the density of the cloud, to see the chemical evolution of the cloud-based on the thermal evolution. This simulation cannot move the molecular cloud's gas and dust, so the warm-up phase is a static model.

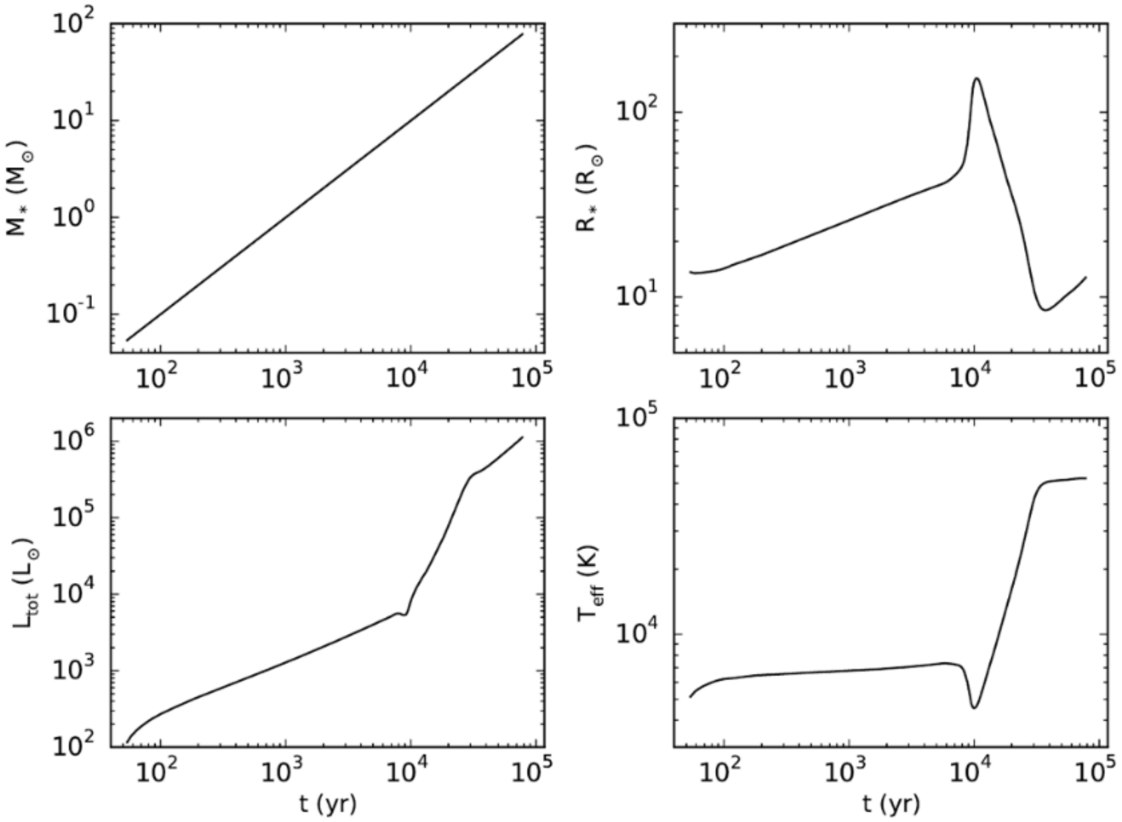

Figure 5.6: Time evolution of the parameters M_{star} (top left), R$_{star}$ (top right), L_{tot} (bottom left) and T_{eff} (bottom right) from (Hosokawa & Omukai, 2009) for an accretion rate $\dot{M} = 10^{-3} M_\odot/yr$.

In the warm-up phase, the initial cloud's temperature equals 10 Kelvin, and the central molecular cloud is the only source of warming up in our model setup. Therefore the temperature of the cloud's center depends on the luminosity of the protostar. We used the protostellar evolutionary models (shows in Fig. 5.6) of (Hosokawa & Omukai, 2009) to give us the protostellar luminosity as a function of time. Then, we use this luminosity and RADMC-3D to compute the temperature distribution in our spherical cloud, assuming a Plummer-like density profile. Fig. 5.5 shows the cloud's temperature evolution in 1 million years.

Part III

Observational results

Chapter 6

Sagittarius B2 Main

6.1 Physical structure

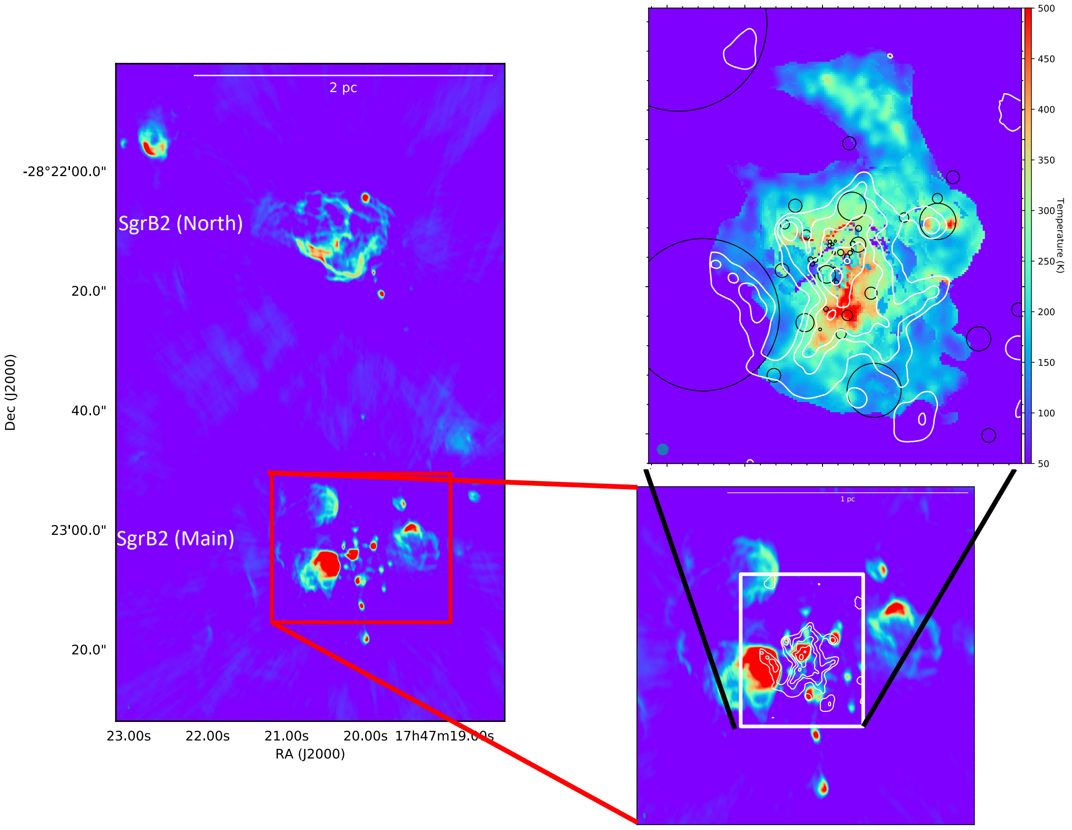

Figure 6.1: Sgr B2 was observed with Jansky Very Large Array (JVLA) in C-Band (4 to 8 GHz) (Meng et al., 2019), shown the spatial distribution of SgrB2 (North) and SgrB2 (Main) on the left-hand side, tracing mostly free-free emission in Sgr B2. The red rectangles: the zoom-in of the Sgr B2(Main) region including 1.3 mm dust continuum in white contour observed by ALMA 1.3 mm (Sánchez-Monge et al., 2017). The red rectangles: the temperature map of SO_2 (Fig. 6.7) in SgrB2(Main) including continuum contour in white color.

Sagittarius B2 is located at 8.34 kpc from the solar system and 100 pc from the

Galactic center (Reid et al., 2014). It is a giant complex molecular cloud with an average density $> 10^5$ cm^{-3}, a temperature of 50-70K, a total molecular mass of $10^7 M_\odot$, and a total luminosity of about $10^7 L_\odot$ (Goldsmith, Lis, Hills, & Lasenby, 1990). Owing to the proximity to the Galactic center (Sgr A*, 100pc) and to its location inside the CMZ (the area surrounding the Galactic center is about 200 pc), Sgr B2 is an intense star-forming area characterized by a density $N(H_2) \sim 10^4$ cm^{-3} and high column density $\sim 10^{23}$ cm^{-2}. It is thus affected by gas pressure from hot gas $10^{6\rightarrow7}$ K cm^{-3}.

There are two high-mass star-forming regions in Sgr B2: Sgr B2 (Main) and Sgr B2 (North). Those regions are high-density, high temperature, and high chemical complexity. Moreover, they contain at least ~ 50 high-mass stars with spectral types in the range from O5 to B0, making SgrB2 one of the best laboratories to search for complex organic molecules in the Milky Way.

Sgr B2(M) presents a higher degree of fragmentation, higher luminosity, and more ultracompact HII regions than Sgr B2 (N) (Qin et al., 2011b)(Sánchez-Monge et al., 2017). Besides, they have different chemical distributions: Sgr B2(M) is exceptionally rich in sulfur-bearing molecules, and Sgr B2(N) mainly contains complex organic molecules(Qin et al., 2011b)(Belloche et al., 2013).

The centimeter wavelength (C band (4–8 GHz)) data (JVLA) is used to trace the ionized component to identify dense cores, and their associated UCHII regions in the SgrB2 region (Meng et al., 2019). The image (6.1) is shown the HII regions in SgrB2(M) and SgrB2(N). The zoom-in of the region where SgB2 (Main) is embedded on the right-hand side of the figure shows the overlap of data (C band data) and the radio continuum emission of dust (white contour) by using ALMA 1.3 mm data which show the ionized component where the high-mass star is forming in SgrB2(Main).

This research focuses on Sgr B2 (M), on chemical and physical properties in the Sgr B2 (Main) region. Because this region contains high abundances of sulfur-bearing species such as SO_2, SO, OCS, CS, we focus on understanding the morphology and spatial structure of the molecules.

The continuum image and several dust cores (27 sources) in Sgr B2(M) have been detected in previous studies (Sánchez-Monge et al., 2017). From the ALMA data, we analyze the global chemical properties of the cloud. The image of continuum and integrated spectra of Sgr B2 (Main) in Fig 6.2 show us the dust and molecules distribution. We can see that the outer northern part of the cloud is mainly visible in molecular lines and not in the continuum. We should analyze this part's velocity structure, chemistry, and physical properties in more detail.

Firstly, we use line stacking, which can determine the distribution of the molecules. However, excitation information is lost since lines from various excitation levels are stacked. With XCLASS and CDMS database, we can get the line transitions of S-bearing species like H_2CS and OCS, SO_2, SO, H_2S in the given frequency range (ALMA Band 6 (frequency range from 211 to 275 GHz)). Using that information and line-stacking, we can determine the spatial distribution of S-bearing molecules' velocity structure. The Fig. 6.3 shows the spatial distribution of SO_2, SO, OCS, CS, H_2S, H_2CS molecules in Sgr B2(Main) which are derived by using line-stacking. From the Fig. 6.3, we can see, SO_2 and SO almost follow the integrated spectra, OCS mostly tracing the dust map, H_2S distributes mostly in the northern part of the integrated map, CS molecule mostly affected

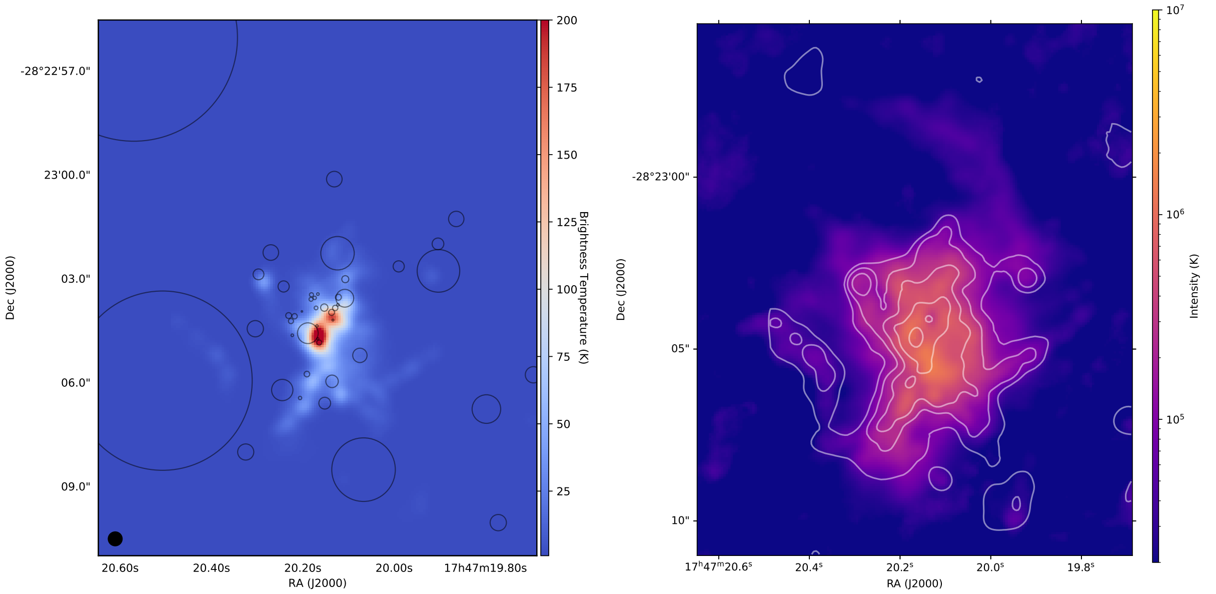

(a) (b)

Figure 6.2: **Left panel:** The ALMA 1.3 mm continuum emission with the black circles indicate the position of HII regions. **Right panel:** integral brightness temperature of all lines in the whole observational frequency range (ALMA band 6) of Sgr B2 (Main). The white contour shows the 1.3 mm continuum map of the cloud Sgr B2 (M) (the left panel).

by shock, is tracing the core and the northern outer part of the dust map, H_2CS only exists at the center of the cloud. We can see that SO_2 is more widely distributed than other molecules. Moreover, SO_2 has the largest number of transitions and the highest intensities in our data. We, therefore, use SO_2 to determine the temperature and velocity structure of the cloud.

From line stacking data cube, we can produce the cloud's 3 D map with x-axis and y-axis is the coordination of SgrB2 (Main) and the third axis (z-axis) is the velocity axis which is the velocity of SO_2 molecules (Fig 6.4). The northern outer part has a shield-like morphology, and this region expands the Sgr B2 (Main) due to the stellar wind created by the high-mass star formation. The formation of the high-mass stars at the position H2RA (we name the HII region inside the region A, which creates the stellar wind and impact the A region) in Fig. 6.1 and Fig. 6.5 creates the stellar wind and the extent of the HII regions.

The cloud has shown a complex structure, and we classify the cloud into two parts: the upper and lower parts.

- The upper part is affected by HII expansion (A region in Fig 6.5).
- The lower part is chemical-rich at nearby the core (B region in Fig 6.5).

We will detail the chemical properties of these two parts next section, the chemistry of S-bearing molecules.

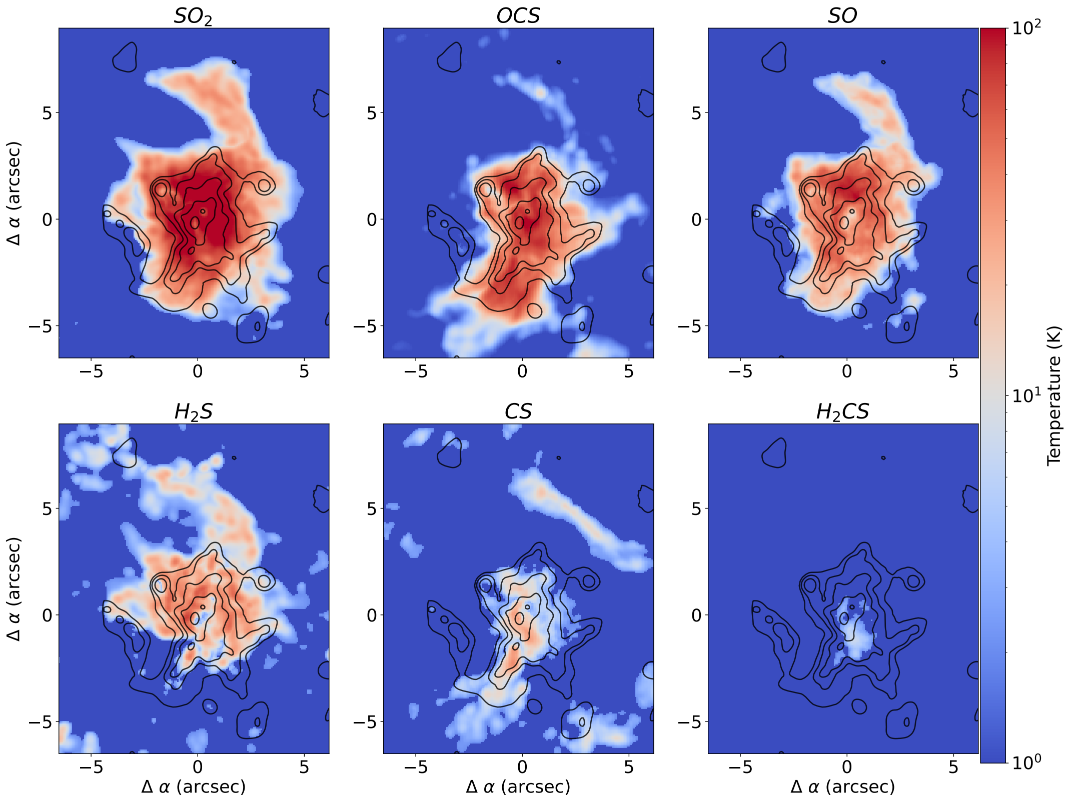

Figure 6.3: Spatial distribution of sulfur-bearing molecules in Sgr B2 (Main) which produced using the line-stacking method. The black contour shows the 1.3 mm continuum map of Sgr B2 (M)

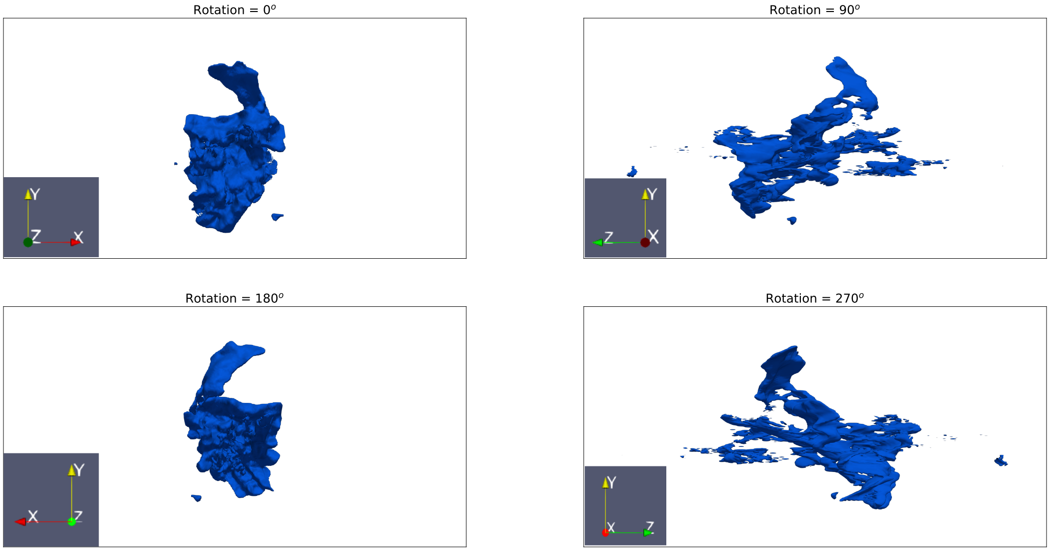

Figure 6.4: 3D structure of SO_2 molecule in Sgr B2 (Main) which are produced by line stacking method. The x-axis and y-axis show the spatial coordinate of the cloud, and the z-axis shows the velocity of SO_2 molecule

6.2 Chemical structure

The line survey toward Sgr B2 (M) showed much compact and rich chemistry from previous research. This section aims to understand the chemistry properties and chemical

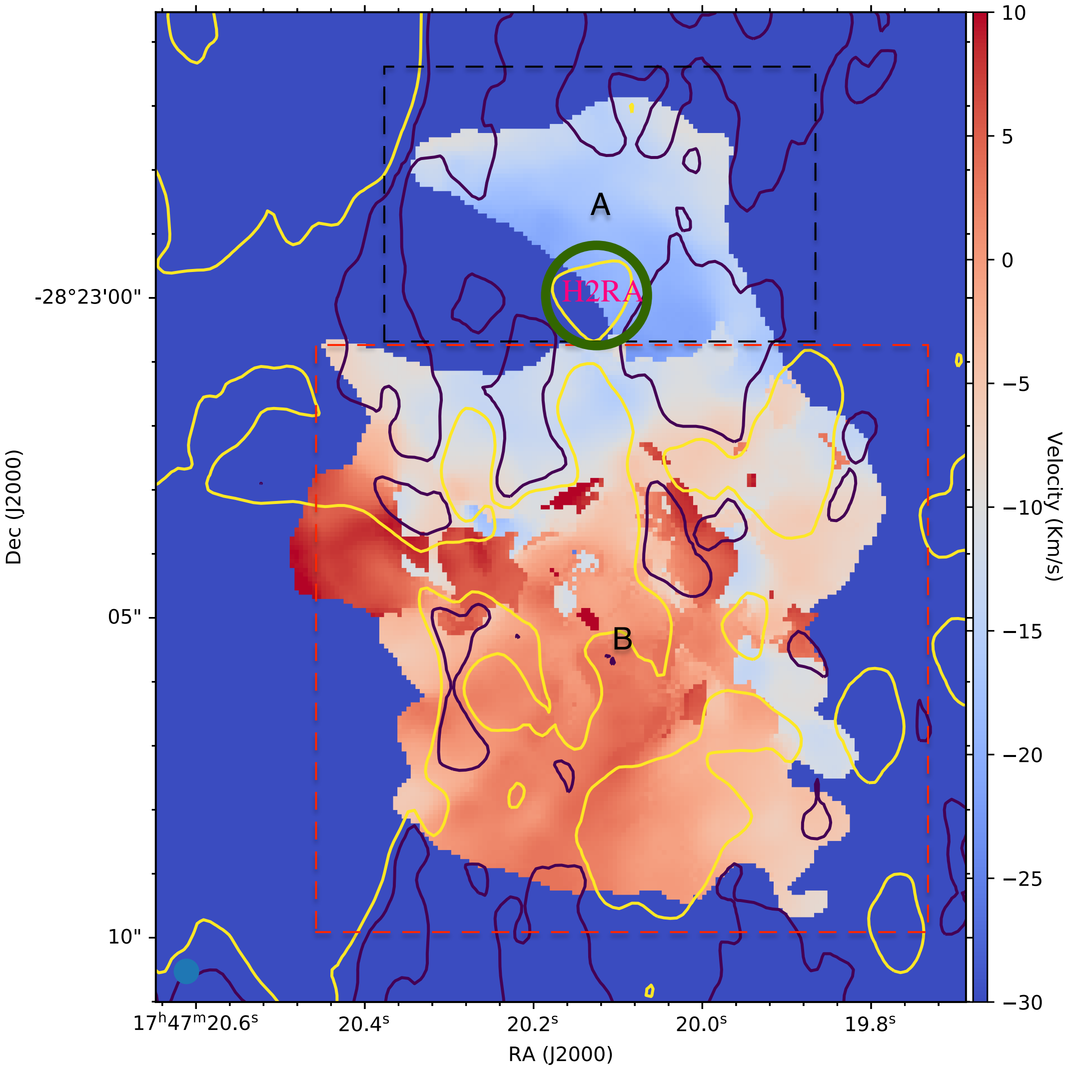

Figure 6.5: XCLASS produces the peak velocity maps of SO_2, the yellow contour shows the HII regions, and we defined the one specific HII region the H2RA region (the green circle), where the high-mass stars are forming, and the stellar wind from the region breaks the cloud into two regions A (black dashed rectangle) and B (red dashed rectangle).

evolution in Sgr B2 (M). We thus target the sulfur-bearing species such as SO_2, OCS, CS, H_2CS, H_2S using XCLASS to derive the column density and temperature of molecules in each spaxel, then create the temperature and column density map of molecules in Sgr B2 (M).

XCLASS enables fitting molecular transitions by solving the 1D radiative transfer equation. Sgr B2 (Main) has high H_2 densities ($> 10^5$ cm^{-3}), hence LTE conditions can be as-sumed (Mangum & Shirley, 2015). By assuming local thermal equilibrium (LTE) conditions, the kinetic temperature of the gas can be estimated from the rotation temperature: $T_{rot} = T_{kin}$.

As we can see in the 3d map of Sgr B2 Main (Fig. 6.4), the cloud has multiple velocity components, and there is only one velocity component in the extended region in the northern part of the cloud (A region in Fig 6.5). However, there are numerous velocity components in the hot core. Because of the high density and high temperature in the

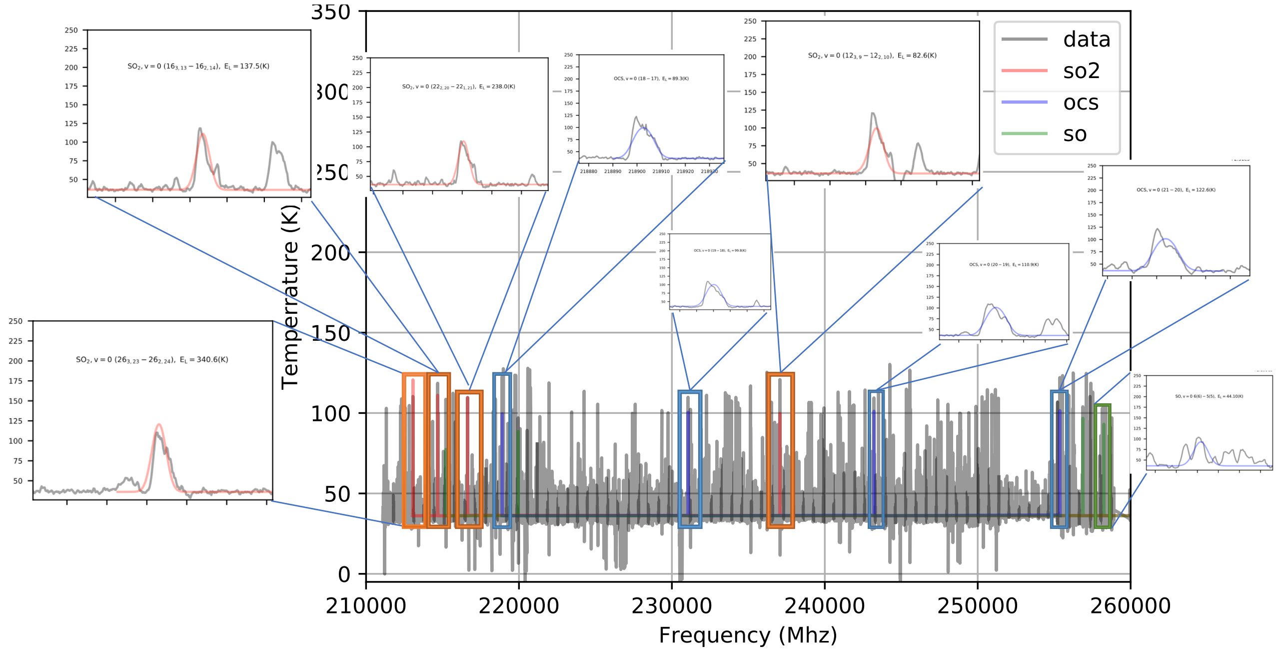

Figure 6.6: SO_2, OCS and SO molecules fitted by XCLASS

hot core, there are multiple high mass star formations in that region, which can produce outflows and affect the structure of the molecular cloud Sgr B2 (Main). The number of velocity components in hot cores is high (4 to 6 components), so in this region, we chose the main component (the velocity component in which the most molecules can be found at the given pixel) to plot them in 2d (velocity map of SgrB2 (Main)).

The 6.5 has shown the velocity map of SO_2 molecule in SgrB2 (Main). As I mentioned above, the two regions, A and B, are classified. Region A represents the region affected by HII expansion, blue-shifted, and the velocity is around -20 km/s. Region B represents the region nearby the core and the south of the core.

6.2.1 Temperature distribution in Sgr B2 (Main)

Figure 6.7 shows the temperature and column density map of SO_2, which varies from 50K to 600K. The temperature around the core is hotter than in the outer regions. Region A has a temperature of around 200-300K. The temperature of the core of the cloud is relatively high $\sim 500K$

As we mentioned above (in section 4.2), we assumed the temperature of SO_2 and other S-bearing molecules in the main component are identical.

Fig 6.7 has shown the temperature of SO_2, and we can recognize that the temperature of the cloud ranges from 50 to 600 K. Based on the temperature of SO_2 molecules in the Sgr B2 (Main), we can classify the B region (classified in Fig. 6.5) into three parts:

- The region is located inside the green ellipse (shown in Fig. 6.7), which overlaps the continuum map (region sgrm1).
  The temperature in this region is relatively high (higher than 250 K). The density in this region is also high. Based on the previous researches (Pols et al., 2018) and (Meng et al., 2019), there are numerous HII regions in this region, which conclude that the region is a highly active high mass star-forming region. In the 3d map of the

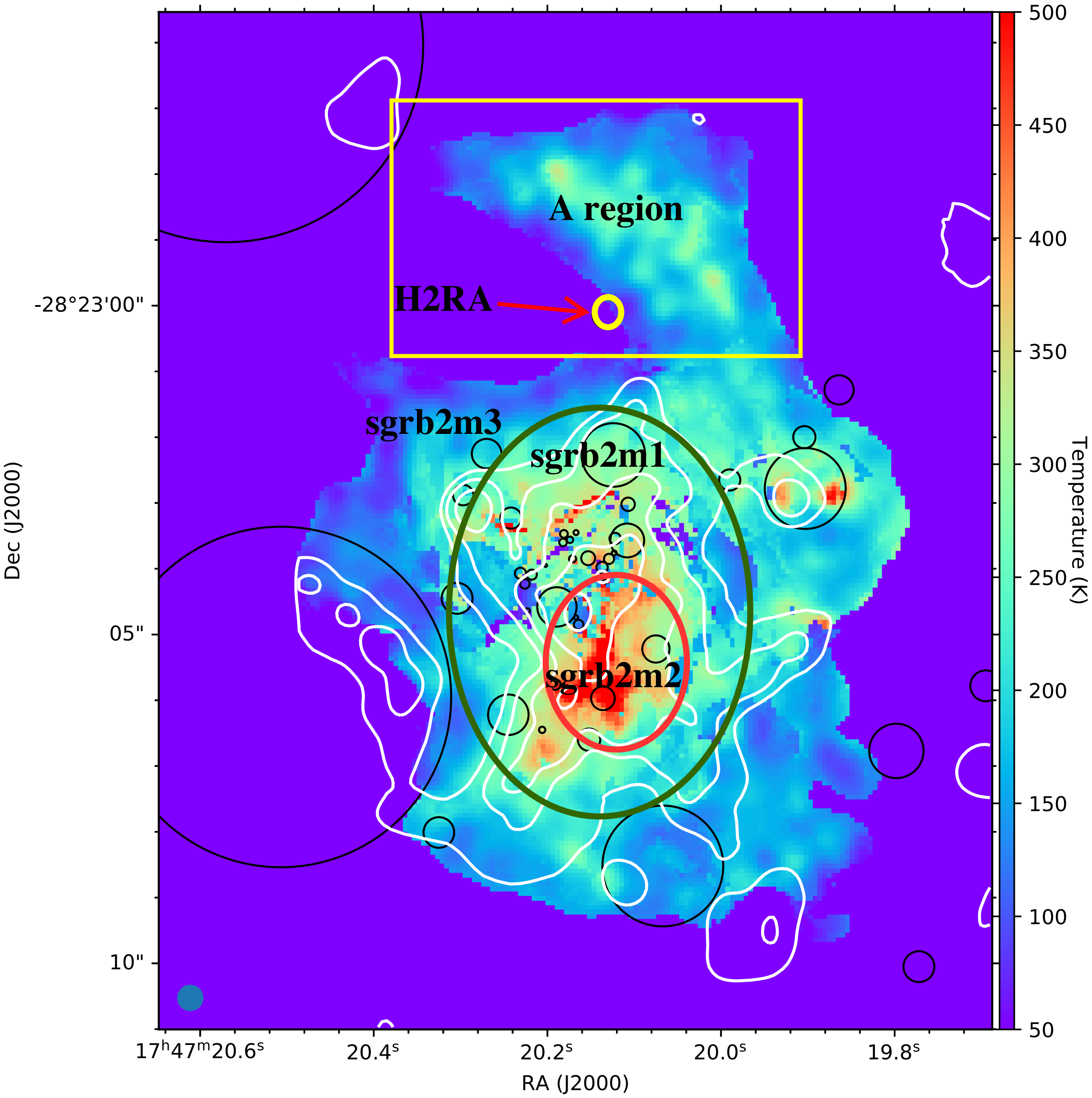

Figure 6.7: The temperature maps of SO_2 derived by XCLASS. From the temperature map, we define the three regions: sgrb2m1 (the region inside green ellipse), sgrb2m2 (the region inside red ellipse), and sgrb2m3 (the region outside green ellipse). The temperatures of these regions are different, which impact the chemistry and abundance of the individual region.

cloud, we can see that there are multiple velocity components in this region which may cause by the outflow in the high-mass star-forming region. Moreover, using the line-stacking method to survey the cloud, we find that this region contains the most complex organic molecules in the Sgr B2 (Main), such as H_2CS, CH_3OH, CH_3CN, C_2H_5CN. We will pay more attention to this region to find the COMs mentioned in the outlook.

- The hot core (region sgrb2m2) is located inside the red ellipse (shown in Fig. 6.7)

The temperature of this region is the highest in Sgr B2 (Main)(higher than 400 K), high-density regions, and actively massive star-forming regions.

- The outer region is located outside the green ellipse (shown in Fig. 6.7), which does not overlap the continuum (sgrb2m3)
  The temperature of this region, the extended region of the cloud, is lower than the inner region. The density in this region is not high as the inner region.

There is one other region, region A (defined in Fig. 6.5). From the 3d map and velocity map of Sgr B2 (Main), this region may be formed by the activities of a high-mass star (the HII region H2RA). The stellar wind from the massive stars may destroy or remove the molecular gas and create a cavity that separates the northern cloud and creates the cloud's northern part. The temperature in this region is pretty high (>200 K). There are some parts in which temperature can reach 350 (K).

6.2.2 Column density distribution of the molecular cloud

In this subsection, we use the definition of the three regions (sgrb2m1, sgrb2m2, sgrb2m3), which are shown in Fig. 6.7, to explain the difference in abundance of S-bearing molecules in these regions.

Fig 6.8 shows the column density of SO_2 molecules in Sgr B2(M), and we can see that the column density of SO_2 molecule is high ($10^{18} \rightarrow 10^{19}$ cm^{-2}) in the sgrb2m1 region, where is the massive star-forming region. In the sgrmb2m3 region, where is the outer region, the column density is lower ($10^{16} \rightarrow 10^{17}$ cm^{-2}) than the inner region, this region is the extended region, so the SO_2 molecules in this region may be formed in a long time ago. The column density of region A is almost the same as the sgrb2m3 region. The SO_2 molecules in region A may have been formed a long time ago or formed through the shock caused by the stellar wind (created by the massive star formation in the H2RA region is shown in Fig. 6.5), which we discussed above in the temperature of Sgr B2 (Main) part. In the histogram plot on the right-hand side, we can identify the column density of SO_2 molecule in the cloud ranges from $10^{15} - 10^{19}$ cm^{-2}. The standard deviation is around $10^{16} - 10^{17}$ cm^{-2}. Comparing the spatial distribution of SO_2 and the histogram plot we can estimate the column density of SO_2 molecule in the outer region is around $10^{16} \rightarrow 10^{17.5}$ cm^{-2}, and the column density in the inner region is around $10^{17.5} \rightarrow 10^{18}$ cm^{-2} .

The column density map of OCS (Fig 6.9) shows the spatial distribution of the OCS molecule in Sgr B2 (Main). The column density of OCS molecules derived by using XCLASS and SO_2 derived temperatures. The molecule is located in the sgrb2m1 region. These results can be explained that OCS can form in high temperature and high-density regions. However, we could not find the OCS molecules in the extended region because of the sensitivity and the telescope's detector. The column density map of OCS has shown that the column density of the chemical in the inner is higher than the outer region. We also find some OCS in the northern part of the cloud (region A), but the column density of OCS in this part is low, and the intensity of OCS in this region is low. In the histogram of the map on the right-hand side, we can identify the column density of OCS molecule in the cloud ranges from $10^{15} - 10^{18}$ cm^{-2}.

Fig 6.10 shows the column density of SO molecules in Sgr B2(Main), and we see that the spatial distribution of SO and SO_2 molecules in the cloud are almost the same, but the

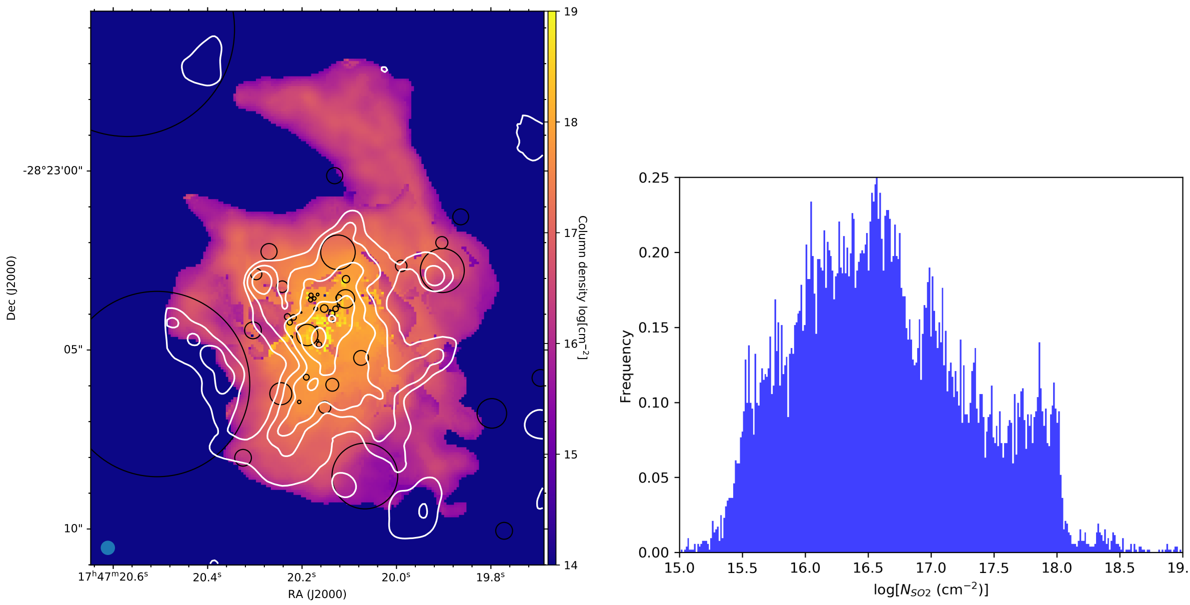

(a) (b)

Figure 6.8: **Left panel:** The column density maps of SO_2 derived by XCLASS, the white contour shows the continuum map of the cloud Sgr B2 (Main) and the black circles indicate the position of HII regions (shown in Fig. 6.2), the definition of the three regions (sgrb2m1, sgrb2m2, sgrb2m3) is shown in Fig. 6.7. **Right panel:** The histogram of SO_2 column density derived by XCLASS.

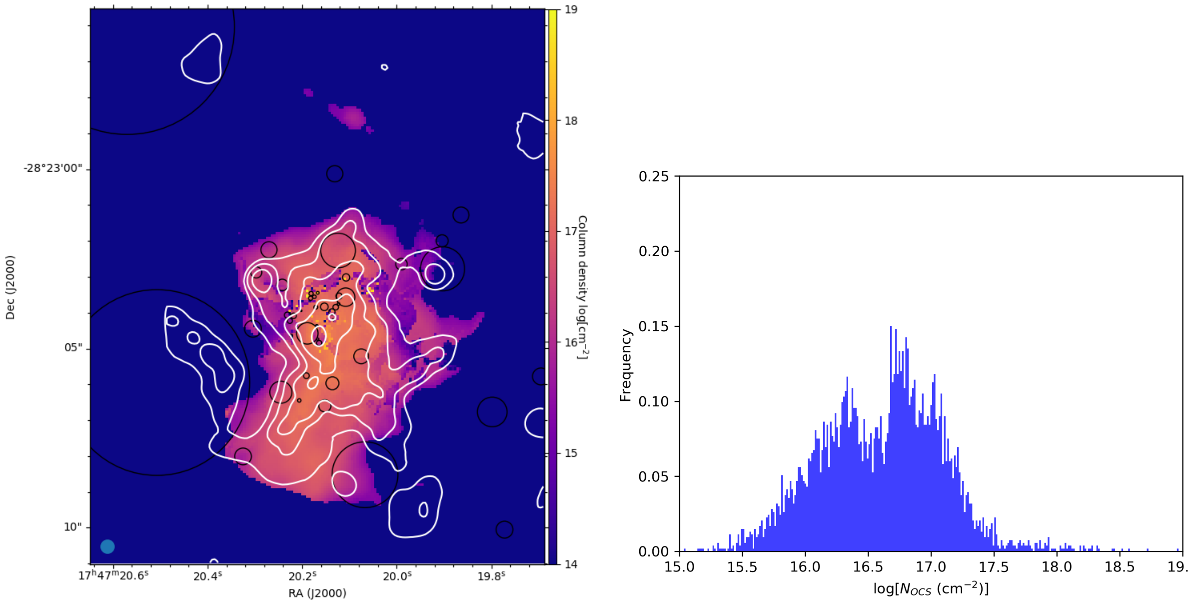

(a) (b)

Figure 6.9: **Left panel:** The column density maps of OCS derived by XCLASS, the white contour shows the continuum map of the cloud Sgr B2 (Main) and the black circles indicate the position of HII regions (shown in Fig. 6.2), the definition of the three regions (sgrb2m1, sgrb2m2, sgrb2m3) is shown in Fig. 6.7. **Right panel:** The histogram of OCS column density derived by XCLASS.

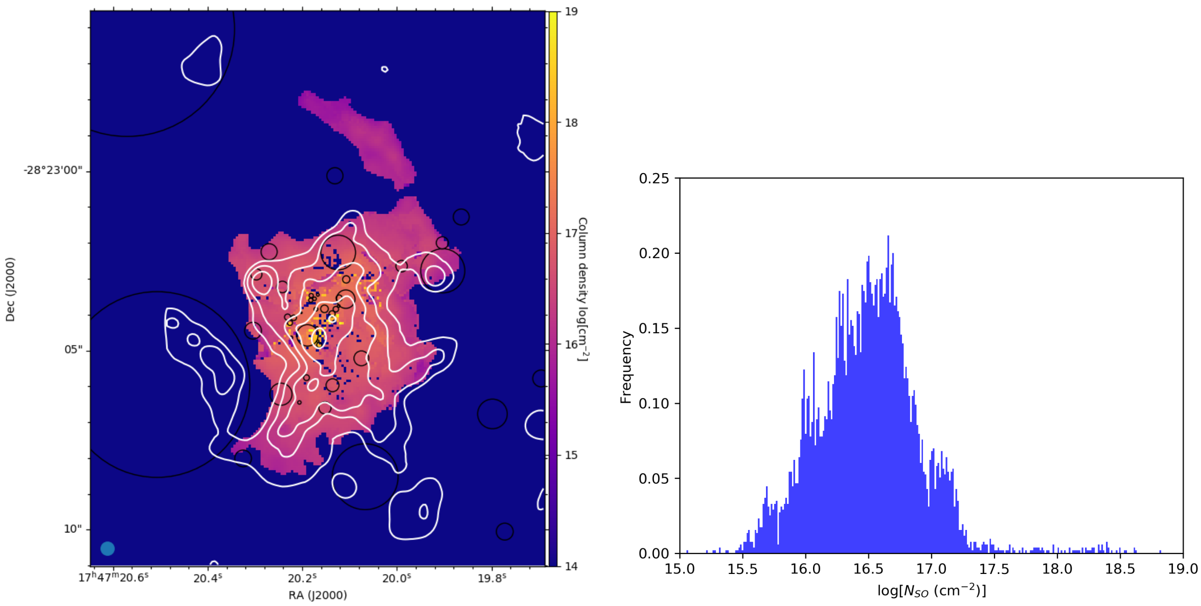

(a) (b)

Figure 6.10: **Left panel:** The column density maps of SO derived by XCLASS, the white contour shows the continuum map of the cloud Sgr B2 (Main) and the black circles indicate the position of HII regions (shown in Fig. 6.2), the definition of the three regions (sgrb2m1, sgrb2m2, sgrb2m3) is shown in Fig. 6.7. **Right panel:** The histogram of SO column density derived by XCLASS.

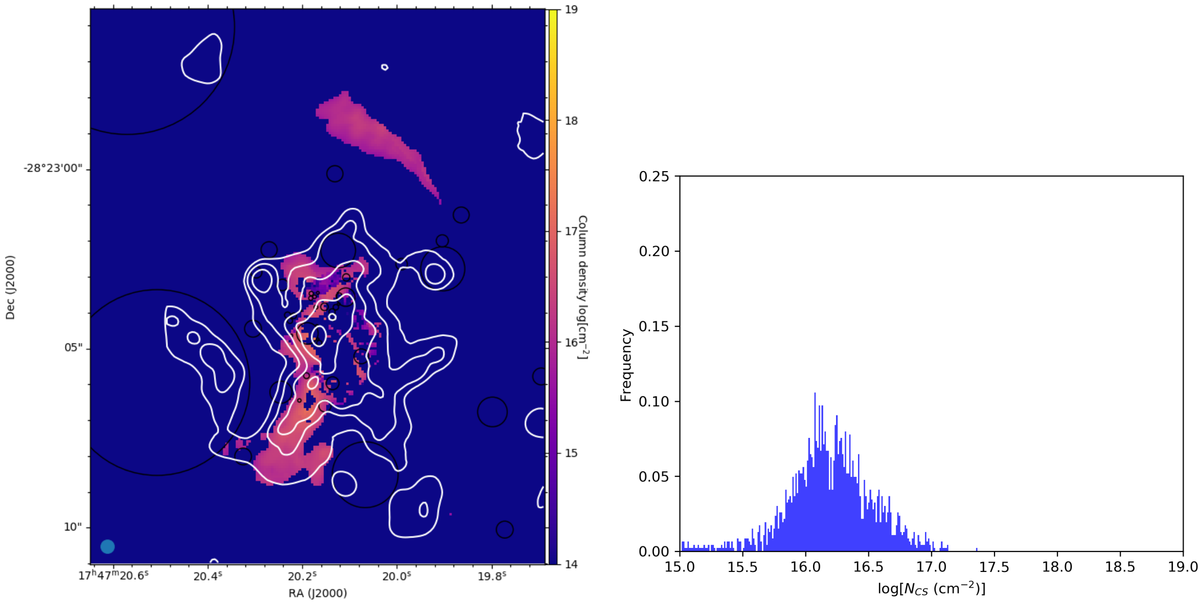

(a) (b)

Figure 6.11: **Left panel:** The column density maps of CS derived by XCLASS, the white contour shows the continuum map of the cloud Sgr B2 (Main) and the black circles indicate the position of HII regions (shown in Fig. 6.2), the definition of the three regions (sgrb2m1, sgrb2m2, sgrb2m3) is shown in Fig. 6.7. **Right panel:** The histogram of CS column density derived by XCLASS.

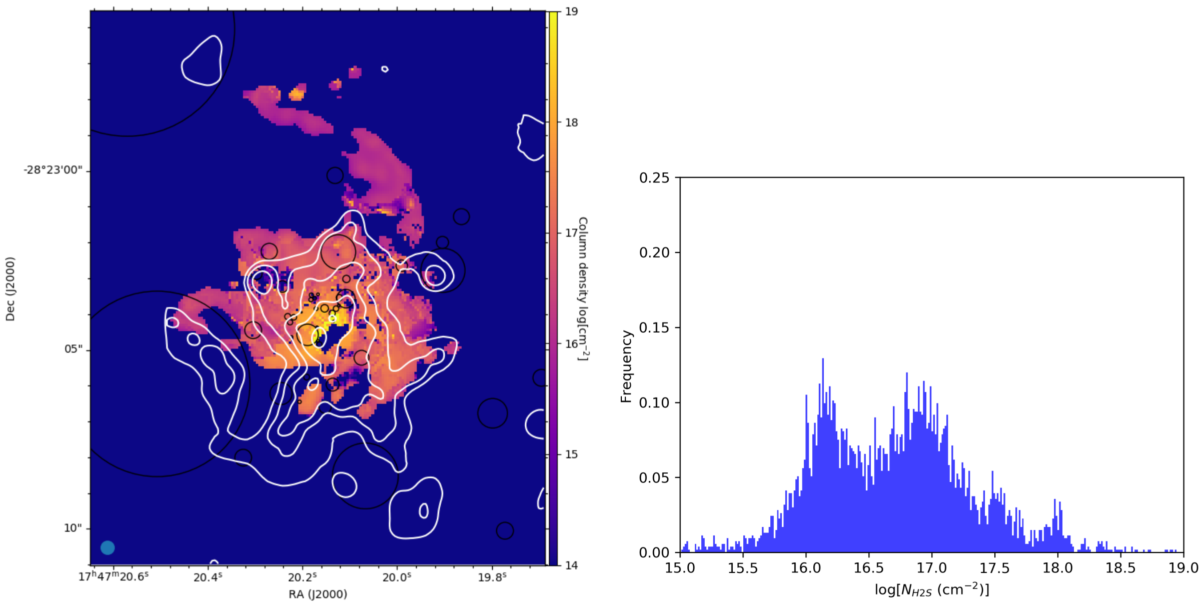

(a) (b)

Figure 6.12: **Left panel:** The column density maps of H_2S derived by XCLASS, the white contour shows the continuum map of the cloud Sgr B2 (Main) and the black circles indicate the position of HII regions (shown in Fig. 6.2), the definition of the three regions (sgrb2m1, sgrb2m2, sgrb2m3) is shown in Fig. 6.7. **Right panel:** The histogram of H_2S column density derived by XCLASS.

spatial distribution map of SO_2 molecules is more extended than SO molecule. We can find SO molecules in the sgrb2m1 region and region A. Because the intensity and number of transitions of SO molecules in our data are not high, we cannot determine the column density of SO in an extended region, and SO molecules can be formed in the hot core (sgrb2m1 region) and the (region A). Our simulation will show the connection between SO_2 and SO molecules. In the histogram of the map, we can identify the column density of SO molecule in the cloud ranges from $10^{15.5} - 10^{17.5}$ cm^{-2}.

Fig 6.11 shows the column density of CS and the histogram of the molecule in Sgr B2(M). In our data, the line emission of $C^{32}S$ is optically thick and shows that we cannot use the line emission of the molecule to derive the column density of the molecule. We have to use the $C^{34}S$ which is an isotope of $C^{32}S$, and transition lines of the isotope are stronger than other isotopes of CS molecules in our data. We can derive the column density of the isotope and use the ratio of $^{32}S/^{34}S$ equal to 13 (Möller et al., 2021) to calculate back the column density of $C^{32}S$. Since there are problems in calculating the column density of CS, we use the column density map of CS as a reference to know the spatial distribution of the molecules. We see that the chemical is located in the inner part (sgrb2m1) and the northern part (region A). Because of the self-absorption and the absorption of the other line, we cannot see the CS molecule in the sgrb2m2 region. The CS molecules present in region A prove that there are shocks in this region. The necessity of the shock in CS formation is introduced in the introduction. In the histogram plot, we identify the column density of CS molecule in the cloud ranges from $10^{15.5} - 10^{17}$ cm^{-2}.

Fig 6.12 shows the column density of H_2S in Sgr B2 (M). There are only two transition

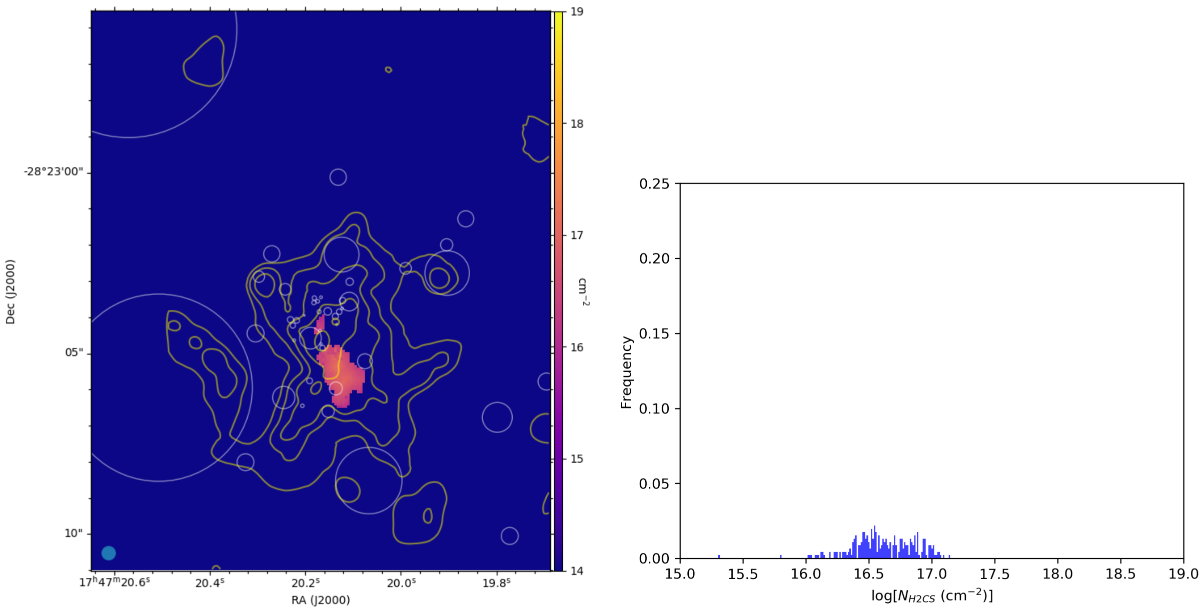

(a) (b)

Figure 6.13: **Left panel:** The column density maps of H_2CS derived by XCLASS, the yellow contour shows the continuum map of the cloud Sgr B2 (Main) and the white circles indicate the position of HII regions (shown in Fig. 6.2), the definition of the three regions (sgrb2m1, sgrb2m2, sgrb2m3) is shown in Fig. 6.7. **Right panel:** The histogram of H_2CS column density derived by XCLASS.

lines of H_2S in our data, so we cannot be certain of the column density of this molecule. However, we could use the column density map as the reference to compare with other molecules. The map shows the spatial distribution of H_2S in the molecular cloud. The H_2S molecules can form in the shock regions, and the formation of the molecules in shock through the chemistry equations (Williams, Hartquist, Rawlings, Cecchi-Pestellini, & Viti, 2017).

$$\mathrm{S} + \mathrm{H_2} \longrightarrow \mathrm{SH} + \mathrm{H} \tag{6.1}$$

$$\mathrm{SH} + \mathrm{H_2} \longrightarrow \mathrm{H_2S} + \mathrm{H} \tag{6.2}$$

The molecule can be found in the northern part of the B region and the A region (defined in Fig. 6.5). The histogram of the column density of H_2S shows the column density of H_2S molecule in the cloud ranges from $10^{15} - 10^{18.5}$ $\mathrm{cm^{-2}}$.

Fig 6.13 shows the column density of H_2CS molecule, like CS, H_2S, the number of and the intensity of the H_2CS is low, the column density of H_2CS is uncertain. Nevertheless, the column density map confirms that we can find the H_2CS molecules in Sgr B2 (M), and most of them are located in the sgrb2m2 region. The histogram shows the column density of H_2CS molecule in the cloud ranges from $10^{16} - 10^{17}$ $\mathrm{cm^{-2}}$ as references.

6.2.3 Comparion of molecules depend on the temperature

To understand the effect of the temperature on the chemistry of the S-bearing molecules, we produced plots of the molecules' column density depending on the temperature. However, the temperature can affect the abundance of molecules, but the total column density of molecules also depends on the total H_2 column density.

In Fig. 6.14, We see that the plot of temperature and column density of SO_2 molecules is a good correlation. The increasing of the temperature from 50 (K) to 400 (K), the column density of SO_2 increases from $10^{15.5}$ cm^{-2} to 10^{18} cm^{-2}.

For SO molecules, in the range of temperature from 50 to 400 K, SO molecules' column density increases when the temperature increases. In the range of high temperature (>400 K), the column density of SO molecules is around 10^{17} cm^{-2}. This uncorrelation of the temperature and column density can be caused by the high total H_2 column density in the hot core (high temperature).

There is a lot of scattering in the correlation plot of temperature and column density for OCS molecules. It seems that the column density of OCS molecules depends on the temperature, but the molecule is not strongly affected by temperature.

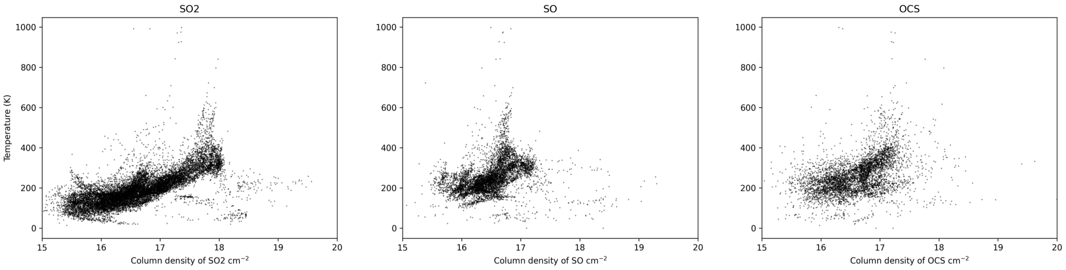

Figure 6.14: The correlation of column density (logarithmic scale) and temperature of SO_2, SO, OCS molecules in Sgr B2(M)

Comparing the correlation of temperature and column density of SO_2, SO, OCS molecules, we see that they are affected by temperature. The effect of temperature on SO_2, SO, and OCS will be discussed in the astrochemistry simulation.

Part IV

Astrochemistry modeling of Sgr B2 (Main)

Chapter 7

Astrochemistry models

In the previous chapters, I showed how I used observational data to derive the physical properties of the Sgr B2(M) molecular cloud. This chapter shows the results of the time-dependent chemical simulations based on the physical information of the Sgr B2(M) molecular cloud from previous studies. We use the astrochemical code Saptarsy (Choudhury et al., 2015) to compute time-dependent chemical abundances and study the mechanisms responsible for producing the sulfur-bearing molecules. In particular, we investigate the influence of different environmental factors (the cosmic-rays ionization rate (CRIR), density distribution, thermal evolution) and the intrinsic factors of molecules: the desorption energy of some molecules, which affects the abundances.

The modification of models are:

1. We study the influence of cosmic rays on molecular cloud chemistry, where we change the CRIR value from a factor of 1-100 to the standard parameter.
2. The influence of the density distribution of molecular clouds, by changing the density and exponent of the Plummer-like function (η)
3. The effect of the thermal evolution of the cloud
4. Finally, we study the influence of OCS and SO's desorption energy to see how they impact the abundance of molecules.

7.1 Motivation

In order to simulate the time-dependent physical and chemical evolution of Sgr B2(M) and explain the formation and destruction of specific sulfur-bearing molecules which were detected toward the cloud, we use the astrochemical code Saptarsy to investigate the impact of physical conditions on the abundances of the molecules and compare the physical parameters which are derived from the observations.

As already mentioned, Sgr B2(M) is embedded in the Galactic center region, which CRIR is expected higher than in the solar neighborhood. In order to investigate the influence of cosmic rays on chemistry and the abundances of molecules and constrain the simulation to observations toward Sgr B2(M), we are modeling the molecular cloud in different cosmic rays conditions.

Moreover, based on the previous results of the physical structure and physical properties of Sgr B2 (Schmiedeke et al., 2016), which found that the density field of Sgr B2 can be fitted by a superposition of spherical symmetric density cores with Plummer-like profiles, we are continuing to study how the Plummer profiles and density of the cloud impact on the chemical evolution.

7.1.1 Cosmic rays ionization rate

In my thesis, I choose a standard value of $\zeta = 1.3 \times 10^{-17}\ s^{-1}$ which value was estimated the cosmic rays ionization rate in dark clouds (Duley & Williams, 1993). Moreover, (Barger & Garrod, 2020) determined the cosmic-ray ionization rate range from around 2 to 20 time the standard value ($1.3 \times 10^{-17}\ s^{-1}$) which model fit hot core observational sources, NGC 6334 IRS 1, NGC 7538, W33A, and W3(H_2O), Furthermore, (Bonfand et al., 2019) studied the influence of cosmic-ray in Sgr B2 (North). They found the best fit between chemical models and observations in which the value of CRIR is $7 \times 10^{-16} s^{-1}$ (around 50-time standard value). I constrained the cosmic rays value in the range 1-100 times the standard value in my research.

7.1.2 Changing the cloud's density distribution

Density of the cloud

Based on the results of observation and analysis of dust emission, (Sánchez-Monge et al., 2017) have calculated the distribution of Sgr B2 (M) $10^7 \rightarrow 10^8$ cm^{-3}. We choose max density equal to 10^8 cm^{-3} corresponding to 9×10^7 at 1/2 FWHM of r = 2000 AU and change the density in the range $2 \times 10^7 \rightarrow 1.8 \times 10^8$ cm^{-3} to see the impact of the density in the evolution in molecules‘ abundance.

In this section we keep the Plummer-like function exponetial value of 4.0 and the standard value of CRIR = 1.3×10^{-17} s^{-1}.

Changing the exponent of Plummer-like function (η)

We use a Plummer-like function (shown in equation 7.1) to model the density profile of the cloud.

$$n(r)\left(\mathrm{cm}^{-3}\right) = 2n_c\left(1+\left(\frac{r}{r_p}\right)^2\right)^{-\eta} \tag{7.1}$$

In this equation:

- The Plummer radius: r_p in cm
- The central density n_c in cm^{-3}

We defined the molecular cloud structure by giving the structure of the modeling grid, which is a single spherical symmetric grid for the whole cloud. Based on the previous research of our group (Schmiedeke et al., 2016), which used the exponent of Plummer-like function equal to $\eta = 4.0$ to analyze the physical properties of the SgrB2 (Main).

By changing the exponent of the Plummer-like functions (the original Plummer function has a fixed $\eta = 5/2$) of the cloud, we are changing the density distribution of the whole molecular cloud, and we can understand how the density distribution of the cloud impacts astrochemistry.

We modified the exponent of Plummer-like function value from 1.0 → 8.0 to investigate the impact of the exponent of Plummer-like function on the astrochemistry.We keep the central density equal to 1.8×10^8 cm^{-3} and the standard value of CRIR equal 1.3×10^{-17} s^{-1}.

7.1.3 Influence of thermal evolution

The chemical unity of the cloud is strongly influenced by temperature and thermal evolution. When the temperature of the cloud changes, the reaction rate coefficient change, and as the temperature decreases, the reaction rate constant decreases. Since the reaction rate constant depends on the temperature, the Arrhenius equation

$$k = Ae^{-\frac{E_A}{RT}} \tag{7.2}$$

shows how the temperature affects the reaction rate.

In my thesis, we modify the thermal evolution of the stellar evolution in the Hosokawa model (Fig. 5.6), which is provided by (Hosokawa & Omukai, 2009). We change the total luminosity of the cloud by multiplying its total luminosity with an s-factor.

7.1.4 Desorption energy of SO and OCS molecules

Furthermore, we are also interested in the binding energies for species on water ice surfaces. In this study, we based on Wakelam's research (Wakelam, Loison, Mereau, & Ruaud, 2017) to change the binding energy of molecules on the grain surface, so I changed the binding energy of SO and OCS molecules on the surface to see how they impact the molecules' abundance.

7.2 The reference model

In this step, we determine the reference model, which can analyze the effects of physical parameters.

Firstly, we have to compare the physical and chemical model with benchmarks from other models, and there is a master thesis in our group (Schaefer, 2017) that already analyzed the models and compared the outcomes with the multi-phase model of (Vasyunin & Herbst, 2013) and with the observational data of (Öberg et al., 2011). The thesis found that the Saptarsy model is improved by using the multilayer model, which is more realistic than the older model.

The physical model in the thesis is the molecular cloud which has an initial density of $n_{H_0} = 3.10^3$ cm^{-3}. Then the molecular cloud evolves after $t = 10^6$ years to receive the final density at the core of $n_H = 10^7$ cm^{-3}. the initial temperature of the cloud is $T_i = 20K$ and the final temperature of the cloud equals $T_f = 10K$. The absolute abundances of molecules will be used as the initial abundances for all zone in the warm-up phase. In this phase, they used 25 zones with the final zone is 10^4 AU and the Plummer function equals

Table 7.1: The parameters in our astrochemical models

Parameter	Symbol	Unit	Value
Grain shape			spherical symmetric
Grain Composition			carbonaceous
Grain radius	r_d	μm	0.1
Grain Mass density	ρ_d	g/cm^3	3.0
Grain density of sites	Σ_{sites}	1/cm^3	1.5×10^{15}
Distance between sites	d_{site}	Å	$1/\sqrt{\Sigma_{sites}} = 2.58$
Number of sites	$N_s(l)$		$4\pi(r_d + l d_{site})^2 \Sigma_{sites} = 1.885 \times 10^6$
Dust to gas mass ratio	$m_{d/g}$		1%/1.0975
Barrier thickness for tunneling	b	Å	1.0
Binding to desorption fraction	E_b/E_D		0.3
Reactive desorption energy			0.01
Cosmic Ray heating temperature	T_{CR}	K	70
Cosmic Ray ionization rate	ζ_{CR}	1/s	1.3×10^{-17}
Sticking probability of species	P_{stick}		(0 for ions) 1
Number of layer segments	N_{seg}		4
Number of surface layers	N_{SL}		4
Include Photo Reactions	FLAG(5)		True
Usege of the Multilayer Approach	FLAG(6)		True
Growth of sites per layer	FLAG(6b)		$(N_s(l) = N_s(0))$ FALSE
Bury atoms in mantle	FLAG(8)		False
Read provided E$_b$	FLAG(9)		False
Use reactive diffusion competition	FLAG(10)		False
Chemical Network			OSU 334 species
Physical model			cold and warm-up

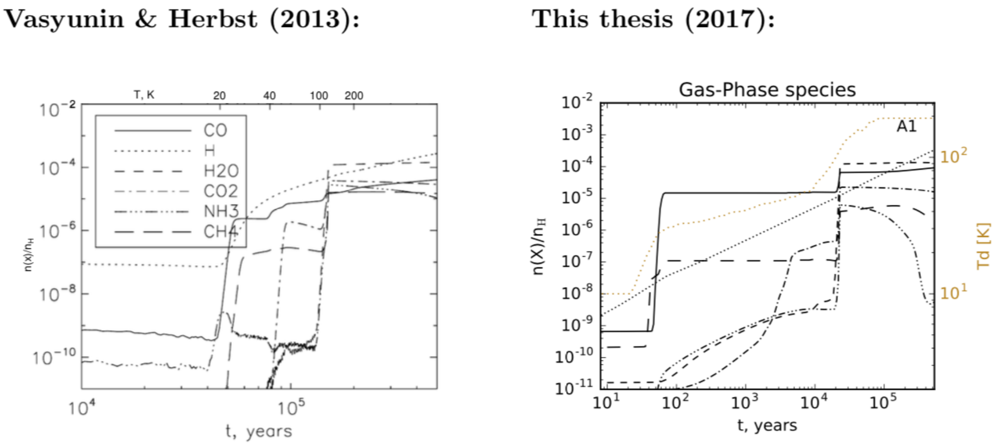

Figure 7.1: Comparison between the multi-phase model (Vasyunin & Herbst, 2013) and reference model in the warm-up phase (Schaefer, 2017). The gas-phase abundances for some selected species.

$\eta = 2.5$. The comparisons of the benchmark model and the previous result are shown in the figure 7.1.

In this thesis, we found the limitation of the benchmark model, which we have to compute the final density in the cold collapse phase to make them compromise with the initial densities in the warm-up phase. Moreover, we want to compare our models with our ALMA data, and we should change the physical parameters such as temperature and the density distribution of the cloud.

7.3 Evolution of molecule abundances in molecular cloud

The evolution of molecule abundances can be explained by: in outer region (R_1, R_3 in Fig 7.2) abundances of molecules strongly depend on the cold collapse phase. The inner region in time step $10^4 \to 10^6$ (R_3, R_4 in Fig 7.2) strongly depends on the molecules' total reaction rate.

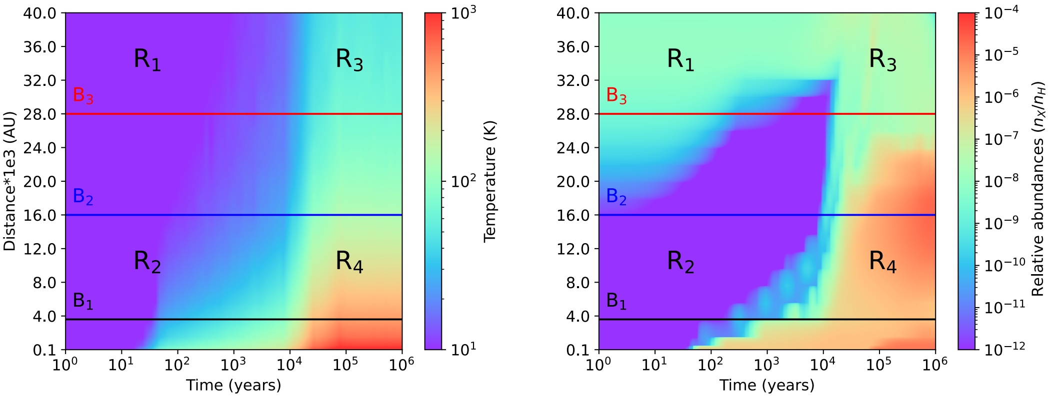

Figure 7.2: The evolution of SO_2 abundances in the molecular cloud is divided into four regions: R_1, R_2, R_3, R_4 on the right-hand side. The thermal evolution of the molecular cloud shows on the left-hand side, which can explain the effectiveness of the changing density of the cloud. Moreover, the molecules' abundance in the cloud is affected by the temperature, the outer regions of the cloud are not heated much, and therefore the abundances stay the same

The physical properties of the 4 regions: R_1, R_2, R_3, R_4 can be classified:

- R_1: low density ($d \sim 10^4 \to 5 \times 10^5$ cm−3), low temperature (T $= 10 \to 20$ K)
- R_2: high density (d $\sim 5 \times 10^7 \to 3 \times 10^8$ cm−3), low temperature (T $= 10 \to 20$ K)
- R_3: low density (d $\sim 10^4 \to 5 \times 10^5$ cm−3), relative high temperature (T ~ 100 K)
- R_4: high density (d $\sim 5 \times 10^7 \to 10^8$ cm^{-3}), high temperature (T $\sim 10^3$ K)

The explanation of the influence of changing density can be based on the changing of physical properties on R_1, R_2, R_3, R_4 regions. When we change the density, the exponent of Plummer-like function, or the thermal evolution of the cloud, those changes will affect the abundance of molecules. We will look in more detail at how those conditions affect the abundances of molecules in the next chapter.

Moreover, we are comparing the time dependent abundance of sulfur-bearing molecules at 3 specific distances: $B_1 = 4.058 \times 10^3$ AU, $B_2 = 16.315 \times 10^3$ AU , and $B_3 = 28.177 \times$

Table 7.2: Physical properties of R_1, R_2, R_3, and R_4 regions

Region	Density (cm^{-3})	Temperature (K)	n_{SO_2}/n_H
R_1	$10^4 \rightarrow 5 \times 10^5$ (low)	10-20 (low)	$\sim 10^{-8}$
R_2	$10^6 \rightarrow 2 \times 10^8$ (high)	10-20 (low)	$\sim 10^{-12}$
R_3	$10^4 \rightarrow 5 \times 10^5$ (low)	100-200 (relatively high)	$\sim 10^{-7}$
R_4	$10^6 \rightarrow 2 \times 10^8$ (high)	10^3 (high)	$\sim 10^{-4 \rightarrow -6}$

10^3 AU. By using the plot of time dependent abundance of molecules, we can understand more about the formation and destruction of different molecules at some specific times.

7.4 Total reaction rate

To understand the chemistry evolution in molecules cloud, we are using the reaction rate of several vital chemical reactions of sulfur-bearing molecules and some particular molecules affected by changing condition models such as changing cosmic rate ionization rate of the whole cloud. We classified the reaction rate of molecules into formation and destruction reactions. For instance, we are using some formation, destruction reaction of SO_2 to explain the reaction rate of molecules and calculation the total reaction rate.

The total reaction can help us know where molecules are formed or destroyed at the specific time step. The calculation of the total reaction rate requires the abundances of molecules calculated by the astrochemistry code Saptarsy.

Formation

- $SO_2^+ + O_2 \longrightarrow O_2^+ + SO_2$; $\dfrac{d[SO_2]}{dt} = v_{f_1} \Rightarrow d[SO_2] = v_{f_1} dt$
- $HSO_2^+ + H_2O \longrightarrow H_3O^+ + SO_2$; $\dfrac{d[SO_2]}{dt} = v_{f_2} \Rightarrow d[SO_2] = v_{f_2} dt$
- $HSO_2^+ + NH_3 \longrightarrow NH_4^+ + SO_2$; $\dfrac{d[SO_2]}{dt} = v_{f_3} \Rightarrow d[SO_2] = v_{f_3} dt$

$$d[SO_2] = \sum_{i=1}^{n} v_{f_i} dt \quad \text{; which } \sum_{i=1}^{n} v_{f_i} \text{ is total formation reaction rate.}$$

Destruction

- $SO_2 \rightarrow SO + O$; $\dfrac{d[SO_2]}{dt} = v_{d_1} \Rightarrow d[SO_2] = v_{d_1} dt$
- $C^+ + SO_2 \rightarrow SO^+ + CO$; $-\dfrac{d[SO_2]}{dt} = v_{d_2} \Rightarrow -d[SO_2] = v_{d_2} dt$
- $He^+ + SO_2 \rightarrow S^+ + O_2 + He$; $-\dfrac{d[SO_2]}{dt} = v_{d_3} \Rightarrow -d[SO_2] = v_{d_3} dt$

$$-d[SO_2] = \sum_{i=1}^{n} v_{d_i} dt \quad \text{; which } \sum_{i=1}^{n} v_{d_i} \text{ is total destruction reaction rate.}$$

Total reaction rate:

$$d[\mathrm{SO_2}] = \left(\sum_{i=1}^{nf} v_{f_i} - \sum_{i=1}^{nd} v_{d_i} \right) dt$$

Total abundance of SO_2:

$$[\mathrm{SO_2}] = \int \left(\sum_{i=1}^{nf} v_{f_i} - \sum_{i=1}^{nd} v_{d_i} \right) dt$$

The rate of single formation and destruction reaction (v_{f_i} and v_{d_i}) can be derived from output Saptarsy. As we mentioned above, we can get each molecule's abundance, reaction rate, and chemical reaction by solving the rate equation.

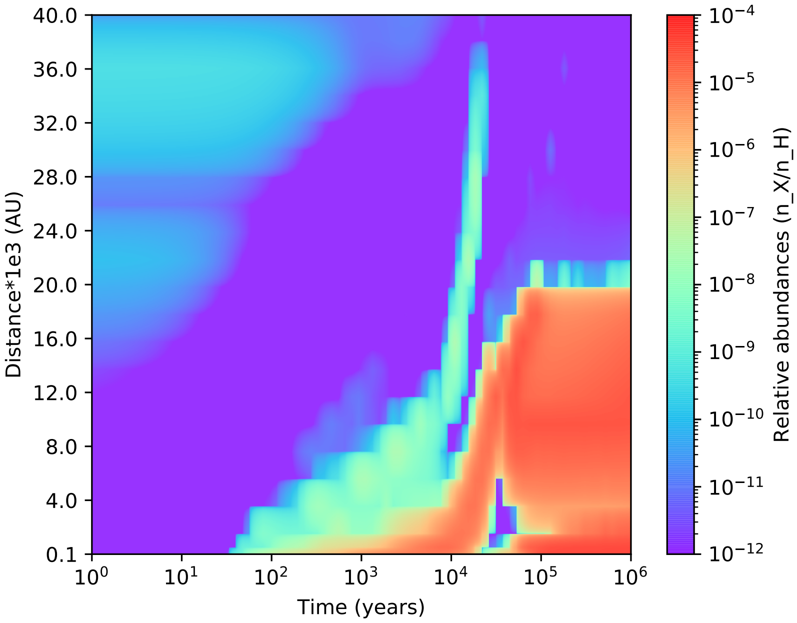

Figure 7.3: Relative abundances of SO_2 as a function of time (x-axis) and distance from the center of molecular cloud (y-axis)

To simplify, we can use the equation to compute the total reaction of SO_2 molecule in each time step.

$$\frac{[\mathrm{SO_2}]_{t+1} - [\mathrm{SO_2}]_t}{\text{time step}_{t+1} - \text{time step}_t} \tag{7.3}$$

In the Fig 7.3 and Fig 7.4 we can see the relative abundance of SO_2 is strongly depend on the total reaction rate. In the next section, we will show how the relative abundances of molecules are affected by different physical conditions.

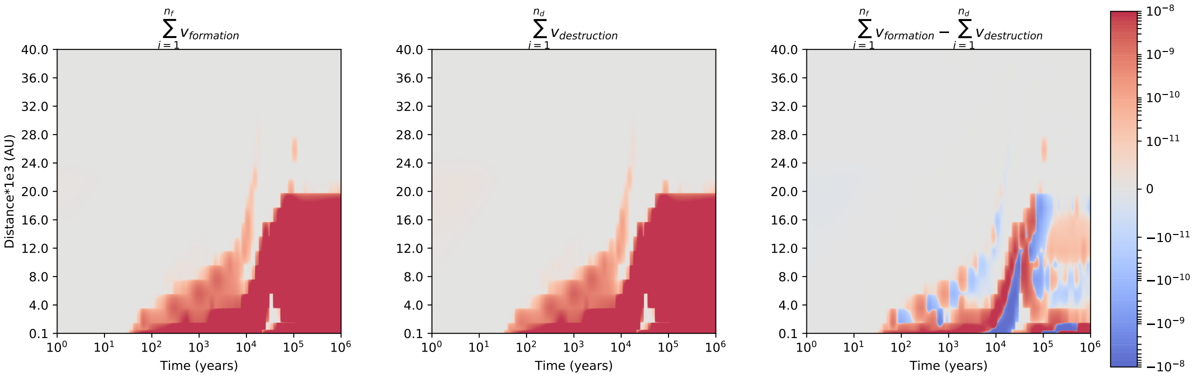

Figure 7.4: Formation reaction rate, destruction rate, and total reaction rate of SO_2, in the total reaction rate of SO_2 figure (right figure), the blue region corresponding to areas of net destruction of SO_2 and the red area is where SO_2 is forming.

Chapter 8

Chemical Model Results and Analysis

8.1 The impact of cosmic rays in S-bearing molecules

The abundance of S-bearing molecules is impacted by ions. He^+, ${H_2}^+$, H^+ which are produced through the cosmic rays ionization process. The ions strongly influence the formation and destruction of sulfur-bearing molecules. For H_2S molecule, the two most molecules involve in its formation are S^+ and HS^+ (which is formed by reacting with ${H_3}^+$)

Moreover, the photo destruction due to cosmic rays processes strongly impacts the abundance of S-bearing molecules. Cosmic rays penetrate deeper into a molecular cloud than ultraviolet photons and ionize H_2 molecules and Hydrogen atoms. This primary process excites other H_2 and generates exciting Hydrogen atoms, which radiative decay generates an ultraviolet flux (Prasad & Tarafdar, 1983) (Shen, Greenberg, Schutte, & Van Dishoeck, 2004). Those UV photons can interact with other molecules and destroy them to form smaller molecules or ionize the S atom.

$$\mathrm{S + CRP \longrightarrow S^+ + e^-} \tag{8.1}$$

In addition, under the the effect of the cosmic rays, the sulfur atom will be ionized (ionization potential of sulfur equal to 10.36 eV) by the chemical reaction 8.2 to form S^+.

$$\mathrm{H^+ + S \longrightarrow S^+ + H} \tag{8.2}$$

The figures 8.1 shows the chemical network of S-bearing, which reactions are a high reaction rate and strongly affect the abundance of molecules. Most molecules are forming from the desorption process and grain surface reaction, and they are destroyed by reacting with ${H_3}^+$, H^+, He^+.

The chemical network of SO_2 and SO in figure 8.1 shows the most of SO_2 molecules are formed by SO molecules reactions, and the formation of SO, OH, O_2 molecules are strongly impacted by ions ${H_3}^+$, H^+, He^+ which are created by cosmic rays. The abundance of SO_2 and SO is also impacted by the photodissociation induced cosmic rays process through the reactions

$$SO_2 + CRP \longrightarrow SO + O \tag{8.3}$$

$$SO + CRP \longrightarrow S + O \tag{8.4}$$

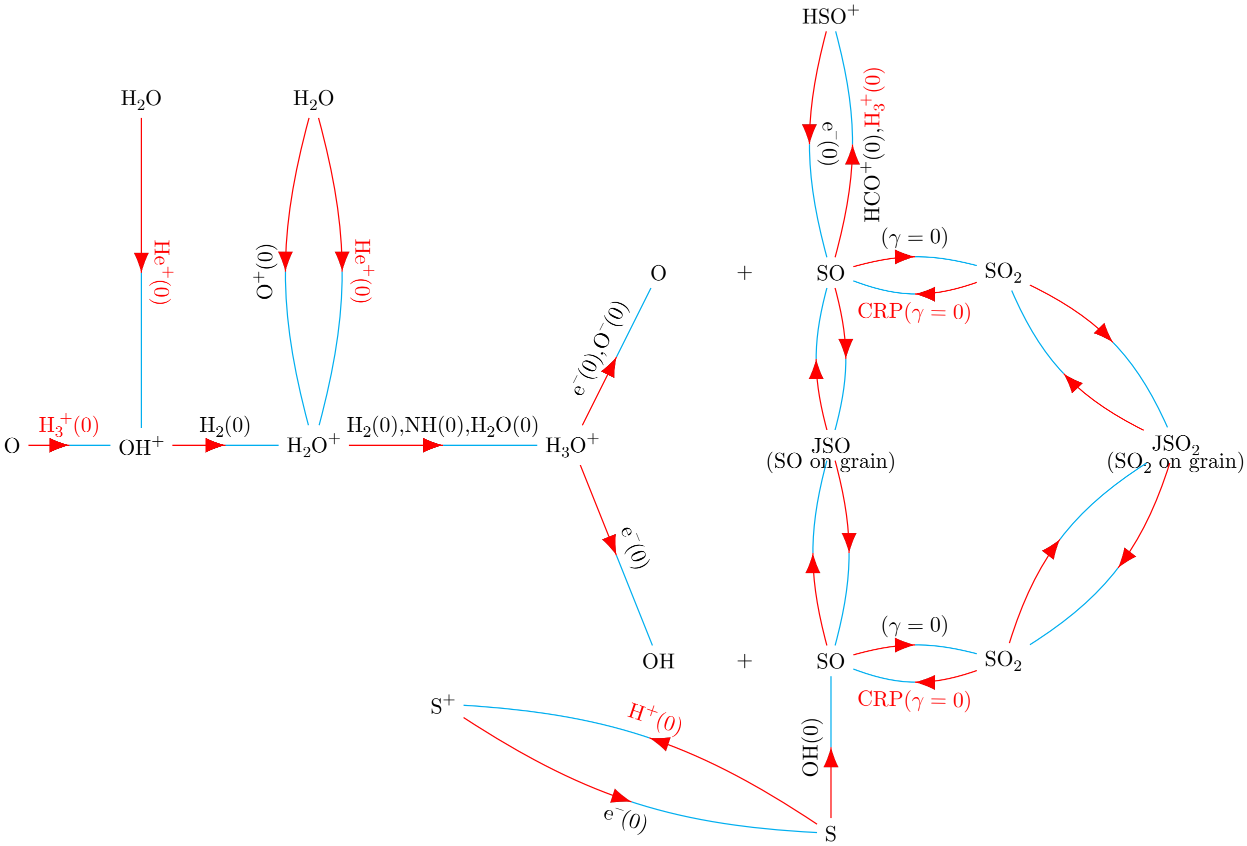

Figure 8.1: the formation reactions of SO and SO_2 molecules impacted by cosmic rays. γ is the activation barrier (in Kelvin) in parentheses, we divided the arrow into two parts (blue and red) to illustrate the molecule in the blue arrow is formating and the molecule in the red arrow is destroying.

8.2 Influence of cosmic rays on the chemistry of S-bearing molecules

Cosmic rays are an essential factor in the evolution of chemical complexity in the interstellar medium (Indriolo et al., 2015). This section explores the influence of cosmic rays ionization ray (CRIR) on chemistry and, in particular, its impact on the production and destruction of sulfur-bearing molecules. Cosmic rays play an essential role in chemistry during the cold collapse and warm-up phases.

The CRIR directly impacts the chemical process in molecular cloud:

1. On grain surface: the dissociation of molecules on the grain surface influences the number of reactive radicals on the grain surface.
2. In the gas phase:
    - The CRIR controls the density of ions in the molecular cloud and ion-molecule reactions, which mainly impact forming and destroying molecules.
    - Destroying molecules through photodissociation induced cosmic rays

The essential ionization caused by cosmic-ray protons (CR) in dense clouds interact with molecule H_2 to form essential ionization through the reaction

$$H_2 + CR \rightarrow H_2^+ + e^-$$

. Then H_2^+ immediately reacts with H_2 to form the ion H_3^+ :

$$H_2^+ + H_2 \rightarrow H_3^+ + H$$

Cosmic rays also ionize helium atoms to form the ion He^+. Those ions (H^+, H_3^+, He^+) affect the formation and destruction of sulfur-bearing molecules. We will look in more detail, how cosmic rays impact S-bearing molecules.

In this section, we compares the effects of cosmic ray ionization on the chemistry and abundance of S-bearing molecules. By changing the cosmic ray ionization rate (ζ_{CR}) from $\zeta_{CR1} = 1.3.10^{-17}$ to $10 \times \zeta_{CR1}, 20 \times \zeta_{CR1}, 50 \times \zeta_{CR1},$ and $100 \times \zeta_{CR1}$, we see the effect of cosmic ray ionization rate on the abundances of sulfur-bearing molecules, and understand the effects of cosmic ray into chemical evolution of molecular cloud and the chemical reaction rates.

Table 8.1: The parameters of the chemical models for Sgr B2 (M)

CRIR (ζ)	Abbreviation	(η)	s-factor	Density (cm^{-3})
1.3×10^{-17} s^{-1}	ζ_{CR1}	4.0	1.0	1.8 $\times 10^8$
$10 \times 1.3 \times 10^{-17}$ s^{-1}	ζ_{CR10}	4.0	1.0	1.8 $\times 10^8$
$50 \times 1.3 \times 10^{-17}$ s^{-1}	ζ_{CR50}	4.0	1.0	1.8 $\times 10^8$
$100 \times 1.3 \times 10^{-17}$ s^{-1}	ζ_{CR100}	4.0	1.0	1.8 $\times 10^8$

8.2.1 Cold collapse

The cold collapse phase covers the pre-stellar and early cold stages of the free-fall collapse. The reactions on the grain surface in this phase rule the chemistry. In this phase, the visual extinction increases, the dust temperature falls from 20 to 10 K, and molecules on gas-phase freeze onto interstellar dust grains, forming ice mantles.

Under cosmic rays, the molecules in the gas phase can be dissociated by the cosmic rays and photodissociation-induced cosmic rays. When the cosmic rays enhance, the S-bearing molecules are destroyed, impacting the abundance of molecules both on the grain and in the gas phase in the cold collapse phase. The figure 8.2 is shown the changing of the abundance of sulfur-bearing molecules in the cold collapse phase at $t = 10^6$ years

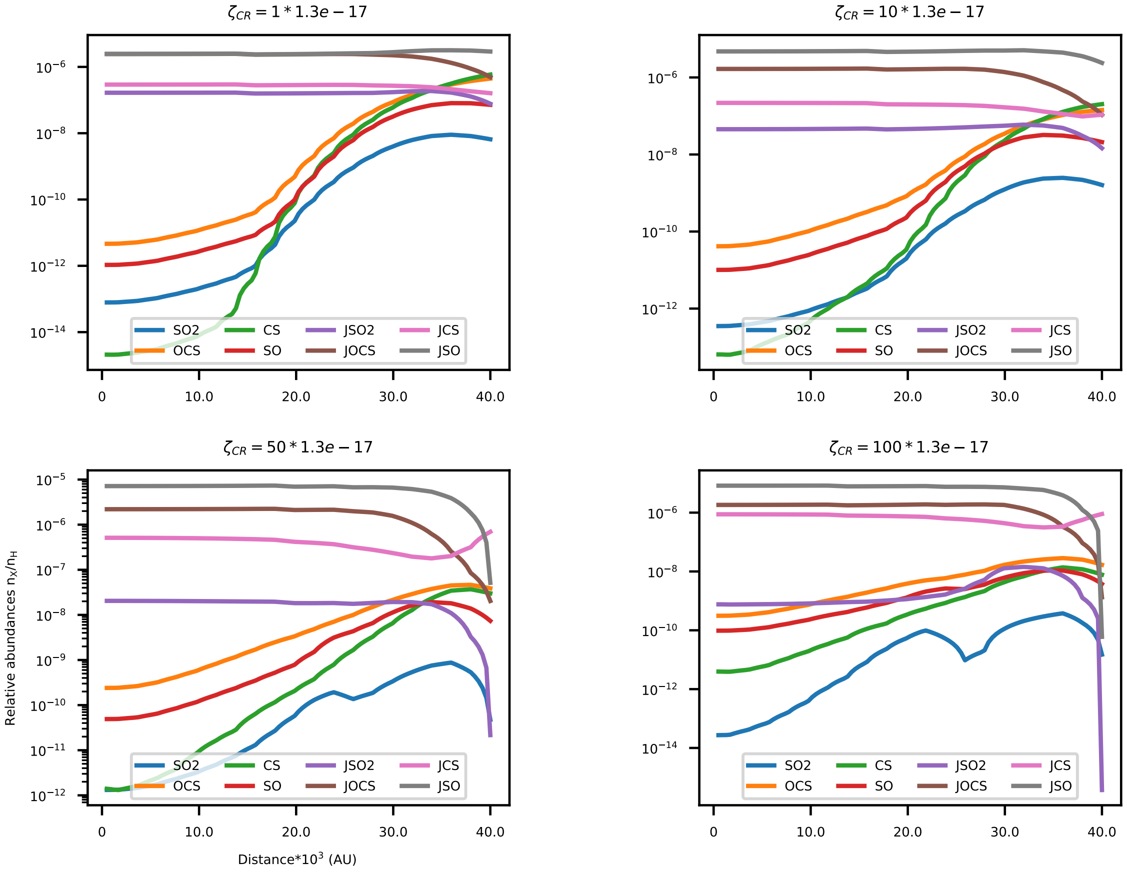

Figure 8.2: The abundances of sulfur-bearing molecules at final time step in cold collapse phase in difference cosmic-ray ionization rate condition

8.2.2 Warm-up phase

The warm-up phase follows the cold collapse phase. The evolving protostar at the center of the molecular cloud heats its surroundings. At early times of the warm-up phase, the temperature of the cloud is low, and ice mantles are still growing by accreting gas-phase species until the temperature is sufficiently high to release molecules on the grain surface into the gas phase.

Like other molecules, sulfur-bearing molecules are formed on the surface of the grains during the cold collapse phase. In the first 50 years of the warm-up phase, the temperature remains low (10K). The molecules in the gas phase continue to freeze out on the grain surface. When the temperature increases, the grains' molecules start to evaporate into the gas, and its gas-phase abundances remain essentially unchanged after 10^4 years (T>100K).

When we increase the CRIR from $\zeta_{CR1} \rightarrow \zeta_{CR100}$, the relative abundance of molecules is affected by cosmic rays. The cosmic process affects the cloud's chemistry through the H_3^+, H_2^+, H^+, He^+, S^+ ions, and through the second photon-induced process, the cosmic rays photon interacts with molecular hydrogen or the dust particles and produce UV photons. The high-energy UV photons can break chemical bonds to form ions or smaller

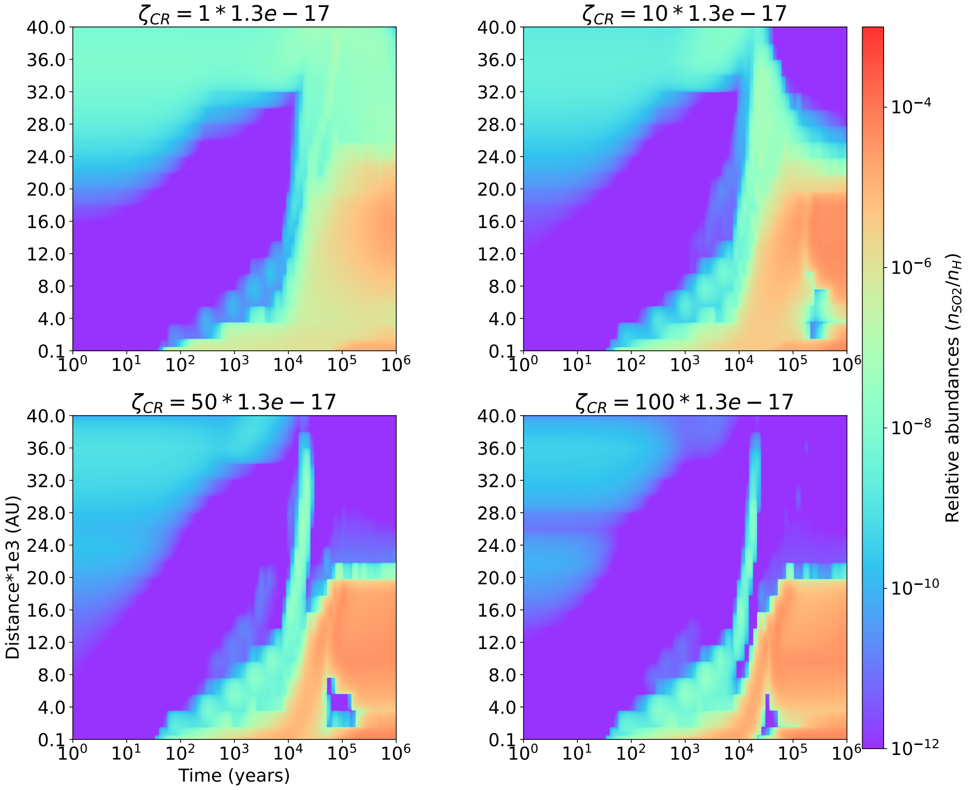

Figure 8.3: The relative abundances of SO_2 as a function of time (x-axis) and distance from the center of molecular cloud (y-axis) with different cosmic rays conditions

molecules, such as bond-breaking reactions of S-bearing molecules

$$SO_2 + UV \longrightarrow SO + O. \tag{8.5}$$

This process also dramatically influences the abundance of S-bearing molecules. Especially considering the decomposition of SO_2, this process significantly affects the abundance of S-bearing.

Moreover, cosmic ray also affects the desorption of molecules on the grain surface; however, this process influence in cold collapse phase due to low temperature (10 - 20 Kelvin). In the warm-up phase, when the dust temperature increase higher than 70-100 Kelvin, most molecules are evaporated into the gas phase, and the cosmic rays do not impact the desorption of molecules in the high-temperature region.

For SO_2 (in Fig 8.3) we can see the abundance of SO_2 is decreased when the CRIR enhance, the forming of H^+, H_3^+ which is destroy the precursors molecules which are froming SO_2

We computed the abundance evolution of molecules in different CRIR conditions, and in the next chapter, we will use those results to compare the observed data to choose which condition agrees with the observation.

8.3 Influence of density

In this section, we explore the influence of cloud density on chemistry and the production of S-bearing molecules.

The density of the molecular cloud also plays an essential role in chemical simulations. In particular, in the early cold collapse phase, the density of the cloud impacts the chemistry of the cloud. By increasing the density, the molecules have more chances to interact. Moreover, the molecules on the gas phase quickly freeze out onto the grain surface (in Fig. 8.5).

In this set, we altered the density of the cloud by changing the inner density of the molecular cloud. The density of the cloud is changed from $0.2\times10^8 \rightarrow 1.8\times10^8$ cm^{-3}. Fig. 8.4 shows how the density of the molecular cloud changes from the core to the outermost region in linear and log scales.

Table 8.2: The parameters which we use to compare the models

Inner density (cm^{-3})	Abbreviation	η	s factor	CRIR ζ s^{-1}
1.8×10^8	n_1	4.0	1.0	1.3×10^{-17}
1.6×10^8	n_2	4.0	1.0	1.3×10^{-17}
1.4×10^8	n_3	4.0	1.0	1.3×10^{-17}
1.2×10^8	n_4	4.0	1.0	1.3×10^{-17}
1.0×10^8	n_5	4.0	1.0	1.3×10^{-17}
0.8×10^8	n_6	4.0	1.0	1.3×10^{-17}
0.6×10^8	n_7	4.0	1.0	1.3×10^{-17}
0.4×10^8	n_8	4.0	1.0	1.3×10^{-17}
0.2×10^8	n_9	4.0	1.0	1.3×10^{-17}

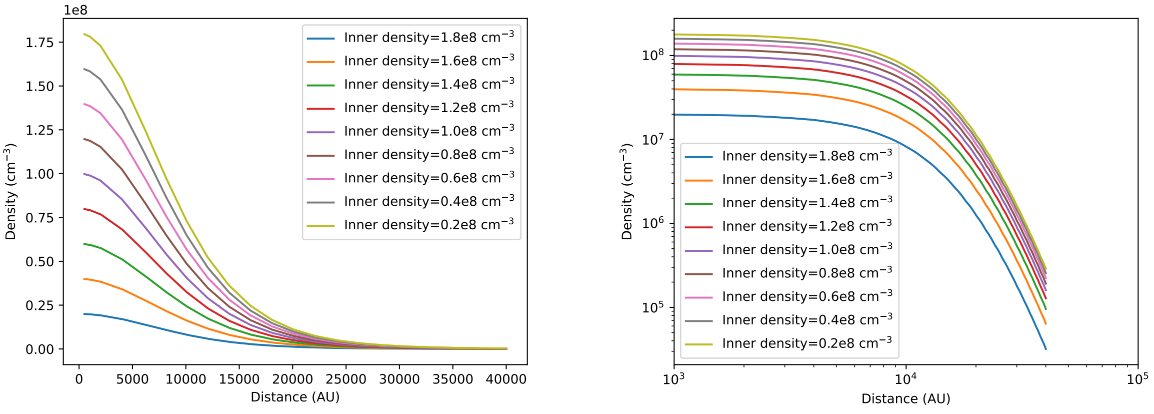

(a) (b)

Figure 8.4: Density of the molecular cloud in different inner density with $\eta = 4.0$. **(a): linear scale**; **(b): log scale**

Fig. 8.5 shows the changing of the relative abundance of S-bearing molecules in the gas phase and on the grain surface at the last time step of the cold collapse phase or the

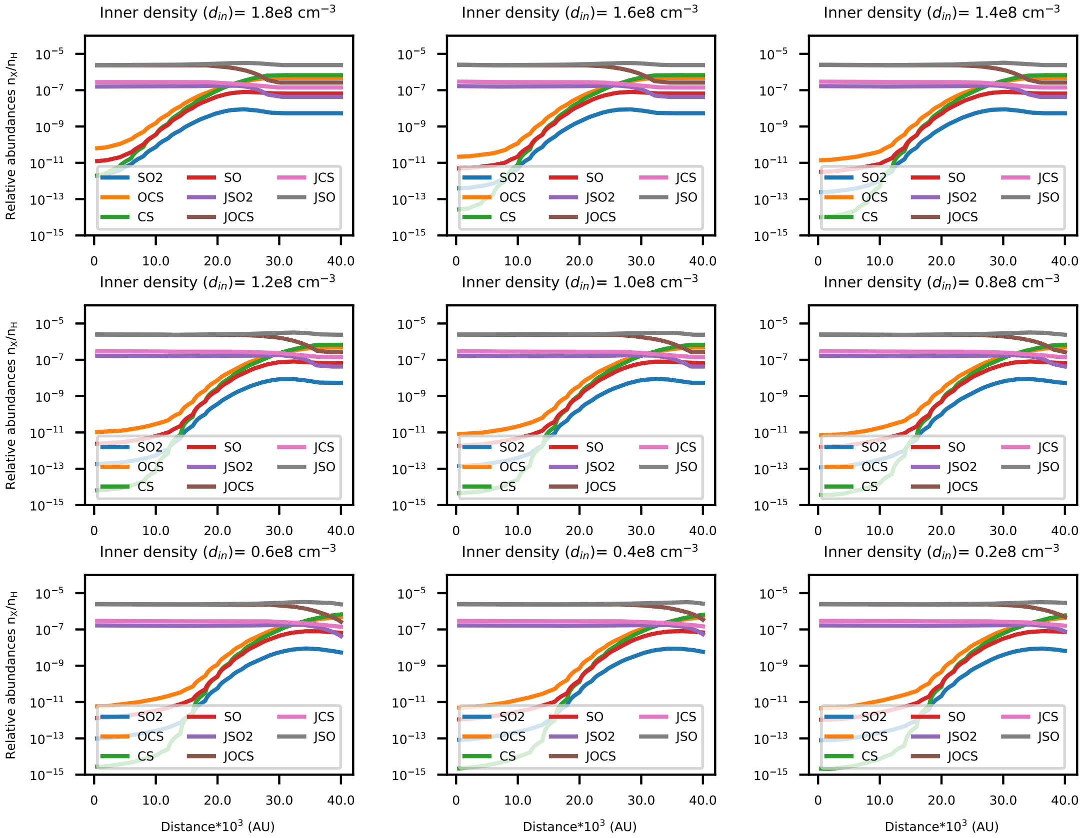

Figure 8.5: The initial abundances of molecules in warm-up phase in the molecular cloud as a function of distance from the center of molecular cloud (x-axis) in different inner density.

initial abundance of S-bearing molecules in the warm-up phase. The higher density, the higher abundance of molecules in the outer region ($20 \times 10^3 - 40 \times 10^3$ AU).

Abundance profiles: In Fig. 8.6 we show the abundance of SO_2 molecule in different density. When we increase the inner density, the abundance of molecules increases.

Following the classification of the evolution of molecular cloud in the section, we classified the change into four regions (Fig 7.2), and we focus on the two last time steps regions: the region R_3 and region R_4.

Firstly, when we change the density of the cloud, the density R_1 changes, and the final abundances of molecules in the cold collapse phase are affected. In the cold-collapse phase, the density increase the molecules have more chances to interact with the grain and freeze on the grain surface.

In the warm-up phase, the temperature of the R_3 region is relatively high (around 100K - 200K), and the density is relatively low, so the change of the density does not impact this region. The R_4 region is high density and high temperature, which is the most impacted region. The molecules in this region are formed in the cold collapse phase, and they will be evaporated and interact with other molecules in the warm-up phase. When we

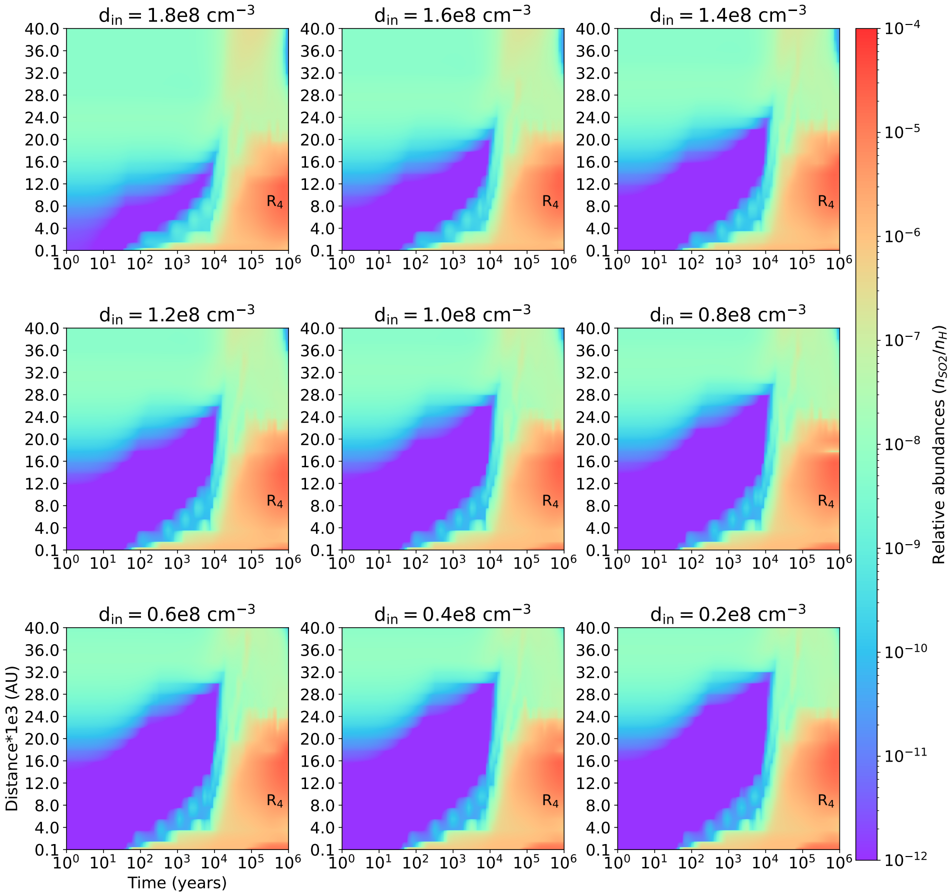

Figure 8.6: The relative abundances of SO_2 as a function of time (x-axis) and distance from the center of molecular cloud (y-axis) in different density

increase the density of the cloud, the total abundances of molecules increase, the number of molecules increases, but they are not homogeneously increased, the abundances of each molecule strongly depend on the total reaction rate. We can see the relative abundances and the total reaction rate of molecules in the appendix (Influence of density).

We can conclude that the R_4 region is the most crucial region and is affected by changing the density of the molecular cloud.

8.4 Influence of density distribution of the molecular cloud

In this section, we are modeling the molecular cloud based on the change of density profile of the cloud. We distinguish eight models with a different exponent of Plummer-like function (η) from 1.0 - 8.0, as seen in Fig. 8.7 and table 8.3.

Density profile: We modified models by changing the exponent of the Plummer-like

Table 8.3: The parameters which we use to compare the models

s-factor	η	CRIR (ζ) s^{-1}	Density (cm^{-3})
1.0	1.0	1.3×10^{-17}	1.8×10^8
1.0	2.0	1.3×10^{-17}	1.8×10^8
1.0	3.0	1.3×10^{-17}	1.8×10^8
1.0	4.0	1.3×10^{-17}	1.8×10^8
1.0	5.0	1.3×10^{-17}	1.8×10^8
1.0	6.0	1.3×10^{-17}	1.8×10^8
1.0	7.0	1.3×10^{-17}	1.8×10^8
1.0	8.0	1.3×10^{-17}	1.8×10^8

function η. The density profile of the molecular cloud is steeper than when we increase an exponent of the Plummer-like function (shown in Fig. 8.7). The η value of the reference model equals 4.0.

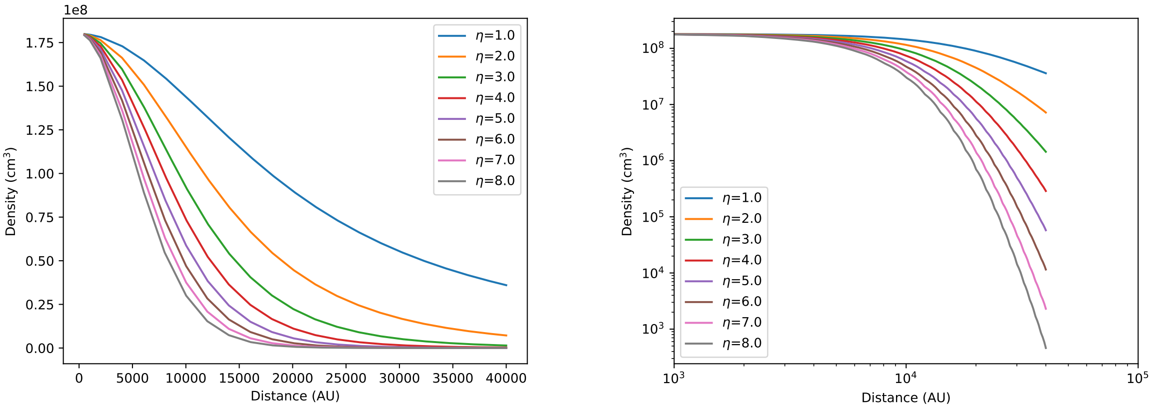

(a) (b)

Figure 8.7: Plummer density profiles for different exponents η with $n_{in} = 1.8 \times 10^8$ cm^{-3}.**(a): linear scale**; **(b): log scale**

When we change the exponent of the Plummer-like function of the cloud, the density of the outer regions (region R_1 and R_3) are changed, but we only concentrate on the late time step (R_3 region). We will look in more detail at how the exponent of Plummer-like function and density of those regions affect the abundances of molecules in R_3 region.

The simulation results of SO_2 molecules in (Fig 8.8) show us how the exponent of the Plummer-like function affects the abundances of the molecules in the warm-up phase.

- In the case of small exponents in the Plummer-like function, the abundance of SO_2 in the R_3 area is high.
- In the case of large exponents in the Plummer-like function, the abundance of SO_2 molecules in the R_3 region is low

When increasing the exponent of the Plummer-like function of the cloud, the density in the R_3 regions is decreased (Fig 8.7), and the absolute abundances of molecules in the cold-collapse phase were affected. The density of the outer area increases from 10^3 cm^{-3}

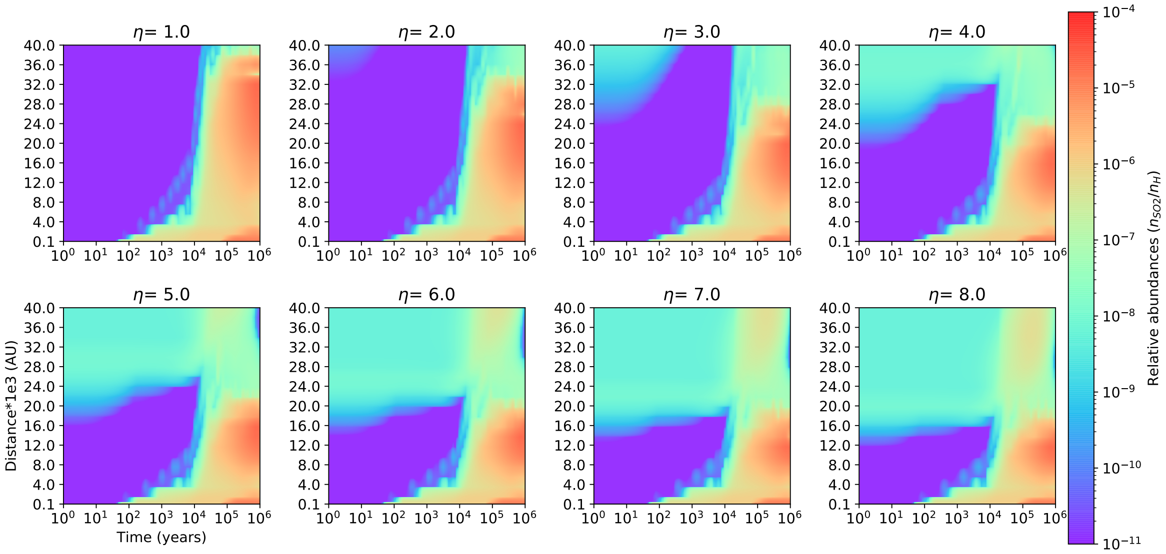

Figure 8.8: The relative abundances of SO_2 as a function of time (x-axis) and distance from the center of molecular cloud (y-axis) in different exponent of Plummer-like function (η)

to 10^5 cm^{-3} (depending on the Plumer function of the cloud), and the temperature drops out from 20 K to 10 K. In high-density and low temperatures, molecules can interact with dust and freeze on their surface. For higher exponents of the Plummer-like function, all of the molecules in the gas phase will freeze on the dust, and in the warm-up phase (increase temperature), all the molecules on the dust evaporate into the gas phase.

In the outer region (distance from the core $> 20 \times 10^3$ AU), when the exponent of Plummer-like function (η) increases from 1.0 to 8.0, the density of the outer area decreases (Fig. 8.8). When the density of the external region decreases (by changing the exponent η), the abundance of molecules in the gas phase increases. The molecules' abundance in the gas phase in the cold-collapse phase leads to the change of the abundance of molecules in the warm-up phase.

8.5 Influence of thermal evolution of cloud

In this section, we modify the thermal evolution of the molecular cloud to see how the temperature affects the astrochemistry of the cloud. In the cold-collapse phase, we keep the thermal evolution of the cloud as the reference model. However, we are changing the s-factor (defined in the subsection 7.1.3 Influence of thermal evolution) of the Hosokawa & Omukai models in the warm-up phase, leading to the change in the temperature of the cloud. Fig. 8.9 shows the changing of the thermal evolution in different models.

The reaction rate of the molecules strongly impacts the abundance of molecules, and the formation and destruction reactions of molecules rate depend on reaction rate coefficient k and abundances of reactant molecules. The chemical reaction rate equation of the

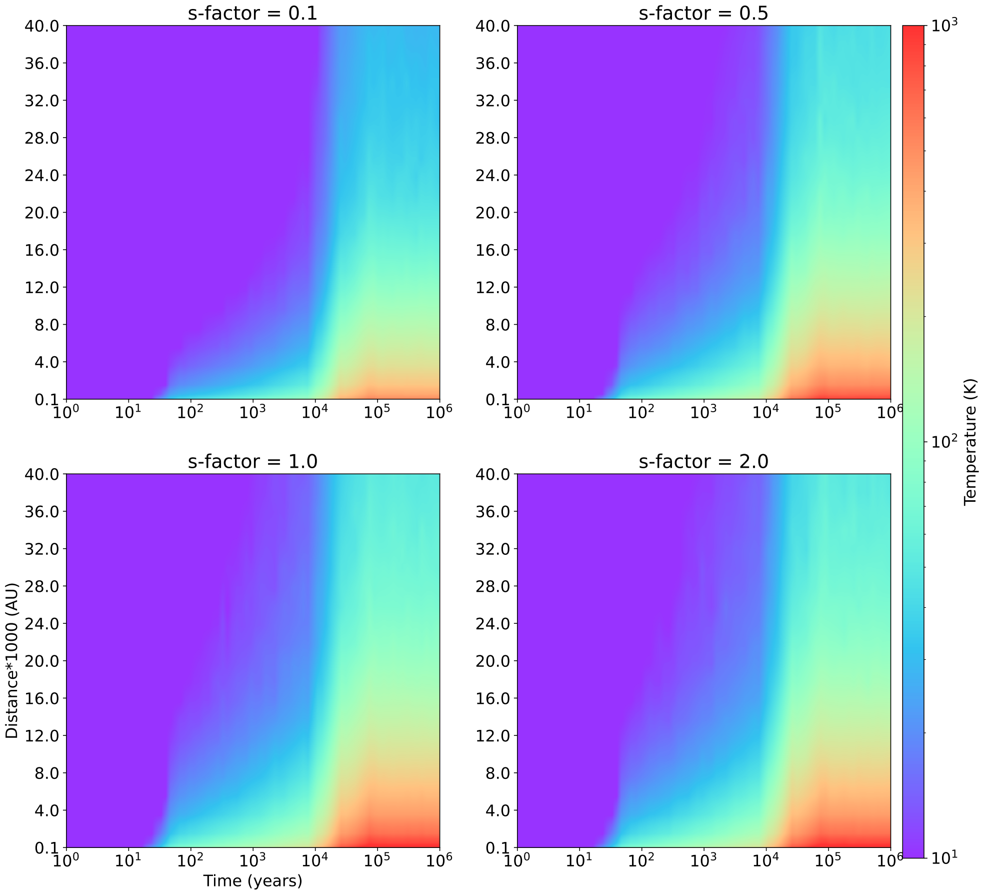

Figure 8.9: The thermal evolution of the cloud in different models (changing the s-factor in Hosokawa & Omukai models)

molecules

$$v = k[A][B] \tag{8.6}$$

which

- v is the reaction rate,
- k is the rate coefficient,

A and [B] are the abundance of reactant A and B
in the reaction A+B $\longrightarrow$ C+D

The reaction rate coefficient (k) strongly depends on the temperature (Arrhenius equation).

$$k = Ae^{-\frac{E_A}{RT}} \tag{8.7}$$

So when we change the temperature of the cloud, the reaction rate of formation and destruction are also changed.

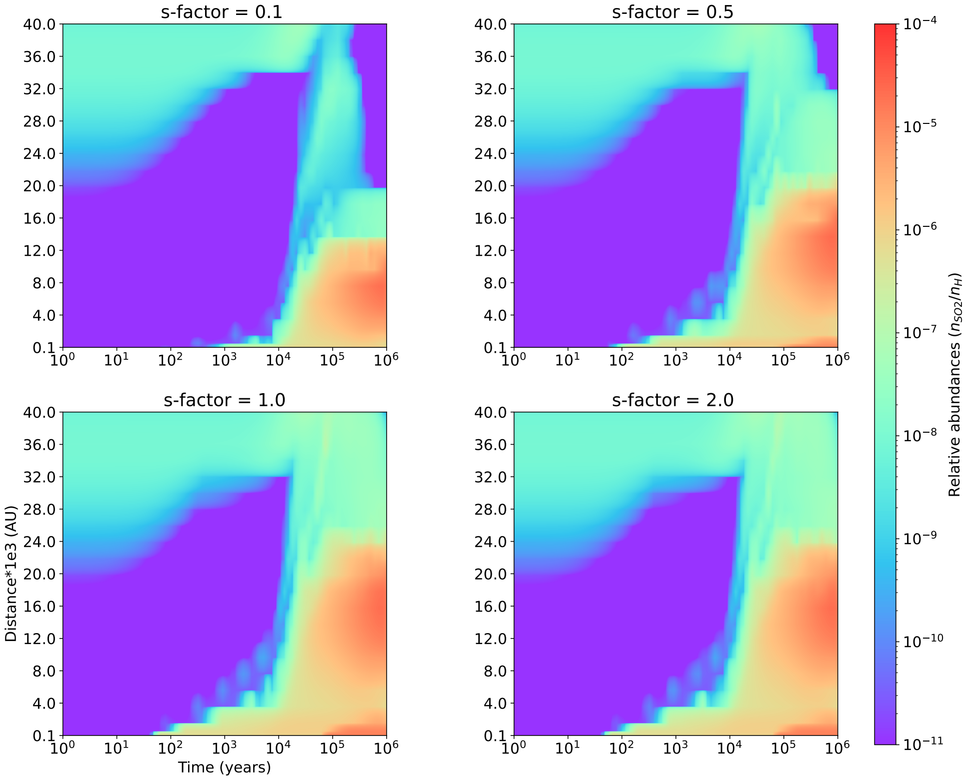

Figure 8.10: The relative abundances of SO_2 as a function of time (x-axis) and distance from the center of molecular cloud (y-axis) in different thermal evolution condition

When the temperature of the cloud increase, the molecules on the grain surface quickly evaporate to the gas phase, and the coefficient reaction rate also increases. There are numerous affected parameters, and we could not estimate and explain how the abundances change and why they change. We should use the total reaction of the molecules to understand which time step and region the molecular cloud is affected by changing the thermal evolution of the cloud.

We use the classification of the evolution of the molecular cloud into four regions 7.2 and physical properties of those regions in table 7.2. We also only focus on the late time step (R_3 and R_4 region). When we increase the s-factor from 0.1 to 1.0, the temperature of the cloud increase, but when we increase the s-factor from 1.0 to 2.0, the temperature of the cloud does not change. The unchanged cloud's temperature when we increase the s-factor from 1.0 to 2.0 is caused by the stabilization of the simulations. When we increase the total luminosity of the cloud, the effectiveness of temperature does not change. We will research more detail about the effect of total luminosity on the effectiveness of the temperature of the molecular cloud, but in this research, we only focus on the change of the thermal evolution of the cloud.

To simplify, we only analyze the evolution of SO_2 molecules in the different thermal evolution. The growth of other molecules and the total reaction of the molecules in different thermal evolution conditions are shown in the appendix (Influence of thermal evolution of the cloud).

Abundance profiles: In Fig. 8.10, we show the evolution of SO_2 molecules in the molecular cloud in different models by changing s-factor (0.1, 0.5, 1.0, 2.0) while keeping the exponent of Plummer-like function equal to 4.0, inner density equal 1.8×10^8 cm^{-3}, and the CRIR = 1.3×10^{-17} s^{-1}.

- The case s-factor = 0.1, 0.5, 1.0

  Comparing the changing of SO_2 molecule abundances in different thermal evolution models, we can see that in the range 10^4 to 10^6 years, the increasing of SO_2 molecules.

- The case s-factor = 1.0, 2.0

  In this case, when we increase the s-factor from 1.0 to 2.0, the abundances of SO_2 molecules do not change much. Because we are using the s-factor to change the thermal evolution of the cloud, the s-factor equal to 1.0 is almost the critical parameter. When we increase the s-factor, the temperature does not change much, leading to the result.

8.6 Influence of binding energy E_D of SO and OCS

The gas-grain chemistry is essential in the astrochemistry model, and recent laboratory measurements confirmed that chemical desorption could be an efficient process. However, the binding energies are probably the most uncertain in astrochemistry models. By changing the binding energy values, based on the research of Wakelam (Wakelam et al., 2017) we are changing the binding energy of SO and OCS molecules on the surface to see how does this parameter impacts chemical abundance in high mass stars forming regions.

Table 8.4: The parameters of the models which we use to compare the binding energy of OCS molecule

OCS binding energy (K)	s-factor	CRIR ζ(s^{-1})	Inner Density (cm^{-3})
2100	1.0	1.3×10^{-17}	1.8×10^8
2400	1.0	1.3×10^{-17}	1.8×10^8
2888	1.0	1.3×10^{-17}	1.8×10^8

Table 8.5: The parameters of the models which we use to compare the binding energy of SO molecule

SO binding energy (K)	s factor	CRIR ζ	Inner Density (cm^{-3})
1745	1.0	1.3×10^{-17}	1.8×10^8
2600	1.0	1.3×10^{-17}	1.8×10^8
2800	1.0	1.3×10^{-17}	1.8×10^8

The explanation of the influence of changing the binding energy of molecules can be based on the molecular cloud's temperature. The innermost of the molecular cloud in the later time step (R4) will not change because, in that region, the temperature is high, and molecules quickly evaporate into the gas phase. The binding energy of the molecules will not affect. The binding energy will affect the area where the temperature is around 100-200 K.

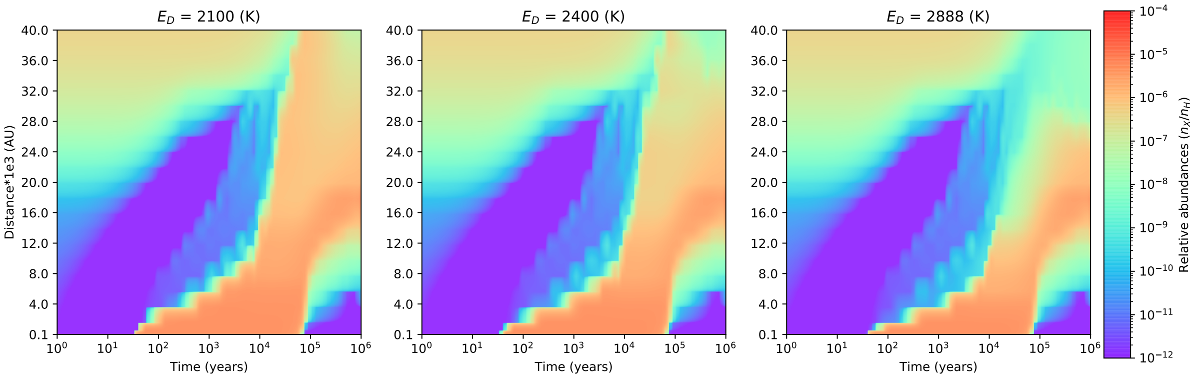

Figure 8.11: The relative abundances of OCS as a function of time (x-axis) and distance from the center of molecular cloud (y-axis) in different total luminosity conditions.

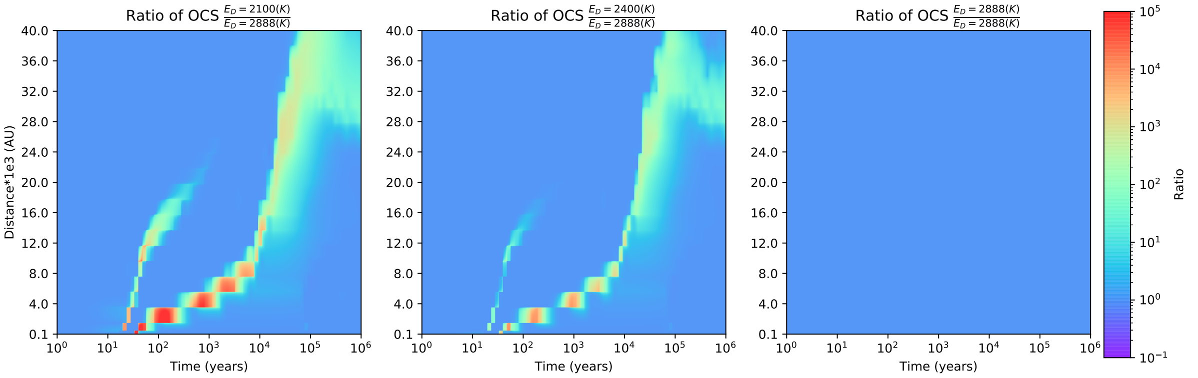

Figure 8.12: The ratio relative abundances of OCS as a function of time (x-axis) and distance from the center of molecular cloud (y-axis) in different total luminosity conditions.

In the Fig. 8.11 and Fig. 8.12. we found that the relative abundance of OCS changes when we decrease the binding energy from 2888 (K) to 2400 (K) and 2100 (K). The abundance change only happens around the region with a temperature around 100 (K). The change can be explained, and when we decrease binding energy, the molecule can evaporate easily into the gas phase. If the temperature is higher than 100 (K), the molecule can easily receive enough energy to evaporate into the gas phase.

In the Fig. 8.13 and Fig. 8.14. we found that the relative abundance of SO changes when we decrease the binding energy from 2800 (K) to 1745 (K). The abundance change also happens around the region with a temperature around 100 (K). The change can be explained, and when we decrease binding energy, the molecule can evaporate easily into the gas phase, but only where the temperature is reasonable. If the temperature is higher than 100 (K), the molecule can easily receive enough energy to evaporate into the gas phase.

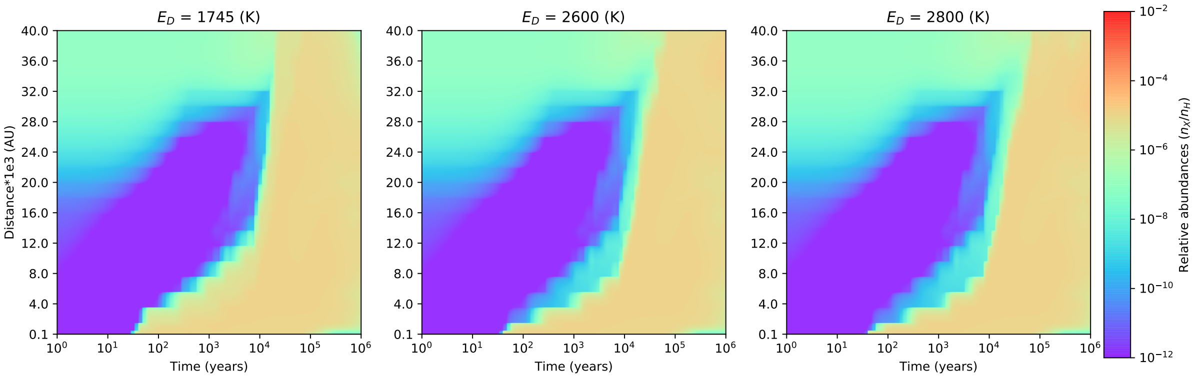

Figure 8.13: The relative abundances of SO as a function of time (x-axis) and distance from the center of molecular cloud (y-axis) in different total luminosity conditions.

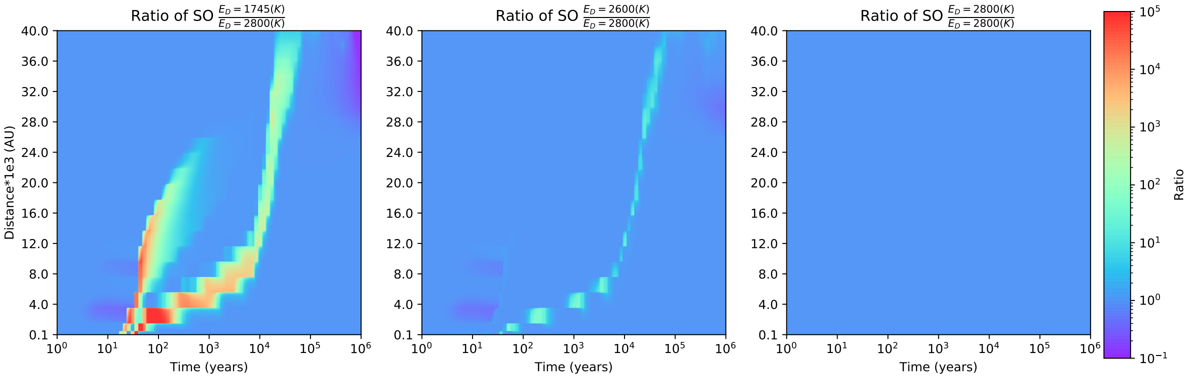

Figure 8.14: The ratio relative abundances of SO as a function of time (x-axis) and distance from the center of molecular cloud (y-axis) in different total luminosity conditions.

Chapter 9

Comparison of the observed and model results

The column density is the number of molecules in energy level u integrated over the lines of sight.(Mangum & Shirley, 2015)

$$N_u \equiv \int n_u ds \tag{9.1}$$

Deriving the column density of molecules is the first step to quantify the fundamental physical quantities such as spatial density and molecular abundance. The molecular column density is computed using molecular spectral line measurements, ultimately involving the measured radiative transfer properties. However, the column density of the molecules is not easily obtained from the observations and relies on various assumptions. We assume all molecule transitions are characterized by a single excitation temperature under the local thermodynamic equilibrium (LTE) approximation in a single source size.

On the other hand, the numerical simulations locally compute the molecular abundances based on chemical networks involving thousands of chemical reactions to investigate the chemical evolution and chemical relation of molecules in the ISM.

Moreover, chemical models are depended on the knowledge of the rate coefficients in the chemical network and their uncertainties for the gas-phase and grain surface processes. (Wakelam, Herbst, & Selsis, 2006) showed that the relative error on calculated abundances due to rate coefficient uncertainties might be more significant than 50% for hot cores aged $10^4 \rightarrow 10^6$ years (T = 100 K, $n_{\mathrm{H}_2} = 10^7\ \mathrm{cm}^{-3}$) and the lack of experimental and theoretical data for grain-surface processes.

Due to those circumstances, we also face some issues in observed data:

- Since the abundances of molecules in some regions are deficient and cannot be observable, we could not compute the column density of those molecules.
- The beam-averaged intensity of the source on the line of sight also impacts the observation results when comparing the observation and simulation in some regions where the simulation and observation consistently agree, but some areas do not.
- There are multiple uncertainties of the column density of molecules by using XCLASS fitting and the abundance of molecules in astrochemistry simulation.

9.1 Calculation of the ratio of S-bearing molecules

9.1.1 Computing the column density ratio of S-bearing molecules in observed results

We use the ratios of the column density of SO_2 and other sulfur-bearing molecules in the observed results to compare with the simulation results. Comparing the ratio of molecules can decrease the uncertainty of the observation and simulation results.

Firstly, we must determine every pixel's main velocity component to get the column density ratio. Then we compute the column density ratio by dividing the column density of SO_2 molecules at the main component with the column density of other molecules (such as OCS). Then we have the 2d map of the ratio column density of S-bearing molecules. Moreover, we have the temperature (SO_2 temperature) at the main component in each pixel. We can construct the plot of the column density ratio and temperature to see how the temperature affects the ratio.

9.1.2 Computing the abundances ratio of S-bearing molecules in astrochemical models

In the warm-up phase, we use 22 zones ($0.5 \times 10^3 \rightarrow 40 \times 10^3$ au) in 10^6 years. From the saptarsy results, we interpolate the grid of the saptarsy results into 1000×1000 points. Then we can compute the abundances ratio of S-bearing molecules from astrochemistry models by dividing the abundance of SO_2 molecules at each point with the abundance of other molecules (such as OCS). Then we have the 2d map of the ratio abundances of S-bearing molecules. Moreover, we have the temperature (SO_2 temperature) at each point, we can construct the plot of the abundance ratio and temperature.

9.2 Comparison observed and simulation results

By comparing the proportional distribution of S-bearing with the temperature of the cloud, we can evaluate the agreement of the observed results and the chemistry models.

For instance, we show the comparison of SO_2 and SO molecules in Fig 9.1. The blue dots are the abundance ratio of molecules depending on the temperature, and the red dots are the column density ratio of molecules depending on temperature. The red dots are computed from the observed results, so they do not change in all the conditions.

Based on the results in the astrochemical simulation results chapter, we found that cosmic rays influence the chemical properties of the molecular cloud. When we change the CRIR of the molecular cloud in the simulation, the abundances of S-bearing species change significantly. This section compares the simulation results in different CRIR conditions and the observed results.

We noticed that the Sgr B2 (Main) in the hot core is a complex structure, and the column density ratio of this region can vary along the line of sight. Because of the variation, we have to choose the main component (which we have discussed in the observed results chapter) to compare column density ratios with abundance ratios.

Moreover, in the cloud, there are many regions that the molecules would not be detectable because the contribution to the column density would be minimal. Still, in the abundance ratio plots, they could show up. Because of this reason, in the comparison plots, many simulation results do not agree with the observed results.

9.2.1 Comparison of the ratio of SO_2 and SO molecules

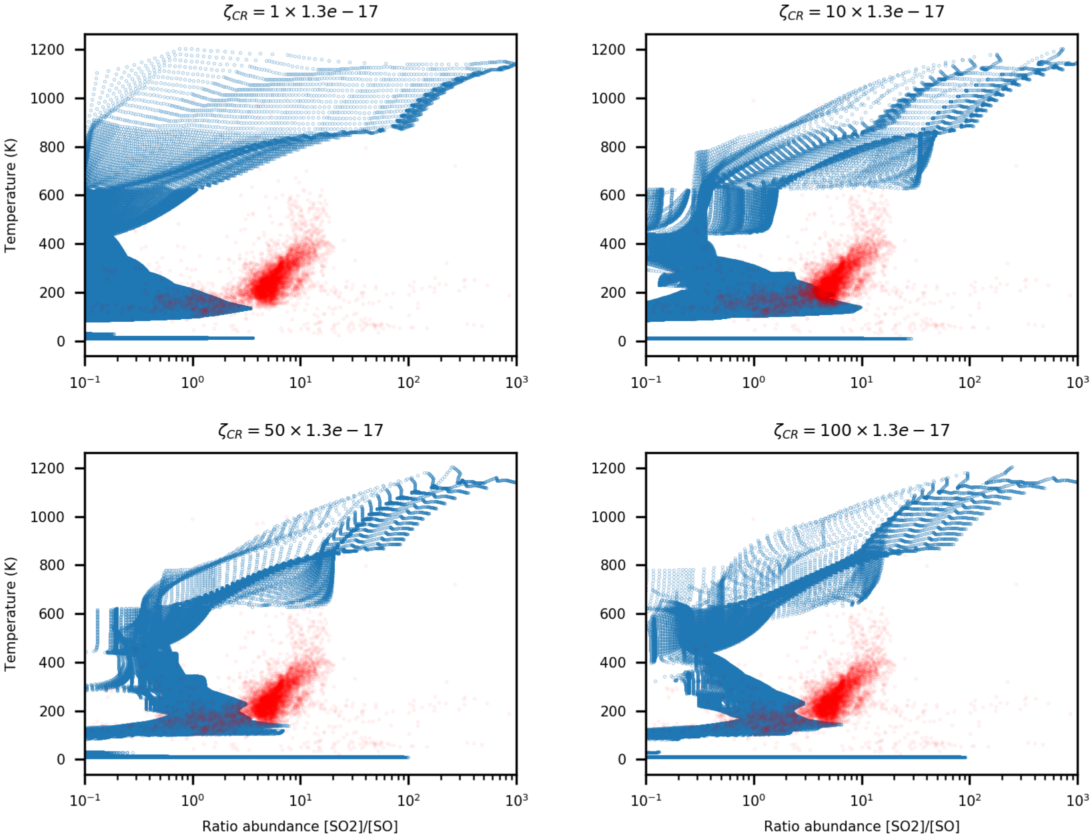

Figure 9.1: The comparison observed results (the column density ratio of SO_2/SO in red dots) and astrochemistry models (the abundance ratio of SO_2/SO in blue dots) in difference cosmic-ray ionization rate condition

Our observed results show that the ratio decreases when the temperature increases, consistent with the results of (Esplugues, Viti, Goicoechea, & Cernicharo, 2014). Figure 9.1 shows the abundance ratio of $[SO_2]/[SO]$ in observation and simulation results. The figure shows how consistent the results are by changing CRIR conditions. In the cases $\zeta_1 = 1.3 \times 10^{-17}\ s^{-1}, \zeta_3 = 50 \times \zeta_1$ and $\zeta_4 = 100 \times \zeta_1$, we can see that there is only some pixels which the temperature smaller the 200 (K) and the ratio column density in the range 0.5 to 5.0 are agree with the simulation results. Because the abundance of SO molecules in the simulation is mostly higher than the abundance of SO_2 molecules, the ratio abundances of SO_2 and SO are lower than 5 in the temperature range 50-600(K).

In the case $\zeta_2 = 10 \times \zeta_1$, we can see that most of the pixels with temperatures lower than around 230 (K) agree with simulation results. Those pixels with higher 230(K) do

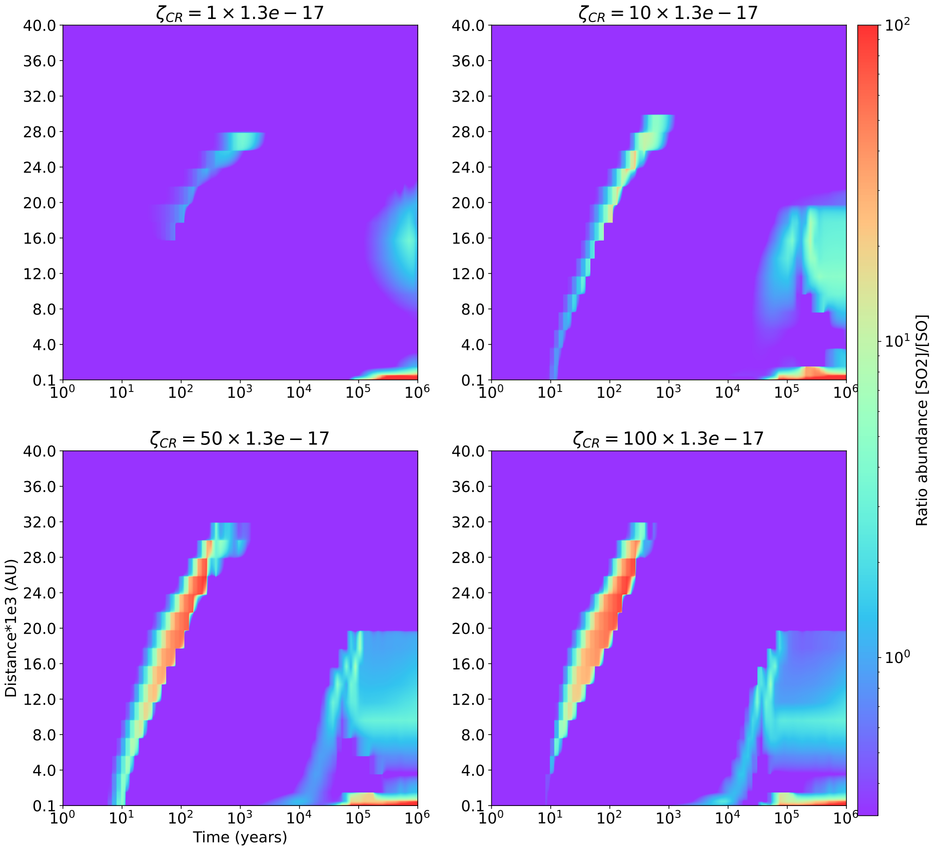

Figure 9.2: The abundances ratio of SO and SO_2 in difference cosmic-ray ionization rate condition

not agree with the simulation results because of the abundances ratio of $[SO_2]/[SO]<5$, or the abundance of SO_2 molecules lower than expected in the observed results. Most of the pixels with high temperatures (>230 K) are located in the hot core (the inner of the Sgr B2 (Main)). The cosmic ray cannot penetrate the inner region, the dissociation induced by cosmic ray could not happen in this region, or the effect of the cosmic ray could be decreased.

Figure 9.1 shows how the abundance ratio of $[SO_2]/[SO]$ changes in different cosmic rays conditions. The enhancement of CRIR leads to the ratio of $[SO_2]/[SO]$ enhancement. The difference is not easy to explain because when the CRIR enhance causes the increase in the H^+, H_3^+, He^+ ions, these ions impact the abundance of almost all molecules.

In addition, Figure 9.3 shows the spatial distribution of the ratio $[SO_2]/[SO]$ in Sgr B2 (M), which shows how the ratio change in the whole Sgr B2(M). We can see that, the ratio SO_2/SO cover the sgrb2m1, sgrb2m2, and the A region (defined in Fig. 6.7).

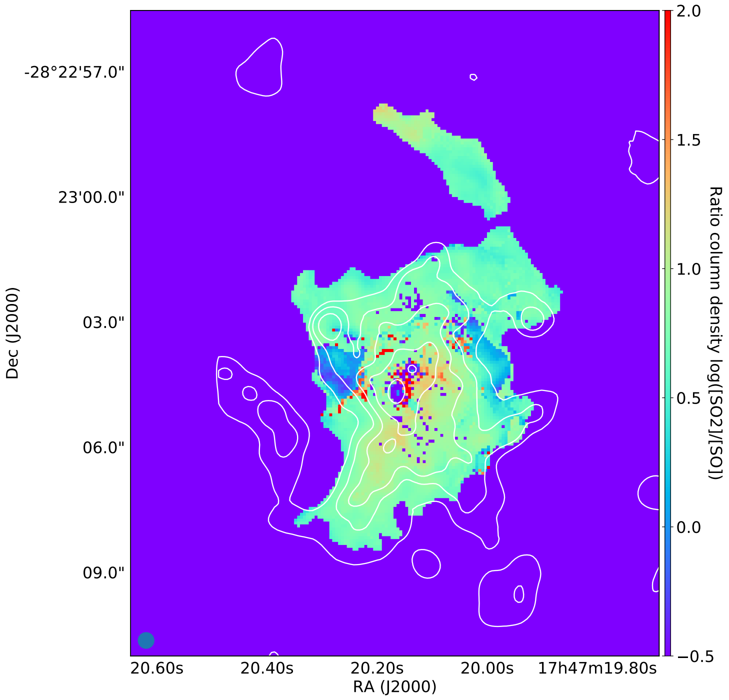

Figure 9.3: The spatial column density ratio of SO and SO_2 molecules in Sgr B2 (Main). The white contour shows the 1.3 mm continuum map of Sgr B2 (M)

9.2.2 Comparison of the ratio of SO_2 and OCS molecules

In the case of OCS, we compare the observed results and the astrochemical models, and we see that the observational result is consistent with the modeling results. The results are also consistent with the model prediction by (Wakelam, Hersant, & Herpin, 2011). The abundance ratio of SO_2/OCS in the simulation results increased when the temperature increases because the OCS molecules are destroyed by the chemical reactions such as

$$\mathrm{H} + \mathrm{OCS} \longrightarrow \mathrm{CO} + \mathrm{HS}$$

in such a temperature regime.

However, there are still so many simulation data points which are not cover the observational results. The difference can be explained that the models being the plots of ratio (x-axis) vs. temperature (y-axis) covered from 10^4 to 10^6 years and locate from 0.5×10^3 au to 40×10^3 au, and many data points cannot be observed. For instance, carbonyl sulfide (OCS) in the red rectangle regions A, B, C, D on the left hand side of Fig. 9.5, the abundance of OCS molecule is lower than the abundance of SO_2 molecule (ratio SO_2/OCS>100) in those regions, but the relative abundance of OCS molecules in those regions is too low ($N(OCS) < 10^{-9}$ cm^{-3}) and they are not observable.

Moreover, when we are comparing the simulation and observation (Fig. 9.4. Under the conditions CRIR $\zeta_1 = 1.3 \times 10^{-17}$ s^{-1} and $\zeta_2 = \zeta_1 \times 10$, the simulations cover the observed results, but under the conditions CRIR $\zeta_3 = 50 \times \zeta_1$ and $\zeta_4 = 100 \times \zeta_1$, the simulations do not cover all the observed results. We can conclude that the column density of OCS molecules which are derived by using XCLASS fit to the astrochemistry models under CRIR equal to ζ_1 and ζ_2, the density at the center equal to 1.8×10^8 cm^{-3}, the exponent of the Plummer-like function equal to 4.0, and the s-factor equal to 1.0.

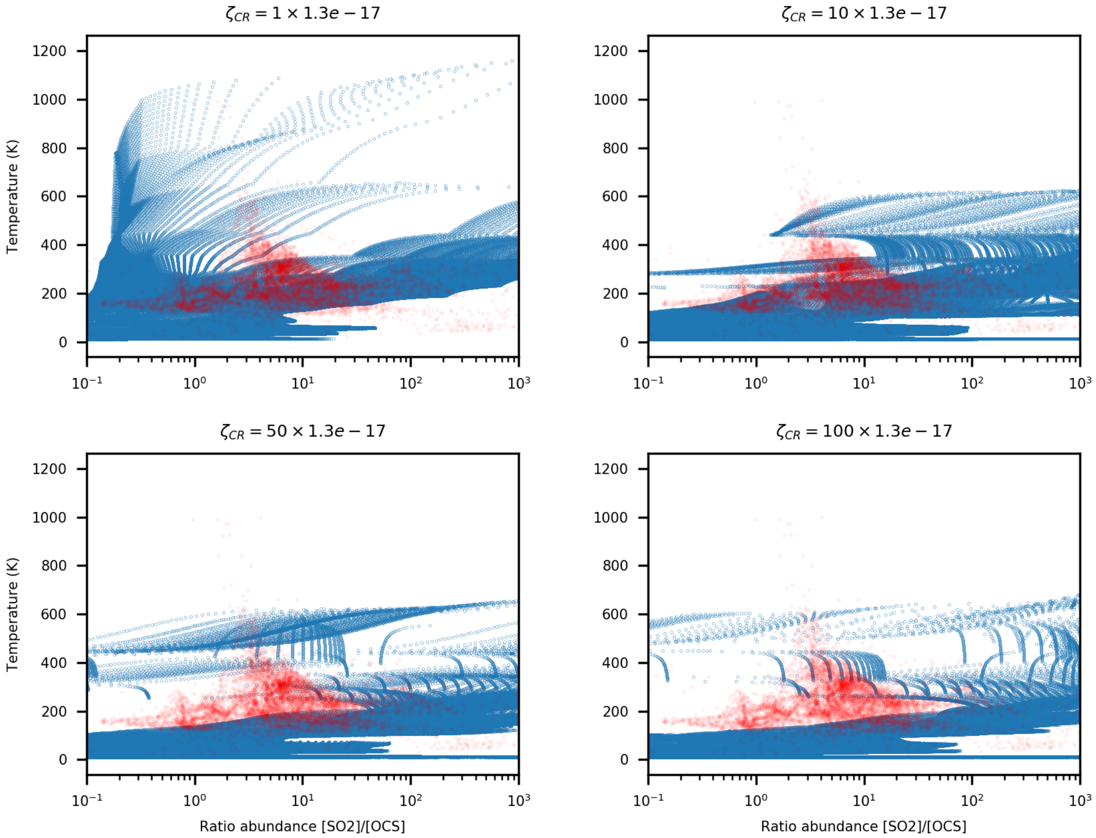

Figure 9.4: The comparison observed results (the column density ratio of SO_2/OCS in red dots) and astrochemistry models (the abundance ratio of SO_2/OCS blue dots) in difference cosmic-ray ionization rate condition

Figure 9.5 shows the changing of abundance ratio (left hand side) of [SO_2]/[OCS] under cosmic rays conditions, the enhancement of CRIR lead to the ratio of [SO_2]/[OCS] enhance. On the right hand side of the Fig. 9.5 shows the relative abundance of OCS under cosmic rays conditions. In addition, Figure 9.6 shows the spatial distribution of the ratio [SO_2]/[OCS] in Sgr B2 (M), which shows how the ratio change in the whole Sgr B2(M).

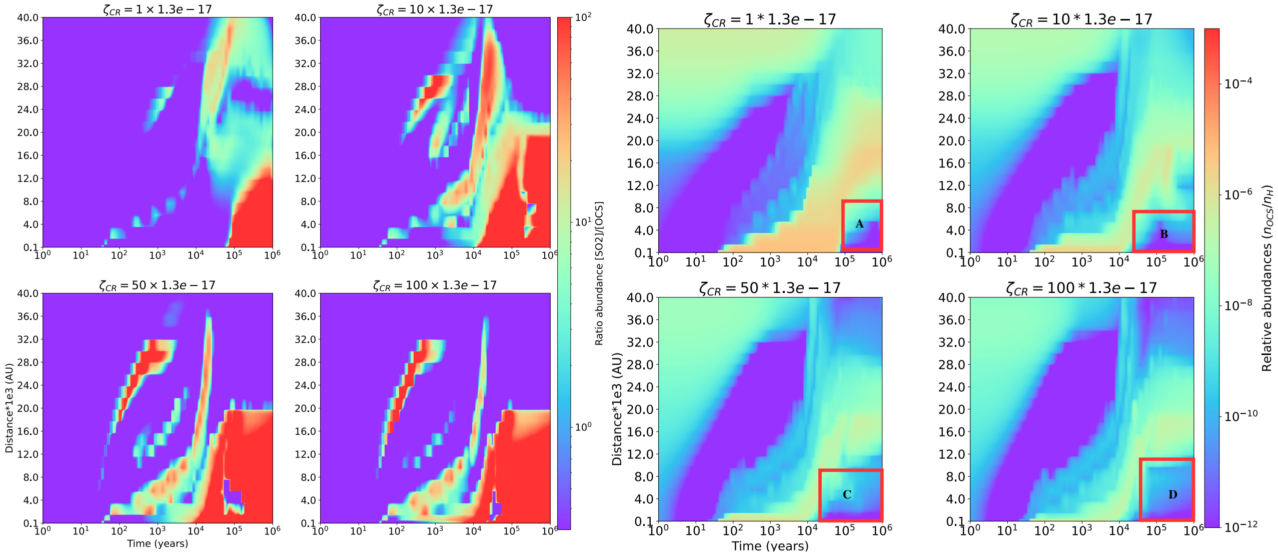

Figure 9.5: **Left panel:** The ratio abundances SO_2/OCS molecules in difference cosmic-ray ionization rate condition ; **Right panel:** The relative abundances of OCS as a function of time (x-axis) and distance from the center of molecular cloud (y-axis) in different cosmic rays conditions

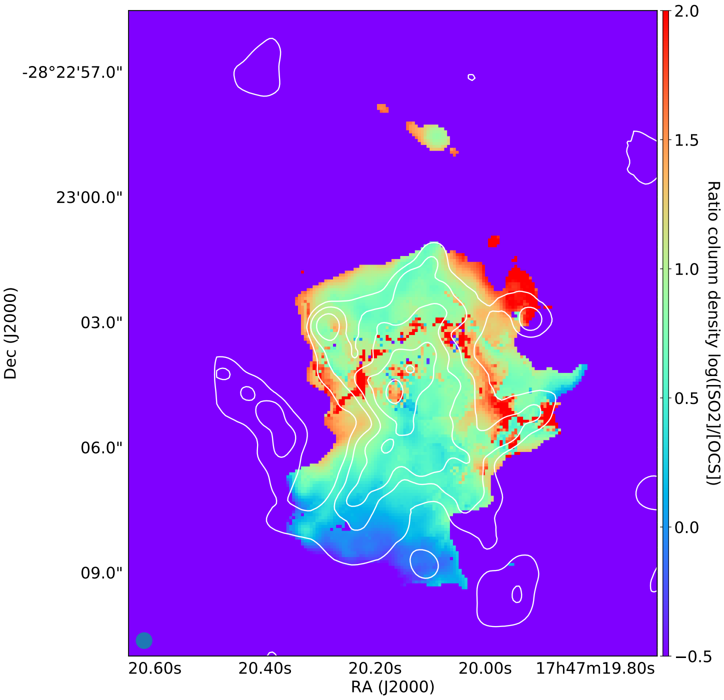

Figure 9.6: The spatial column density ratio of SO_2/OCS molecules in Sgr B2 (Main) including the 1.3 mm dust continuum in white contour observed by ALMA.

Chapter 10

Discussion

We compared the abundance ratio and column density ratio of SO_2/SO, and SO_2/OCS in observation and simulation results are relatively consistent under CRIR $= 10{\times}1.3.10^{-17}$ s^{-1} conditions. However, in the case of SO molecules, we found that some observation results still do not fit into the simulation results.

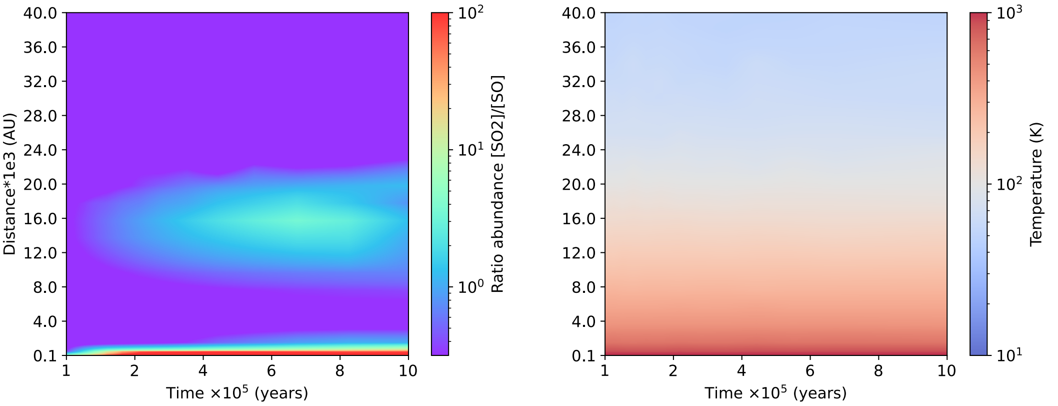

Figure 10.1: The ratio abundances of $[SO_2]/[SO]$ (on the left-hand side) and thermal evolution (on the right-hand side) as a function of time ($10^5 \rightarrow 10^6$ years) and distance from the center of molecular cloud (10^4 to 4.10^4 AU) in CRIR $= 10 \times 1.7 \times 10^{-17}$ s^{-1} condition

The discrepancy is significant in the hot core, where observationally, the SO_2/SO ratio is > 5, with both molecules having large column densities. The high ratio of SO_2/SO is not the case in the model.

We look at the simulation results and the comparison closer. Fig. 10.1 shows that in the late time step, the ratio abundance of $[SO_2]/[SO]$ is in the range 0.1-10, and the temperature of the region in the range 100-200 (K). The comparison in Fig. 10.2 shows clearer that the simulation and the observed results agree in the range temperature 100-230 (K). Nevertheless, in the higher temperature, the ratio abundance of $[SO_2]/[SO]$ is lower than in the ratio column density. We can conclude that outside of the hot core (T< 230 Kelvin), the observed data fit the simulation results, but in the hot where the high mass stars are formating, the abundances of SO_2 must be higher than our simulation results. The inconsistent simulation and observation in the hot core (T>230K) may be caused by some physical and chemical processes not included in the models.

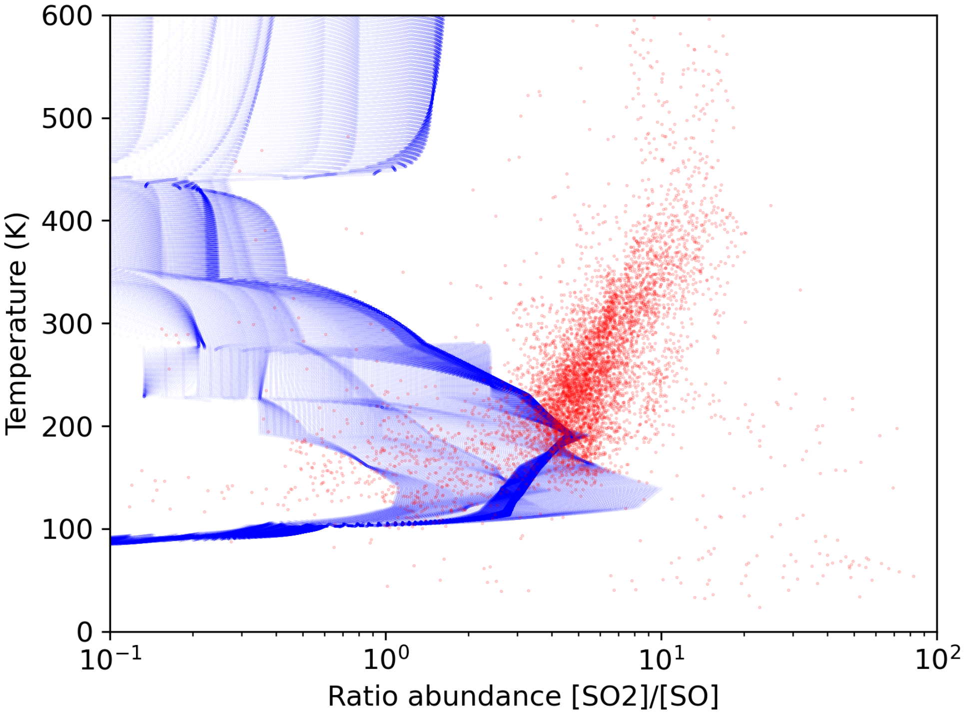

Figure 10.2: The comparison of the ratio abundances of $[SO_2]/[SO]$ (blue dot) and the ratio column density of $[SO_2]/[SO]$ (red dot) in the late time step ($10^5 \rightarrow 10^6$ years) in R3 and R4 region in CRIR $= 10 \times 1.7 \times 10^{-17}$ s^{-1} condition

We remind our chemical models to assume that CRIR is not attenuated in the envelope of the sources, which means the whole molecule cloud has the constant CRIR. Nevertheless, in reality, the cosmic ray can be attenuated by the H_2 molecules and dust particles. For instance, (Padovani, Hennebelle, & Galli, 2013) indicated the attenuation of the CRIR in the molecular cloud as a function of the density and (Rimmer, Herbst, Morata, & Roueff, 2012) suggested that a column-density-dependent CRIR improves the agreement between chemical model predictions and observations for the Horsehead nebula, compared to a standard model with a uniform CRIR.

Recently (Neufeld & Wolfire, 2017) suggested, based on H_2 and H_3^+ column densities measured toward diffuse clouds in the galactic disk, that the CRIR decreases with increasing H_2 column density and the cosmic-ray flux is attenuated by a factor $\sim 70-600$ from the diffuse regions with $N(H_2) = 10^{21}$ cm^{-2} to the dense gas with $N(H_2) = 10^{23} - 10^{24}$ cm^{-2}. And by the change by a factor $\sim 70 - 600$, the photodissociation induced by cosmic rays could be ignored in the high density region.

One possible consequence of this is that because of the attenuated cosmic ray flux, the destruction channel $SO_2 + CRP \longrightarrow SO + O$ is missing, and therefore the SO_2/SO ratio would increase. We, therefore, ran a model with a reduced the CRP flux by factor of 100 (CRIR $= 1.3 \times 10^{-19}$ s^{-1}), Fig. 10.3, and see that this is not the case. It seems likely that under this condition, the creation process of SO_2 is affected even more, since critical chemical process $H_2O + CRP \longrightarrow OH + H$, producing of OH molecules, is suppressed, and subsequently, the process $SO + OH \longrightarrow SO_2 + H$ is also suppressed, diminishing the production of SO_2 molecules.

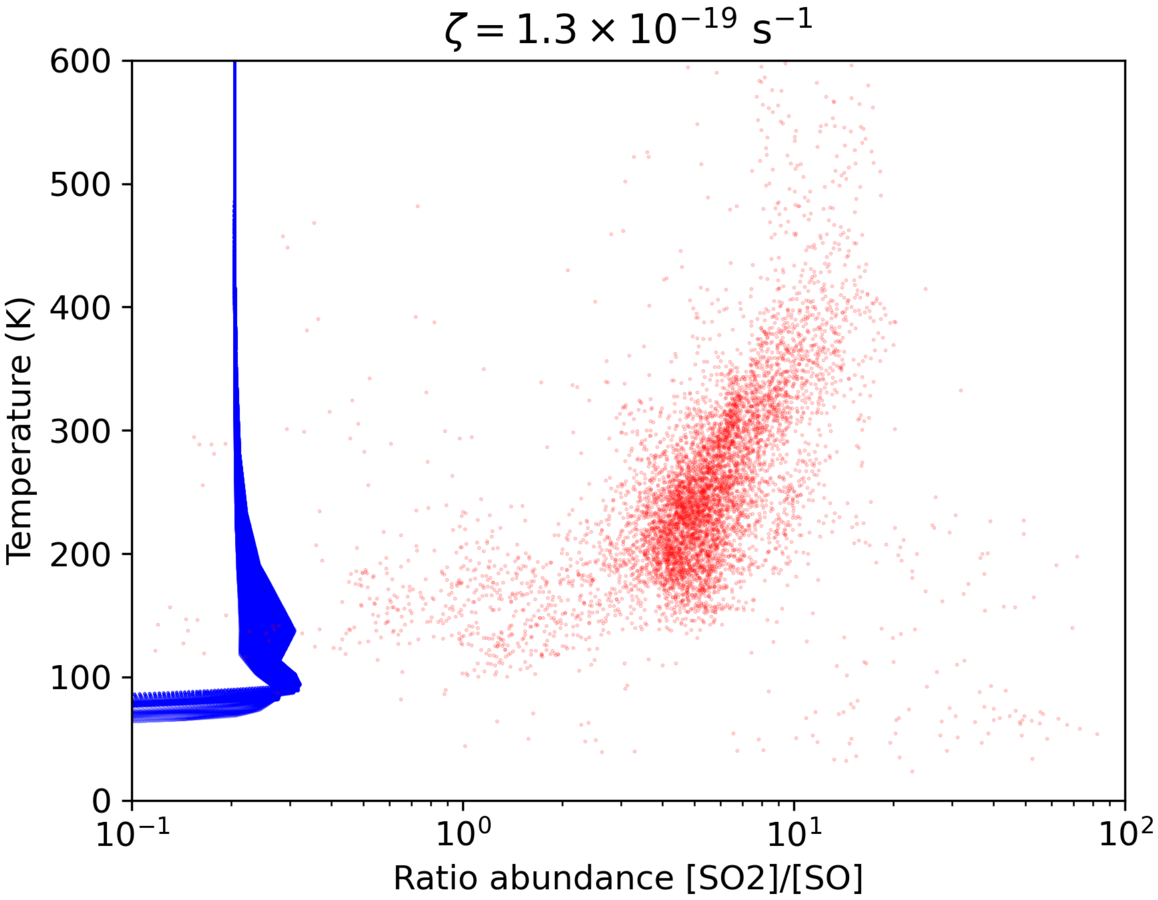

Figure 10.3: The comparison of the observational results (red dots) and astrochemistry models (blue dots) of SO_2 and SO molecules in the low CRIR condition (1.3×10^{-19} s^{-1})

Since the reduced cosmic ray flux does not seem to be responsible for the high SO_2/SO ratio, we must look for other explanations. A plausible candidate is shock chemistry, which is missing in our chemistry. In shocks, the gas temperature can be considerably higher than the dust temperature we calculated based on the luminosities, and therefore endothermic reactions with much higher barriers can happen. In the shock regions, the OH molecules are formed through the endothermic reaction $O + H_2 \longrightarrow OH + H$ ($\gamma = 4000K$ and $\gamma = 9650K$ (Baulch et al., 2005)) which react at high kinetic temperatures, which can be obtained in shock waves (Flower & Pineau Des Forêts, 2010). Because of the high abundances of OH molecules in the shock regions, the SO_2 molecules can be formed through the chemical equations (shown in Table 10.1)

Table 10.1: The formation equation of SO_2 molecule from OH molecules and S atoms

Reaction	α	β	γ
$S + OH \longrightarrow SO + H$	6.60×10^{-11}	0.00	0.00
$SO + OH \longrightarrow SO_2 + H$	8.6×10^{-11}	0.00	0.00

The increasing of SO_2 molecule abundance and decreasing the SO molecule abundance leads to the ratio abundance of [SO_2]/[SO] molecules in the hot core, which can be higher than the simulation results.

Moreover, the astrochemical models do not consider the effects of the PDRs (Photodissociation regions), leading to inconsistent simulation and observation comparisons. The Sgr B2 is a high-mass star-forming region, as we show in figure 6.1, the ionization components in SgB2 (Main), which could impact the abundances of molecules. In the PDRs, the UV photons are created, and that UV photon can destroy the molecules to form the smaller ion molecules, leading to the decreasing of the molecules' abundance.

Part V

Conclusion and Outlook

Chapter 11

Conclusion

This thesis studied Sgr B2 (M), a high-mass star-forming region with high temperature and density. SgrB2 is a giant molecular cloud located in the Central Molecular Zone close to the Galactic Center, and therefore, the cloud is affected by extreme conditions such as high levels of X-rays and cosmic rays radiation. Based on ALMA band 6 data, we analyze the abundances of S-bearing molecules, which can help us understand their structure and chemical abundances.

We found that the SgrB2(M) has a complex structure and line-rich chemistry, containing many species, especially sulfur-bearing molecules. Based on XCLASS, we can derive the temperature, column density, and velocity of the molecules in the cloud. Moreover, we can construct the spatial distribution map, which can help us understand more about the chemical properties of the cloud.

By analyzing the S-bearing molecules, we found one region which is not traced by continuum emission at millimeter wavelengths but has a high abundance in SO_2 molecule. The SgrB2(M) harbors multiple compact HII regions, and shocks related to the expansion of one of them (the A region defined in Fig. 6.7) might be found SO_2, SO, CS, and a small amount of OCS, the velocity of the part is around 20 km/s.

Moreover, we used the astrochemical model saptarsy to compare with the observed results and understand the chemical evolution of the cloud. By changing the cosmic rays ionization rate (CRIR), density distribution, thermal evolution, and binding energy of molecules, we found that CRIR is the important factor that completely regulates the chemistry of the cloud by producing basic ions such as H^+, ${H_3}^+$, ${H_2}^+$, He^+, C^+. These ions strongly impact the abundance of the molecule by forming and destroying them. Moreover, the secondary photodissociation induced by cosmic rays (UV-photons produced by cosmic rays) is also essential since these processes produce high-energy UV photons that can interact with molecules and break their bonds. For example, SO_2 can be destroyed via the process $SO_2 + CRP \longrightarrow SO + O$. Cosmic rays also affect the desorption of molecules from dust grain surfaces into the gas phase, impacting the chemistry and abundance of molecules.

From the comparison of observational results and astrochemistry models, we conclude that with CRIR equal to 10 times the standard value (1.3×10^{-17} s^{-1}), together with standard values for the density at the center equal 10^8 cm^{-3} and exponential in the Plummer-like function ($\eta = 4.0$), the astrochemical model results are comparable to the observational results. Despite this agreement, some aspects require further investigation in the future. For example, the SO_2/SO ratio seems to be anti-correlated concerning the model predictions. Nonetheless, this attenuation of the cosmic rays should be included in the models, and we should look in more detail at the impact of shock chemistry in S-bearing molecules, which is missing in our models.

Chapter 12

Outlook

This thesis mainly focused on the Sulfur-bearing molecules detected in Sgr B2(M). Another important outcome of the ALMA data survey in Sgr B2 (M) is detecting several interstellar COMs such as N-bearing (C_2H_5CN and CH_3CN) and O-bearing (CH_3OCHO and CH_3OCH_3) molecules. In particular, (Belloche et al., 2013) and (Möller et al., 2021) reported the detection of the interstellar COMs in Sgr B2 (M). Since our astrochemistry model includes 334 species, we can compare observations and models for a large number of molecules. In Fig 12.1 and Fig 12.2, we show the line-stacking maps of some molecules to see the distribution of those molecules in Sgr B2(M).

Furthermore, we can modify the models to understand the impact of the physical condition of the ISM on the chemistry and abundance of other COMs. Since the cosmic rays are the most critical factor, which impacts the chemistry of molecular clouds, we can analyze and compare the abundance of COMs in models to constrain the cosmic rays in Sgr B2 (M).

Moreover, to get around the problem of comparing (observational) column density ratios with (theoretical) abundance ratios, we can establish the connection between Saptarsy and XCLASS. XCLASS can model synthetic spectra from a set of components with individual column densities of molecules and gas temperatures in a three-dimensional space. We can compare them back to the observational results with the synthetic spectra. Further, the resulting synthetic spectra can be subjected to a principal component analysis (PCA) to analyze the molecules' behavior and the evolutionary tracks of the molecular cloud, depending on model and radial position. Those analyses enable the comparison of theoretical predictions with observations.

In addition, since there are no shock models in our simulation, we are planning to add shock models to see the effect of shock in the chemical evolution of molecules in the ISM. Finally, with our astrochemical code, we can model the physicochemical evolution and interpret the observational results of other high-mass star-forming regions in our Galaxy, for instance, the lower metallicity source such as giant molecular clouds (GMCs) in the Large Magellanic Cloud (LMC) and Small Magellanic Cloud (SMC).

In addition, we can use our code to analyze and compare with the observed results of the low-mass star forming region, and we can understand the difference between the high-mass star and low-mass star-forming regions.

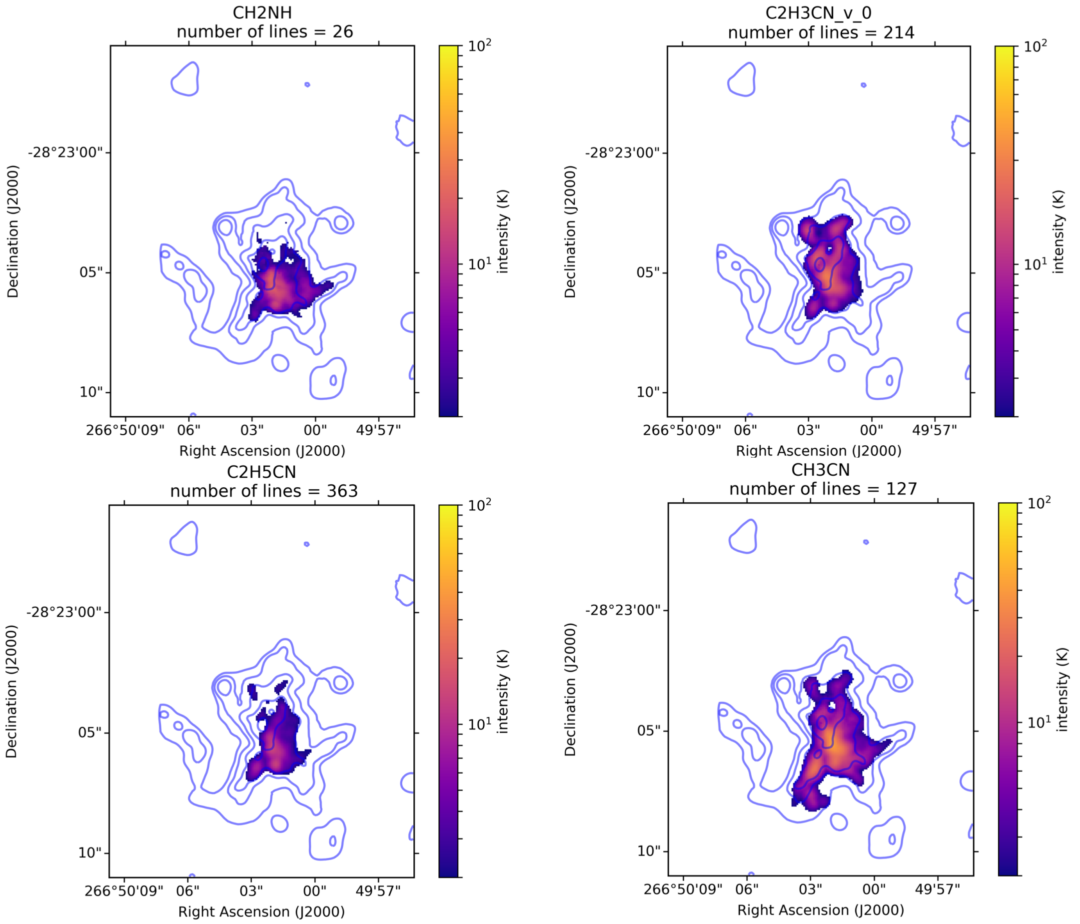

Figure 12.1: line stacking map of some N-bearing molecules in SgrB2(Main)

Moreover, our astrochemical code will allow us to investigate the influence of galactic location of the cloud (i.e., environment, with different CRIR values, density, temperature), stellar properties (mass, luminosity), and the impact of the physical properties on the chemical evolution in the molecular cloud.

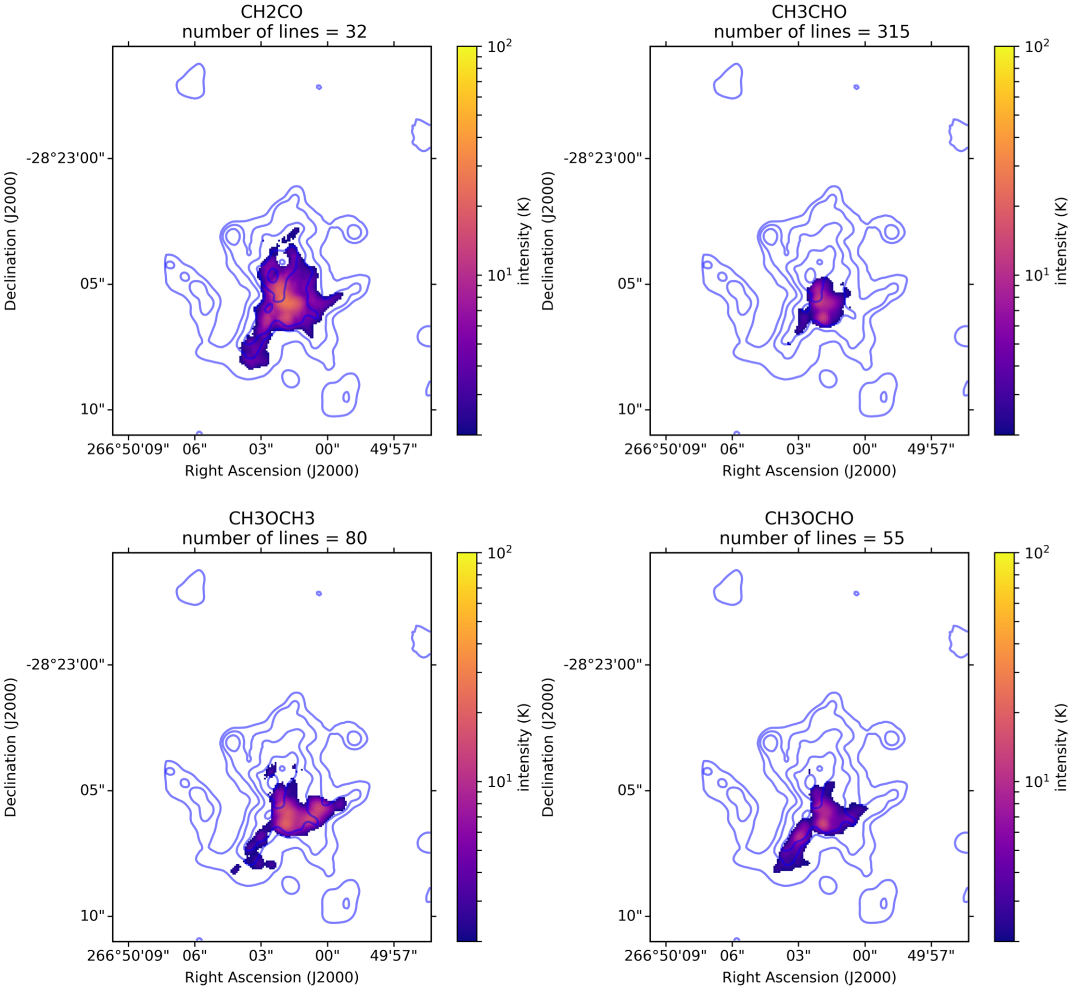

Figure 12.2: line stacking map of some O-bearing molecules in SgrB2(Main)

Bibliography

Ackermann, M., Ajello, M., Allafort, A., Baldini, L., Ballet, J., Barbiellini, G., ... others (2013). Detection of the characteristic pion-decay signature in supernova remnants. *Science*, *339*(6121), 807–811.

Barger, C. J., & Garrod, R. T. (2020). Constraining cosmic-ray ionization rates and chemical timescales in massive hot cores. *The Astrophysical Journal*, *888*(1), 38.

Baulch, D., Bowman, C., Cobos, C. J., Cox, R. A., Just, T., Kerr, J., ... others (2005). Evaluated kinetic data for combustion modeling: supplement ii. *Journal of physical and chemical reference data*, *34*(3), 757–1397.

Belloche, A., Müller, H. S., Menten, K. M., Schilke, P., & Comito, C. (2013). Complex organic molecules in the interstellar medium: Iram 30 m line survey of sagittarius b2 (n) and (m). *Astronomy & Astrophysics*, *559*, A47.

Benson, J., & Johnston, K. (1984). Arc second resolution maps of the compact sources in sagittarius b2 and g34. 3+ 0.2. *The Astrophysical Journal*, *277*, 181–188.

Blake, G. A., Sutton, E., Masson, C., & Phillips, T. (1987). Molecular abundances in omc-1: The chemical composition of interstellar molecular clouds and the influence of massive star formation. *Astrophysical Journal*, *315*(2), 621–645.

Bonfand, M. (2019). *Complex organic chemistry in high-mass star forming regions* (Unpublished doctoral dissertation). Max Planck Institute for Radio Astronomy, Max Planck Society.

Bonfand, M., Belloche, A., Garrod, R., Menten, K., Willis, E., Stéphan, G., & Müller, H. (2019). The complex chemistry of hot cores in sgr b2 (n): influence of cosmic-ray ionization and thermal history. *Astronomy & Astrophysics*, *628*, A27.

Bonfand, M., Belloche, A., Menten, K., Garrod, R., & Müller, H. (2017). Exploring molecular complexity with alma (emoca): Detection of three new hot cores in sagittarius b2 (n). *Astronomy & Astrophysics*, *604*, A60.

Bonnell, I., Bate, M., Clarke, C., & Pringle, J. (2001). Competitive accretion in embedded stellar clusters. *Monthly Notices of the Royal Astronomical Society*, *323*(4), 785–794.

Caswell, J., Fuller, G., Green, J., Avison, A., Breen, S., Brooks, K., ... others (2010). The 6-ghz methanol multibeam maser catalogue–i. galactic centre region, longitudes 345° to 6°. *Monthly Notices of the Royal Astronomical Society*, *404*(2), 1029–1060.

Charnley, S. (1997). Sulfuretted molecules in hot cores. *The Astrophysical Journal*, *481*(1), 396.

Choudhury, R., Schilke, P., Stéphan, G., Bergin, E., Möller, T., Schmiedeke, A., & Zernickel, A. (2015). Evolution of complex organic molecules in hot molecular cores-synthetic spectra at (sub-) mm wavebands. *Astronomy & Astrophysics*, *575*, A68.

Comito, C., Schilke, P., Rolffs, R., Lis, D., Belloche, A., Bergin, E., … others (2010). Herschel observations of deuterated water towards sgr b2 (m). *Astronomy & Astrophysics*, *521*, L38.

Dishoeck, E. F. v. (1988). Photodissociation and photoionization processes. In *Rate coefficients in astrochemistry* (pp. 49–72). Springer.

Draine, B. T. (1978). Photoelectric heating of interstellar gas. *The Astrophysical Journal Supplement Series*, *36*, 595–619.

Duley, W., & Williams, D. (1993). The formation of h2 on interstellar dust. *Monthly Notices of the Royal Astronomical Society*, *260*(1), 37–42.

Dullemond, C., Juhasz, A., Pohl, A., Sereshti, F., Shetty, R., Peters, T., … Flock, M. (2012). Radmc-3d: A multi-purpose radiative transfer tool. *Astrophysics Source Code Library*, ascl–1202.

Endres, C. P., Schlemmer, S., Schilke, P., Stutzki, J., & Müller, H. S. (2016). The cologne database for molecular spectroscopy, cdms, in the virtual atomic and molecular data centre, vamdc. *Journal of Molecular Spectroscopy*, *327*, 95–104.

Esplugues, G., Viti, S., Goicoechea, J., & Cernicharo, J. (2014). Modelling the sulphur chemistry evolution in orion kl. *Astronomy & Astrophysics*, *567*, A95.

Evans, N. J., Dunham, M. M., Jørgensen, J. K., Enoch, M. L., Merín, B., Van Dishoeck, E. F., … others (2009). The spitzer c2d legacy results: star-formation rates and efficiencies; evolution and lifetimes. *The Astrophysical Journal Supplement Series*, *181*(2), 321.

Flower, D., & Pineau Des Forêts, G. (2010). Excitation and emission of h2, co and h2o molecules in interstellar shock waves. *Monthly Notices of the Royal Astronomical Society*, *406*(3), 1745–1758.

Garrod, R. T., & Pauly, T. (2011). On the formation of co2 and other interstellar ices. *The Astrophysical Journal*, *735*(1), 15.

Garrod, R. T., Weaver, S. L. W., & Herbst, E. (2008). Complex chemistry in star-forming regions: An expanded gas-grain warm-up chemical model. *The Astrophysical Journal*, *682*(1), 283.

Gerner, T., Beuther, H., Semenov, D., Linz, H., Vasyunina, T., Bihr, S., … Henning, T. (2014). Chemical evolution in the early phases of massive star formation. i. *Astronomy & Astrophysics*, *563*, A97.

Goldsmith, P. F., & Langer, W. D. (1999). Population diagram analysis of molecular line emission. *The Astrophysical Journal*, *517*(1), 209.

Goldsmith, P. F., Lis, D. C., Hills, R., & Lasenby, J. (1990). High angular resolution submillimeter observations of sagittarius b2. *The Astrophysical Journal*, *350*, 186–194.

Hasegawa, T. I., & Herbst, E. (1993). New gas–grain chemical models of quiescent dense interstellar clouds: the effects of h2 tunnelling reactions and cosmic ray induced desorption. *Monthly Notices of the Royal Astronomical Society*, *261*(1), 83–102.

Hasegawa, T. I., Herbst, E., & Leung, C. M. (1992). Models of gas-grain chemistry in dense interstellar clouds with complex organic molecules. *The Astrophysical Journal Supplement Series*, *82*, 167–195.

Hosokawa, T., & Omukai, K. (2009). Evolution of massive protostars with high accretion rates. *The Astrophysical Journal*, *691*(1), 823.

Hüttemeister, S., Wilson, T., Mauersberger, R., Lemme, C., Dahmen, G., & Henkel, C. (1995). A multilevel study of ammonia in star-forming regions. vi: The envelope of sagittarius b2. *Astronomy and Astrophysics*, *294*, 667–676.

Indriolo, N., Neufeld, D. A., Gerin, M., Schilke, P., Benz, A. O., Winkel, B., … others (2015). Herschel survey of galactic oh+, h2o+, and h3o+: Probing the molecular hydrogen fraction and cosmic-ray ionization rate. *The Astrophysical Journal*, *800*(1), 40.

Kroupa, P. (2001). On the variation of the initial mass function. *Monthly Notices of the Royal Astronomical Society*, *322*(2), 231–246.

Le Bourlot, J., Le Petit, F., Pinto, C., Roueff, E., & Roy, F. (2012). Surface chemistry in the interstellar medium-i. h2 formation by langmuir-hinshelwood and eley-rideal mechanisms. *Astronomy & Astrophysics*, *541*, A76.

Le Petit, F., Nehmé, C., Le Bourlot, J., & Roueff, E. (2006). A model for atomic and molecular interstellar gas: The meudon pdr code. *The Astrophysical Journal Supplement Series*, *164*(2), 506.

Mangum, J. G., & Shirley, Y. L. (2015). How to calculate molecular column density. *Publications of the Astronomical Society of the Pacific*, *127*(949), 266.

Marquardt, D. W. (1963). An algorithm for least-squares estimation of nonlinear parameters. *Journal of the society for Industrial and Applied Mathematics*, *11*(2), 431–441.

Martin, A., & Downes, D. (1972). Possible sites of star formation in sgr b2. *Astrophysical Letters*, *11*, 219.

Martín-Pintado, J., Gaume, R., Rodríguez-Fernández, N., De Vicente, P., & Wilson, T. (1999). Hot expanding shells in the envelope of the sagittarius b2 molecular cloud. *The Astrophysical Journal*, *519*(2), 667.

McGrath, E. J., Goss, W., & De Pree, C. G. (2004). H2o masers in w49 north and sagittarius b2. *The Astrophysical Journal Supplement Series*, *155*(2), 577.

McKee, C. F., & Tan, J. C. (2003). The formation of massive stars from turbulent cores. *The Astrophysical Journal*, *585*(2), 850.

Mehringer, D. M., Palmer, P., Goss, W., & Yusef-Zadeh, F. (1993). Radio continuum and radio recombination line observations of sagittarius b2. *The Astrophysical Journal*, *412*, 684–695.

Meng, F., Sánchez-Monge, Á., Schilke, P., Padovani, M., Marcowith, A., Ginsburg, A., … others (2019). The physical and chemical structure of sagittarius b2-v. non-thermal emission in the envelope of sgr b2. *Astronomy & Astrophysics*, *630*, A73.

Möller, T., Endres, C., & Schilke, P. (2017). extended casa line analysis software suite (xclass). *Astronomy & Astrophysics*, *598*, A7.

Möller, T., Schilke, P., Schmiedeke, A., Bergin, E., Lis, D., Sánchez-Monge, Á., … Comito, C. (2021). Herschel observations of extraordinary sources: Full herschel/hifi molecular line survey of sagittarius b2 (m). *arXiv preprint arXiv:2104.13150*.

Müller, H. S., Schlöder, F., Stutzki, J., & Winnewisser, G. (2005). The cologne database for molecular spectroscopy, cdms: a useful tool for astronomers and spectroscopists. *Journal of Molecular Structure*, *742*(1-3), 215–227.

Müller, H. S., Thorwirth, S., Roth, D., & Winnewisser, G. (2001). The cologne database for molecular spectroscopy, cdms. *Astronomy & Astrophysics*, *370*(3), L49–L52.

Neill, J. L., Bergin, E. A., Lis, D. C., Schilke, P., Crockett, N. R., Favre, C., … others (2014). Herschel observations of extraordinary sources: analysis of the full herschel/hifi molecular line survey of sagittarius b2 (n). *The Astrophysical Journal*, *789*(1), 8.

Neufeld, D. A., & Wolfire, M. G. (2017). The cosmic-ray ionization rate in the galactic disk, as determined from observations of molecular ions. *The Astrophysical Journal*, *845*(2), 163.

Öberg, K. I., Boogert, A. A., Pontoppidan, K. M., Van den Broek, S., Van Dishoeck, E. F., Bottinelli, S., … Evans II, N. J. (2011). The spitzer ice legacy: Ice evolution from cores to protostars. *The Astrophysical Journal*, *740*(2), 109.

Padovani, M., Hennebelle, P., & Galli, D. (2013). Cosmic-ray ionisation in collapsing clouds. *Astronomy & Astrophysics*, *560*, A114.

Padovani, M., Marcowith, A., Hennebelle, P., & Ferrière, K. (2016). Protostars: Forges of cosmic rays? *Astronomy & Astrophysics*, *590*, A8.

Pickett, H., Poynter, R., Cohen, E., Delitsky, M., Pearson, J., & Müller, H. (1998). Submillimeter, millimeter, and microwave spectral line catalog. *Journal of Quantitative Spectroscopy and Radiative Transfer*, *60*(5), 883–890.

Pineau des Forêts, G., Roueff, E., Schilke, P., & Flower, D. R. (1993). Sulphur-bearing molecules as tracers of shocks in interstellar clouds. *Monthly Notices of the Royal Astronomical Society*, *262*(4), 915–928.

Pols, S., Schwörer, A., Schilke, P., Schmiedeke, A., Sánchez-Monge, Á., & Möller, T. (2018). The physical and chemical structure of sagittarius b2-iii. radiative transfer simulations of the hot core sgr b2 (m) for methyl cyanide. *Astronomy & Astrophysics*, *614*, A123.

Prasad, S. S., & Tarafdar, S. P. (1983). Uv radiation field inside dense clouds-its possible existence and chemical implications. *The Astrophysical Journal*, *267*, 603–609.

Qin, S.-L., Schilke, P., Rolffs, R., Comito, C., Lis, D., & Zhang, Q. (2011a). Submillimeter continuum observations of sagittarius b2 at subarcsecond spatial resolution. *Astronomy & Astrophysics*, *530*, L9.

Qin, S.-L., Schilke, P., Rolffs, R., Comito, C., Lis, D., & Zhang, Q. (2011b). Submillimeter continuum observations of sagittarius b2 at subarcsecond spatial resolution. *Astronomy & Astrophysics*, *530*, L9.

Ragan, S. E., Bergin, E. A., Plume, R., Gibson, D. L., Wilner, D. J., O'Brien, S., & Hails, E. (2006). Molecular line observations of infrared dark clouds: seeking the precursors to intermediate and massive star formation. *The Astrophysical Journal Supplement Series*, *166*(2), 567.

Reid, M., Menten, K., Brunthaler, A., Zheng, X., Dame, T., Xu, Y., … others (2014). Trigonometric parallaxes of high mass star forming regions: the structure and kinematics of the milky way. *The Astrophysical Journal*, *783*(2), 130.

Rimmer, P., Herbst, E., Morata, O., & Roueff, E. (2012). Observing a column-dependent ζ in dense interstellar sources: the case of the horsehead nebula. *Astronomy & Astrophysics*, *537*, A7.

Rolffs, R., Schilke, P., Comito, C., Bergin, E., Van Der Tak, F., Lis, D., … others (2010). Reversal of infall in sgrb2 (m) revealed by herschel/hifi observations of hcn lines at thz frequencies. *Astronomy & Astrophysics*, *521*, L46.

Sánchez-Monge, Á., Schilke, P., Schmiedeke, A., Ginsburg, A., Cesaroni, R., Lis, D., … others (2017). The physical and chemical structure of sagittarius b2-ii. continuum millimeter emission of sgr b2 (m) and sgr b2 (n) with alma. *Astronomy & Astrophysics*, *604*, A6.

Schaefer, D. (2017). Modeling icy dust mantles: A multi-phase model for gas-grain chemistry in the rate equation approach.

Schmiedeke, A., Schilke, P., Möller, T., Sánchez-Monge, Á., Bergin, E., Comito, C., … others (2016). The physical and chemical structure of sagittarius b2-i. three-dimensional thermal dust and free-free continuum modeling on 100 au to 45 pc scales. *Astronomy & Astrophysics*, *588*, A143.

Schwörer, A., Sánchez-Monge, Á., Schilke, P., Möller, T., Ginsburg, A., Meng, F., … Qin, S.-L. (2019). The physical and chemical structure of sagittarius b2-iv. converging filaments in the high-mass cluster forming region sgr b2 (n). *Astronomy & Astrophysics*, *628*, A6.

Semenov, D., Hersant, F., Wakelam, V., Dutrey, A., Chapillon, E., Henning, T., … others (2010). Chemistry in disks-iv. benchmarking gas-grain chemical models with surface reactions. *Astronomy & Astrophysics*, *522*, A42.

Shen, C., Greenberg, J., Schutte, W., & Van Dishoeck, E. (2004). Cosmic ray induced explosive chemical desorption in dense clouds. *Astronomy & Astrophysics*, *415*(1), 203–215.

Spitzer Jr, L., & Arny, T. T. (1978). *Physical processes in the interstellar medium.* American Association of Physics Teachers.

Stéphan, G., Schilke, P., Le Bourlot, J., Schmiedeke, A., Choudhury, R., Godard, B., & Sánchez-Monge, Á. (2018). Chemical modeling of internal photon-dominated regions surrounding deeply embedded hc/uchii regions. *Astronomy & Astrophysics*, *617*, A60.

Taquet, V., Ceccarelli, C., & Kahane, C. (2012). Multilayer modeling of porous grain surface chemistry-i. the grainoble model. *Astronomy & Astrophysics*, *538*, A42.

Vallance, C. (2017). *Astrochemistry: From the big bang to the present day.* World Scientific Publishing Company.

Vasyunin, A., & Herbst, E. (2013). Reactive desorption and radiative association as possible drivers of complex molecule formation in the cold interstellar medium. *The Astrophysical Journal*, *769*(1), 34.

Vasyunina, T., Linz, H., Henning, T., Zinchenko, I., Beuther, H., & Voronkov, M. (2011). Chemistry in infrared dark clouds. *Astronomy & Astrophysics*, *527*, A88.

Wakelam, V., & Herbst, E. (2008). Polycyclic aromatic hydrocarbons in dense cloud chemistry. *The Astrophysical Journal*, *680*(1), 371.

Wakelam, V., Herbst, E., & Selsis, F. (2006). The effect of uncertainties on chemical models of dark clouds. *Astronomy & Astrophysics*, *451*(2), 551–562.

Wakelam, V., Hersant, F., & Herpin, F. (2011). Sulfur chemistry: 1d modeling in massive dense cores. *Astronomy & Astrophysics*, *529*, A112.

Wakelam, V., Loison, J.-C., Mereau, R., & Ruaud, M. (2017). Binding energies: New values and impact on the efficiency of chemical desorption. *Molecular Astrophysics*, *6*, 22–35.

Williams, D. A., Hartquist, T. W., Rawlings, J. M., Cecchi-Pestellini, C., & Viti, S. (2017). *Dynamical astrochemistry.* Royal Society of Chemistry.

Xue, C., Remijan, A. J., Burkhardt, A. M., & Herbst, E. (2019). Alma observations of the spatial distribution of three c2h4o2 isomers toward sgr b2 (n). *The Astrophysical Journal*, *871*(1), 112.

Yamamoto, S. (2017). Introduction to astrochemistry. *Editorial: Springer*.

Acknowledgement

The thesis was completed with valuable guidance and advice from my supervisor and my friends. Please accept from me my sincere thanks and deep gratitude:

First of all, I would like to thank Prof. Dr. Peter Schilke, who allowed me to work on such an exciting topic. Moreover, he enthusiastically guided and always gave me valuable comments during the research period to complete the thesis.

Special thanks to my friends in the PS group for always creating good conditions for me during my research.

Sincere thanks to the enthusiastic help of Dr. Álvaro Sánchez-Monge, Dr. Thomas Möller, who always helped me and gave me helpful advice and comments during the thesis work.

Special appreciation to Dr. Luong-Quang Nguyen: for giving me the motivation for my research and helping me find a Ph.D. position at the University of Cologne.

Xin chân thành cảm ơn Bộ Giáo dục và Đào tạo Việt Nam - Cục Hợp Tác Quốc tế đã tạo điều kiện, kinh phí, hỗ trợ tốt nhất để tôi hoàn thành luận văn. Ngoài ra, em xin cảm ơn chị Trần Thị Nga, Cục Hợp Tác Quốc tế đã cung cấp thông tin chính xác, kịp thời cũng như giúp em giải quyết các vướng mắc về thủ tục giấy tờ trong quá trình thực hiện luận văn tại Đại Học Cologne.

Erklärung

„Hiermit versichere ich an Eides statt, dass ich die vorgelegte Dissertation selbstständig und ohne die Benutzung anderer als der angegebenen Hilfsmittel und Literatur angefertigt habe. Alle Stellen, die wörtlich oder sinngemäß aus veröffentlichten und nicht veröffentlichten Werken dem Wortlaut oder dem Sinn nach entnommen wurden, sind als solche bekanntlich gemacht. Ich versichere an Eides statt, dass diese Dissertation noch keiner anderen Fakultät oder Universität zur Prüfung vorgelegen hat; dass sie - abgesehen von unten angegebenen Teilpublikationen und eingebundenen Artikeln und Manuskripten - noch nicht veröffentlicht worden ist sowie, dass ich eine Veröffentlichung der Dissertation vor Abschluss der Promotion nicht ohne Genehmigung des Promotionsausschusses geltend machen würde. Die Bestimmungen dieser Ordnung sind mir bekannt. Darüber hinaus erkläre ich hiermit, dass ich die Ordnung zur Sicherung guter wissenschaftlicher Praxis und zum Umgang mit wissenschaftlichem Fehlverhalten der Universität zu Köln gelesen und sie bei der Durchführung der Dissertation zugrundeliegenden Arbeiten und der schriftlich verfassten Dissertation berücksichtigt habe und verpflichte mich hiermit, die dort genannten Vorgaben bei allen wissenschaftlichen Tätigkeiten zu beachten und umzusetzen. Ich versichere, dass die eingereichte elektronische Fassung der eingereichten Druckfassung vollständig entspricht."

Teilpublikationen:

Köln, 02.04.2022: ____________________

Thanh Liem Ngo

Appendices

Appendix A

Astrochemistry models

A.1 The impact of cosmic rays in S-bearing molecules

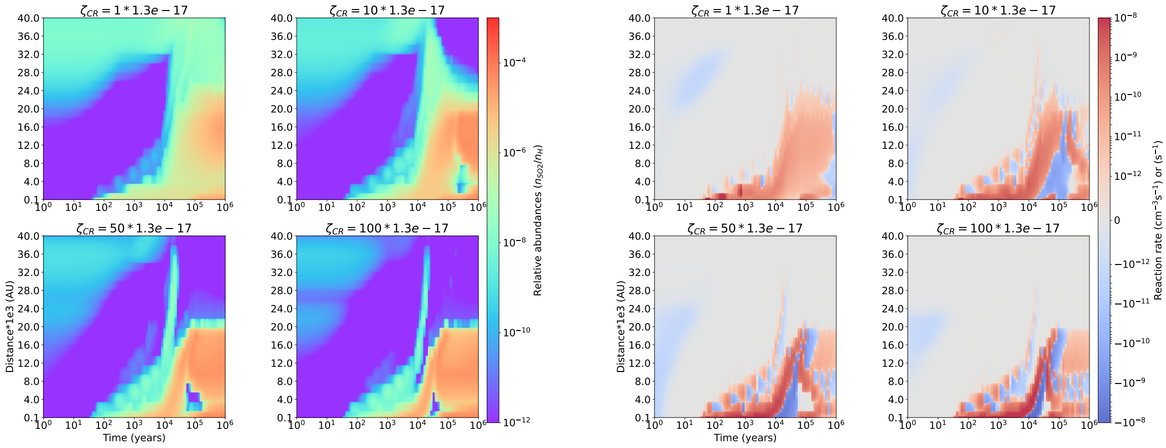

(a) (b)

Figure A.1: The relative abundances of SO_2 and total reaction rate of SO_2 as a function of time (x-axis) and distance from the center of molecular cloud (y-axis) with different cosmic rays conditions : **a. relative abundances n_{SO_2}/n_H , b. Total reaction rate of SO_2**

In the fig A.1, on the left-hand side, we notice that the relative abundance of SO_2 molecules are decreased when we enhance the CRIR. On the right-hand side, we can see the destruction rate of SO_2 is increased.

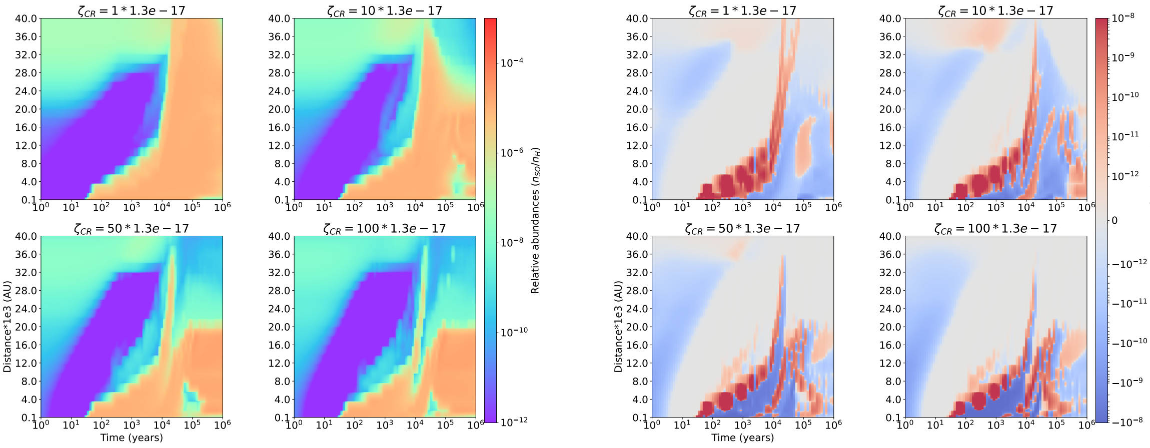

(a) (b)

Figure A.2: The relative abundances of SO and total reaction rate of SO as a function of time (x-axis) and distance from the center of molecular cloud (y-axis) with different cosmic rays conditions : **a. relative abundances $n_{\mathbf{SO}}/n_{\mathbf{H}}$** , **b. Total reaction rate of SO**

In the fig A.2, on the left-hand side, we notice that the relative abundance of SO molecules are decreased when we enhance the CRIR, SO molecule exists in R3 and R4 region, and it is decreasing and only exist in R4 when CRIR = ζ_{100}. On the right-hand side, we can see the destruction rate of SO is increased, the molecule is forming at around $10^2 \rightarrow 10^4$ years, and then it is destroyed after 10^4 years

In the fig A.3, on the left-hand side, we notice that the relative abundance of OCS molecules are decreased when we enhance the CRIR, OCS molecule exist in R3 and R4 region, and it is reducing its abundance when CRIR = ζ_{100}. On the right-hand side, we can see the destruction rate of OCS is increased, the molecule is forming at around $10^2 \rightarrow 10^4$ years, and then it is destroyed after 10^4 years

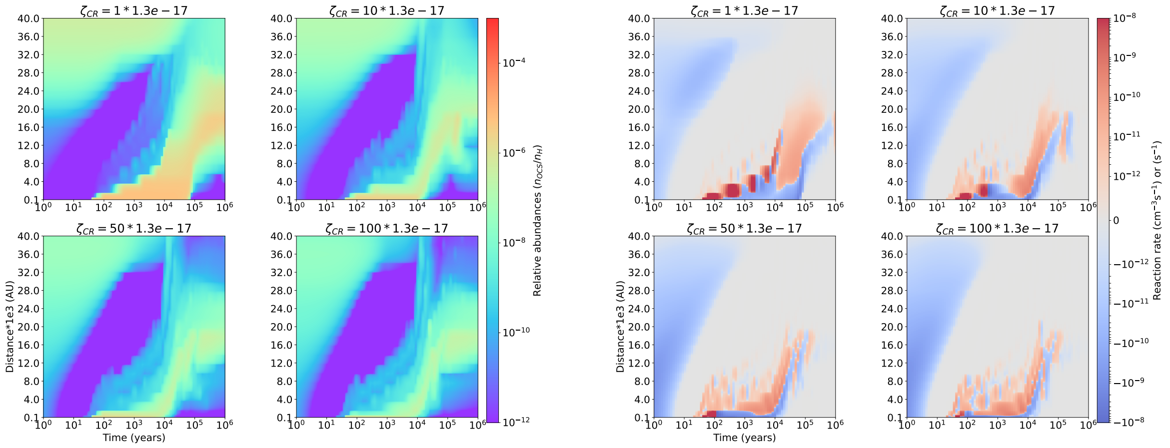

(a) (b)

Figure A.3: The relative abundances of OCS and total reaction rate of OCS as a function of time (x-axis) and distance from the center of molecular cloud (y-axis) with different cosmic rays conditions : **a. relative abundances $n_{\mathbf{OCS}}/n_{\mathbf{H}}$, b. Total reaction rate of OCS**

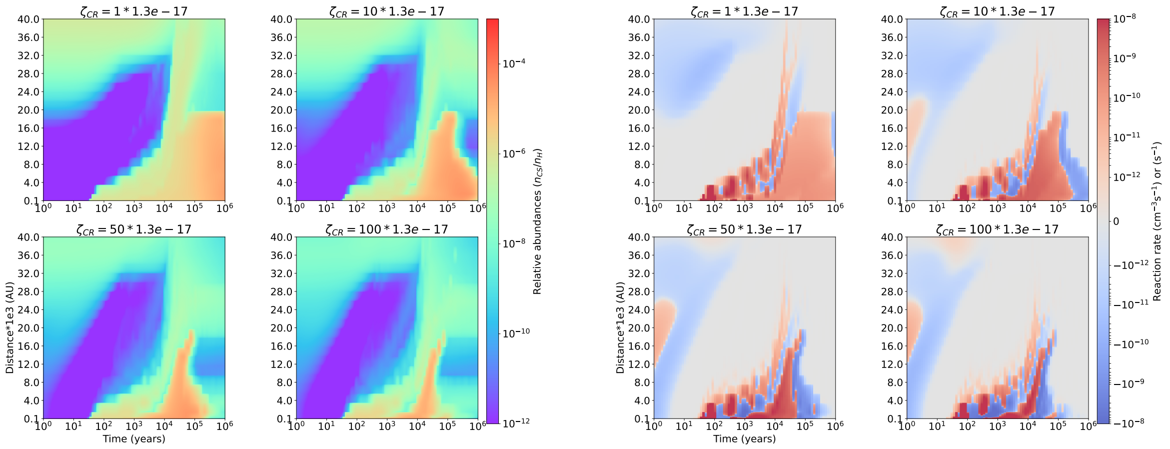

(a) (b)

Figure A.4: The relative abundances of CS and total reaction rate of CS as a function of time (x-axis) and distance from the center of molecular cloud (y-axis) with different cosmic rays conditions : **a. relative abundances $n_{\mathbf{CS}}/n_{\mathbf{H}}$, b. Total reaction rate of CS**

In the fig A.7, on the left-hand side, we notice that the relative abundance of CS molecules are decreased when we enhance the CRIR, CS molecule exist in R3 and R4 region, and it is decreasing its abundance when CRIR = ζ_{100}. On the right-hand side, we can see the destruction rate of CS is increased, the molecule is forming at around

$10^2 \rightarrow 10^4$ years, and then it is destroyed after 10^4 years

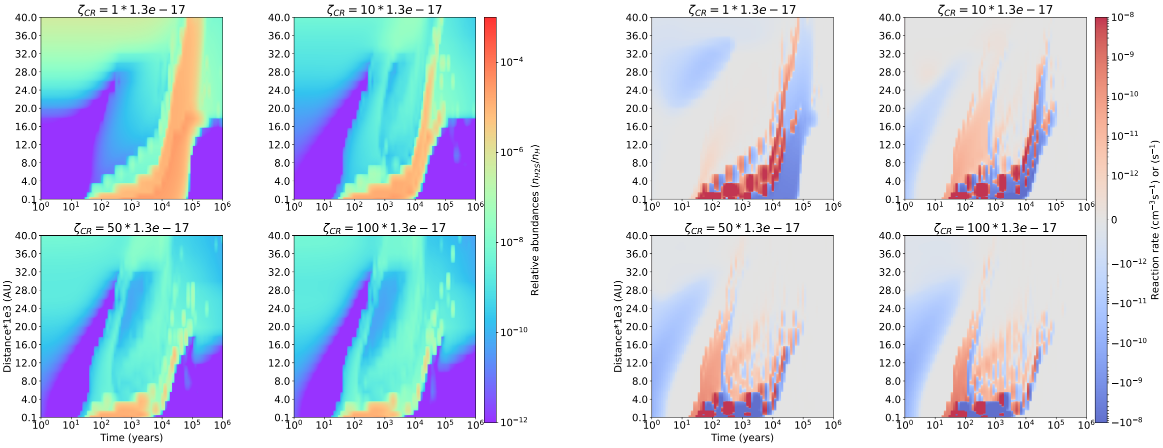

(a) (b)

Figure A.5: The relative abundances of H_2S and total reaction rate of H_2S as a function of time (x-axis) and distance from the center of molecular cloud (y-axis) with different cosmic rays conditions : **a. relative abundances $n_{\mathbf{H_2S}}/n_{\mathbf{H}}$, b. Total reaction rate of $\mathbf{H_2S}$**

In the fig A.5, on the left-hand side, we notice that the relative abundance of H_2S molecules are decreased when we enhance the CRIR, H_2S molecule exist in R3 and partially in the R4 region. It is decrease its abundance when CRIR = ζ_{100}. On the right-hand side, we can see the destruction rate of H_2S is increased, the molecule is forming at around $10^2 \rightarrow 10^4$ years, and then it is destroyed after 10^4 years

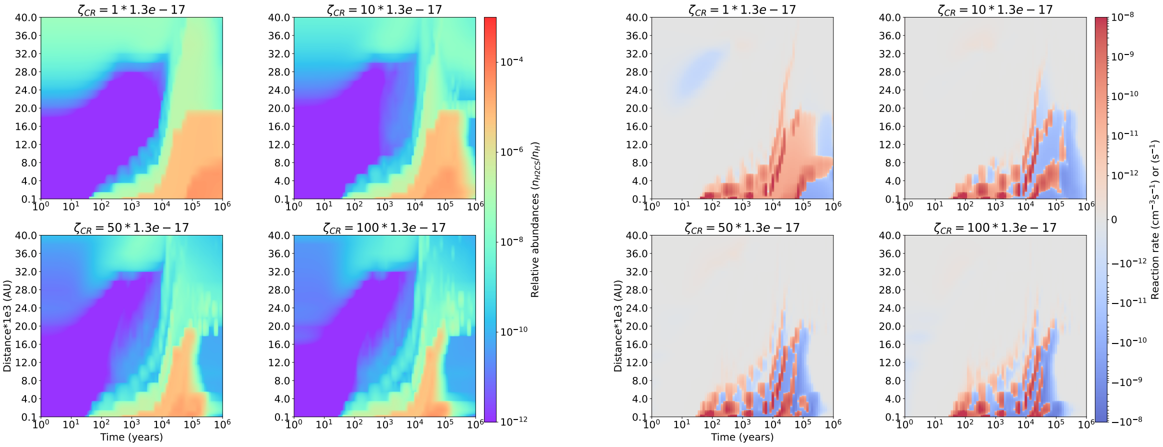

(a) (b)

Figure A.6: The relative abundances of H_2CS and total reaction rate of H_2CS as a function of time (x-axis) and distance from the center of molecular cloud (y-axis) with different cosmic rays conditions : **a. relative abundances $n_{\mathbf{H_2CS}}/n_{\mathbf{H}}$, b. Total reaction rate of $\mathbf{H_2CS}$**

In the fig A.6, on the left-hand side, we see that in case ζ_1 and ζ_10 when we increase the temperature, the abundance of H_2CS is increased, and the abundance of the molecules is decreased when we enhance the CRIR.

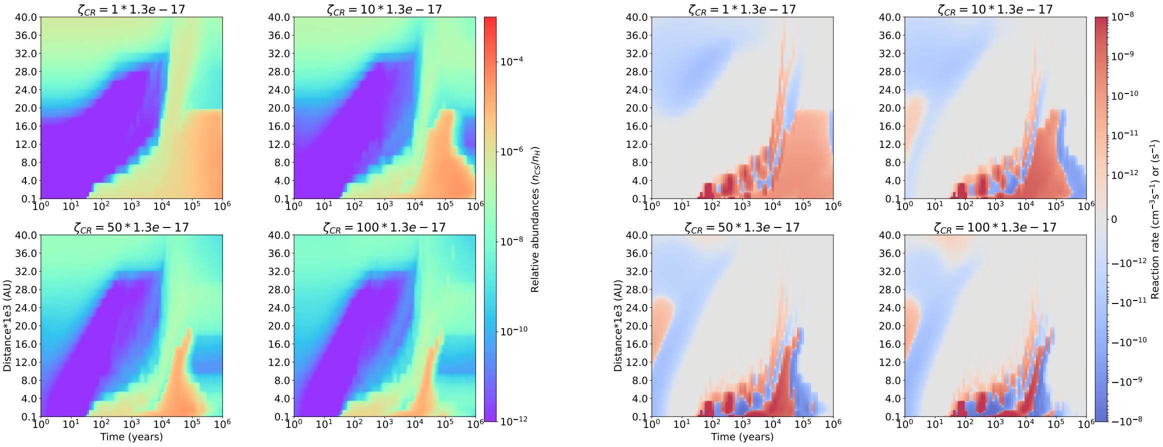

(a) (b)

Figure A.7: The relative abundances of CS and total reaction rate of CS as a function of time (x-axis) and distance from the center of molecular cloud (y-axis) with different cosmic rays conditions : **a. relative abundances $n_{\mathbf{CS}}/n_{\mathbf{H}}$, b. Total reaction rate of CS**

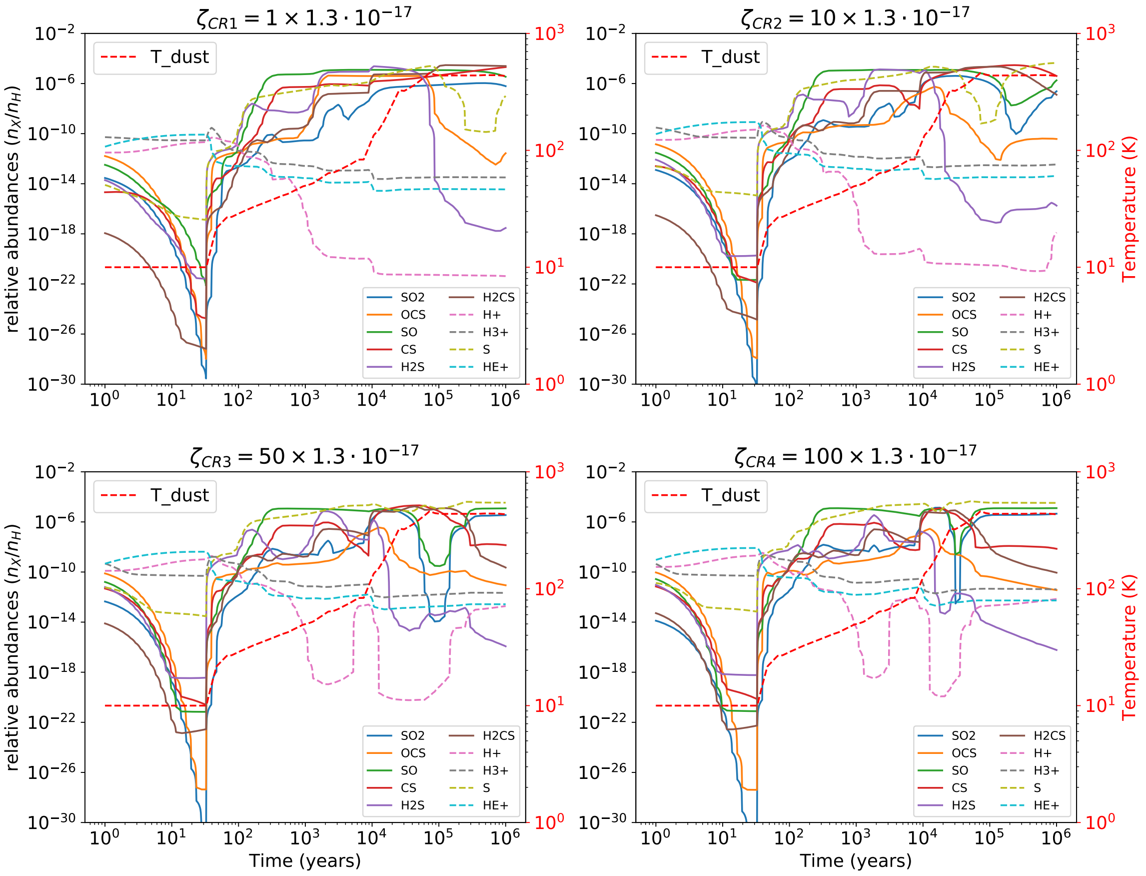

Figure A.8: Time-dependent relative abundance (with respect to H_2) at position B_1 (distant to the center = 4.058 10^3 AU) in gas-phase of S-bearing molecules. The relative abundance (left axis), time, and temperature (right axis) are plotted logarithmically.

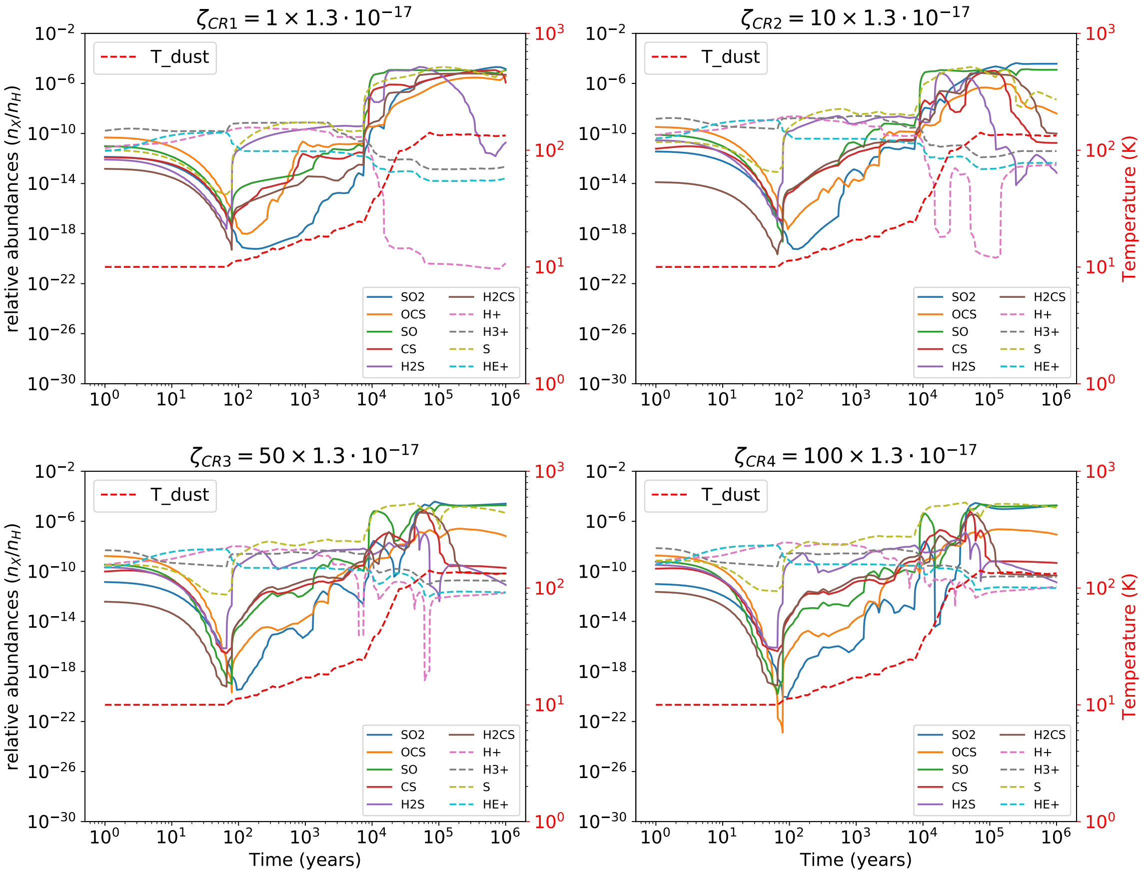
$\zeta_{CR1} = 1 \times 1.3 \cdot 10^{-17}$

$\zeta_{CR2} = 10 \times 1.3 \cdot 10^{-17}$

$\zeta_{CR3} = 50 \times 1.3 \cdot 10^{-17}$

$\zeta_{CR4} = 100 \times 1.3 \cdot 10^{-17}$

Figure A.9: Time-dependent relative abundance (with respect to H_2) at position B_2 (distant to the center = 16.315 10^3 AU) in gas-phase of S-bearing molecules. The relative abundance (left axis), time, and temperature (right axis) are plotted logarithmically.

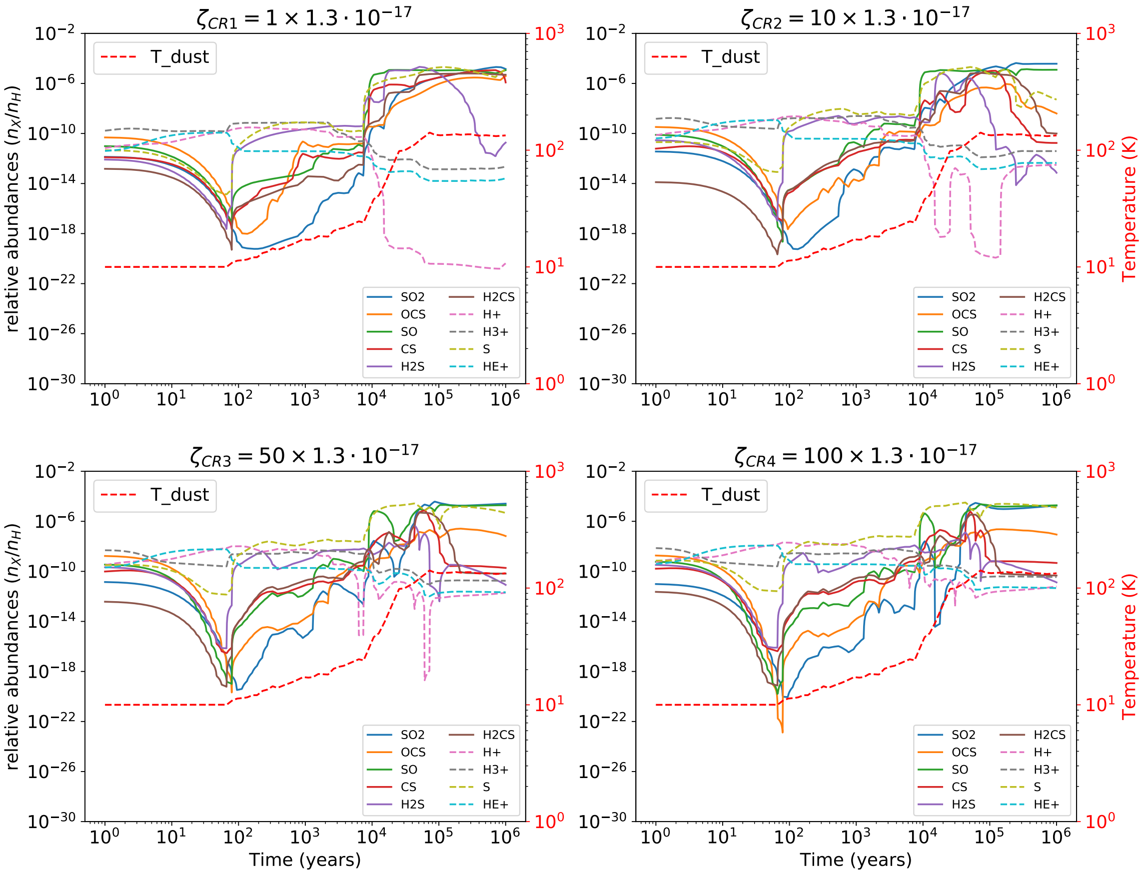

Figure A.10: Time-dependent relative abundance (with respect to H_2) at position B_3 (distant to the center $= 28.177\ 10^3$ AU) in gas-phase of S-bearing molecules. The relative abundance (left axis), time, and temperature (right axis) are plotted logarithmically.

For other molecules OCS (Fig A.3), CS (Fig A.7), H_2S (Fig A.5), H_2CS (Fig A.6)

Under weak CRIR CR1, the molecules forming reaction in the time between $10^5 - 10^6$ years and the region $< 8 \times 10^3$ AU, which can be explained because in this region there is high temperature (> 100 K) makes the precursor's S-bearing species like S, $HOCS^+$, HCS, OCS^+… to decompose to create other molecules. Unlike the case of SO_2, the reaction rate depends only on two reactions. The total reaction rate of the molecules depends on the many reactions. Therefore, they depend on the abundances of molecules such as H_3^+, HCO^+, S, $HOCS^+$, HCS, OCS^+…. Similar formation and destruction of SO_2, with adsorption and desorption, are a significant influence. Since after 10^4 years, all molecules on the grain surface evaporated to the gas phase. After 10^4 years, these reactions reached equilibrium, and due to the rate coefficient, which strongly depends on temperature, so when the temperature increases, the reaction rate of these two reactions increases. Both are reversible and do not affect the total reaction rate.

A.2 Influence of density

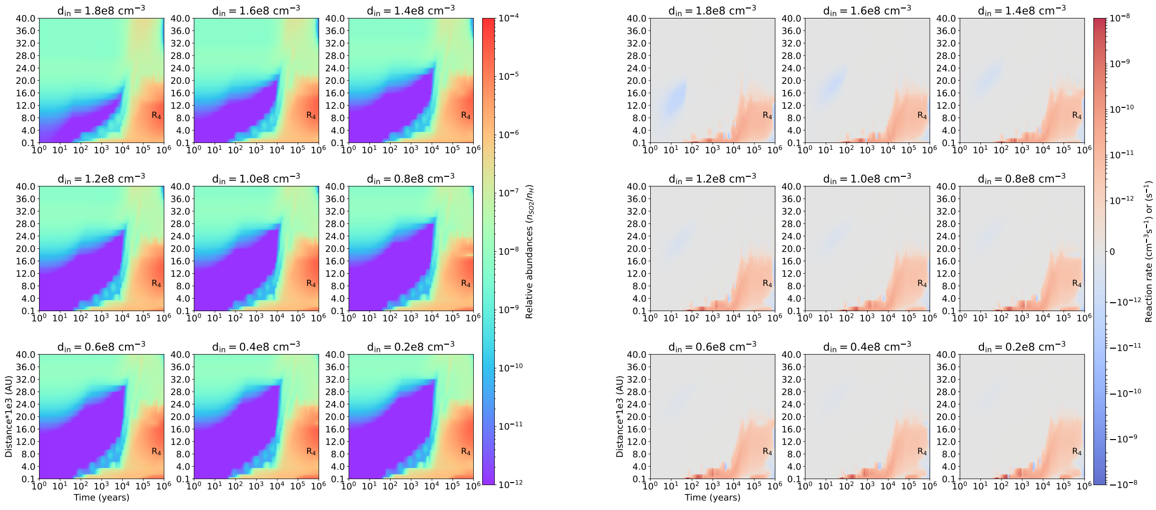

(a) (b)

Figure A.11: The relative abundances of SO_2 and total reaction rate of SO_2 as a function of time (x-axis) and distance from the center of molecular cloud (y-axis) in different inner density of molecular cloud: **a. relative abundances $n_{\mathbf{SO_2}}/n_{\mathbf{H}}$, b. Total reaction rate of $\mathbf{SO_2}$**

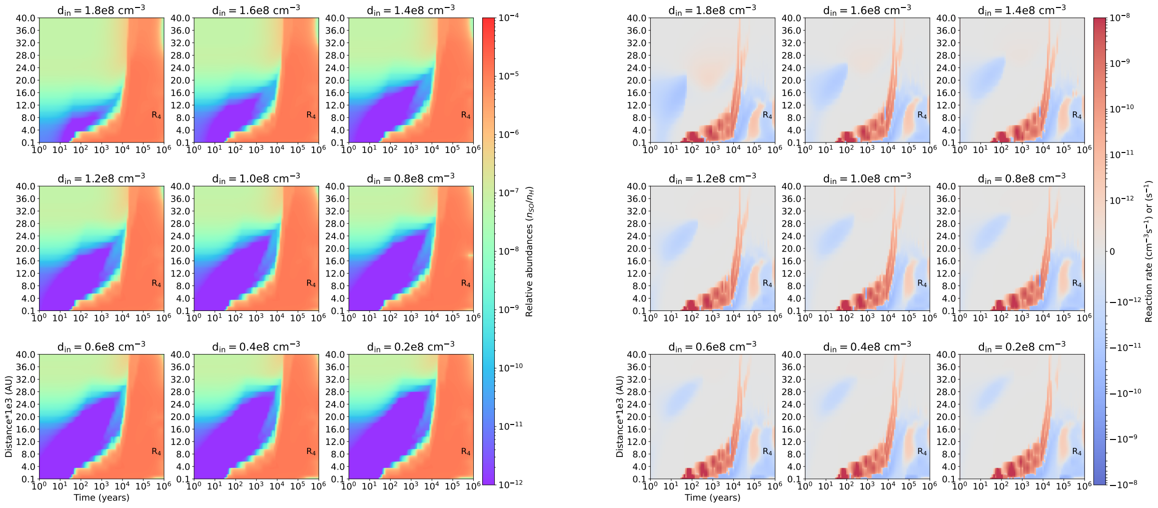

(a) (b)

Figure A.12: The relative abundances of SO and total reaction rate of SO as a function of time (x-axis) and distance from the center of molecular cloud (y-axis) in different inner density of molecular cloud: **a. relative abundances $n_{\mathbf{SO}}/n_{\mathbf{H}}$, b. Total reaction rate of SO**

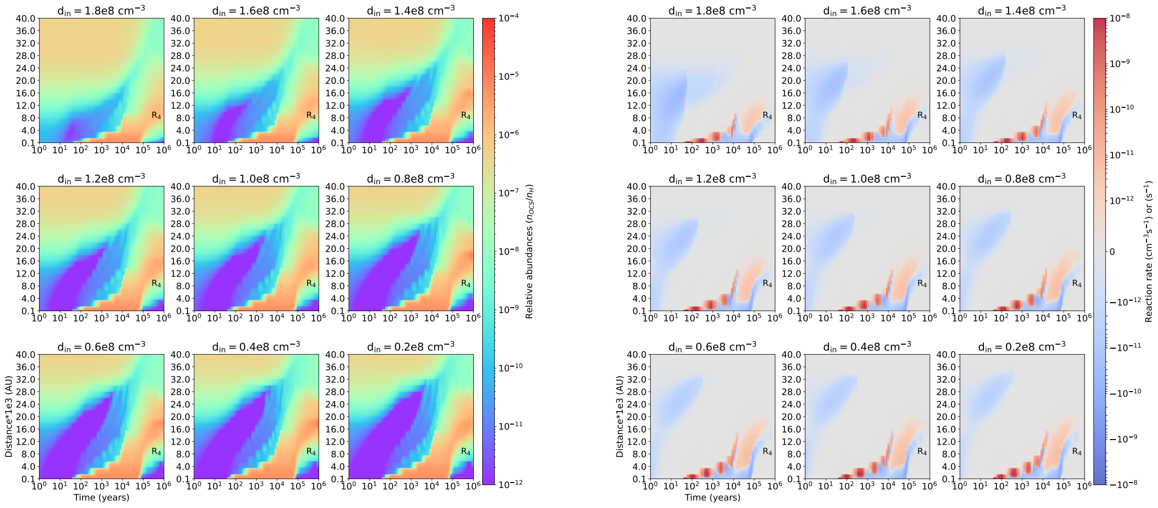

(a) (b)

Figure A.13: The relative abundances of OCS and total reaction rate of OCS as a function of time (x-axis) and distance from the center of molecular cloud (y-axis) in different inner density of molecular cloud: **a. relative abundances $n_{\mathbf{OCS}}/n_{\mathbf{H}}$, b. Total reaction rate of OCS**

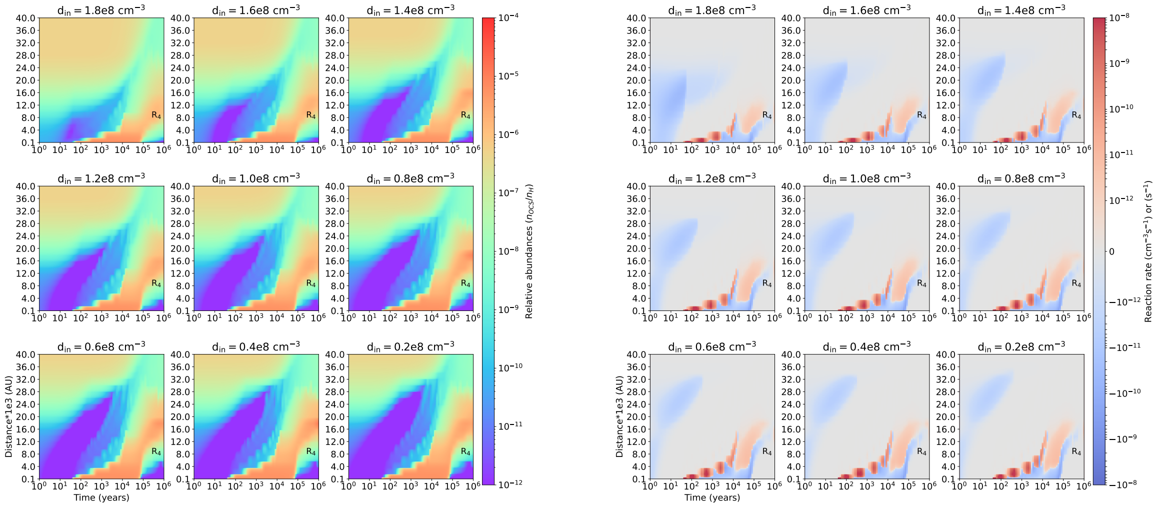

(a) (b)

Figure A.14: The relative abundances of OCS and total reaction rate of OCS as a function of time (x-axis) and distance from the center of molecular cloud (y-axis) in different inner density of molecular cloud: **a. relative abundances $n_{\mathbf{OCS}}/n_{\mathbf{H}}$, b. Total reaction rate of OCS**

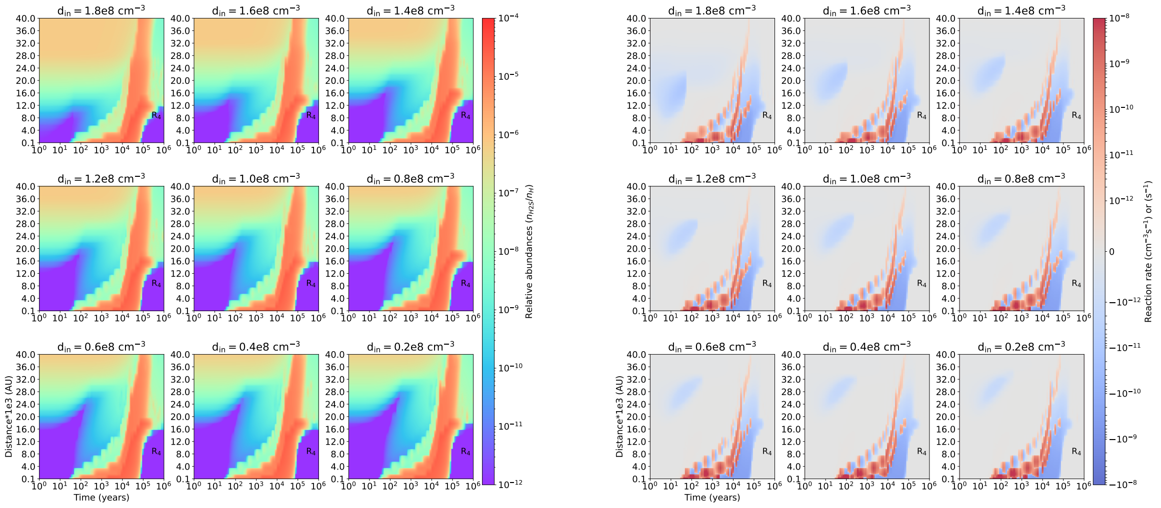

(a) (b)

Figure A.15: The relative abundances of H_2S and total reaction rate of H_2CS as a function of time (x-axis) and distance from the center of molecular cloud (y-axis) in different inner density of molecular cloud: **a. relative abundances $n_{\mathbf{H_2CS}}/n_{\mathbf{H}}$, b. Total reaction rate of $\mathbf{H_2S}$**

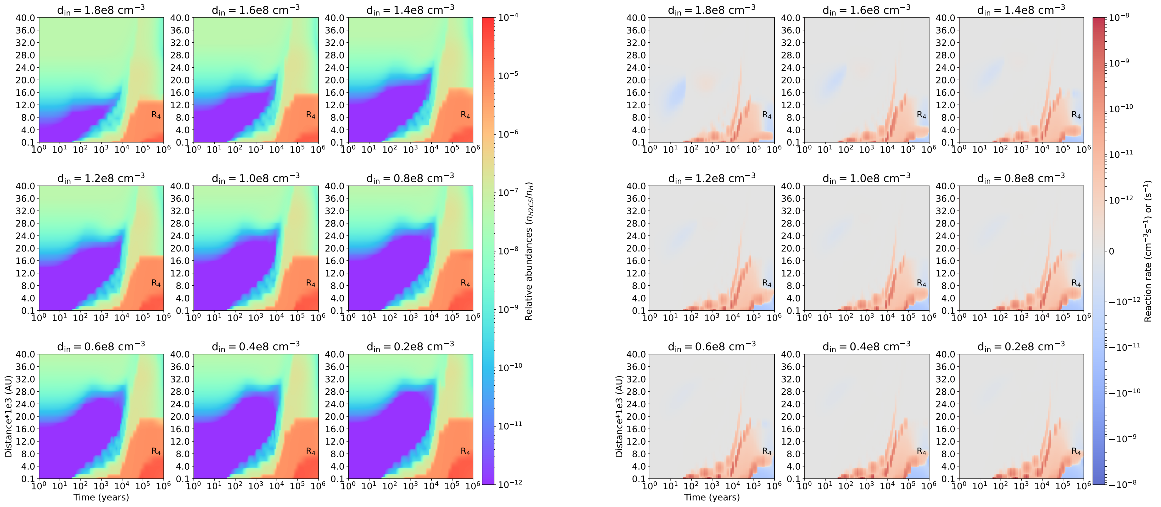

(a) (b)

Figure A.16: The relative abundances of H_2CS and total reaction rate of H_2CS as a function of time (x-axis) and distance from the center of molecular cloud (y-axis) in different inner density of molecular cloud: **a. relative abundances** $n_{\mathbf{H_2CS}}/n_{\mathbf{H}}$, **b. Total reaction rate of** $\mathbf{H_2CS}$

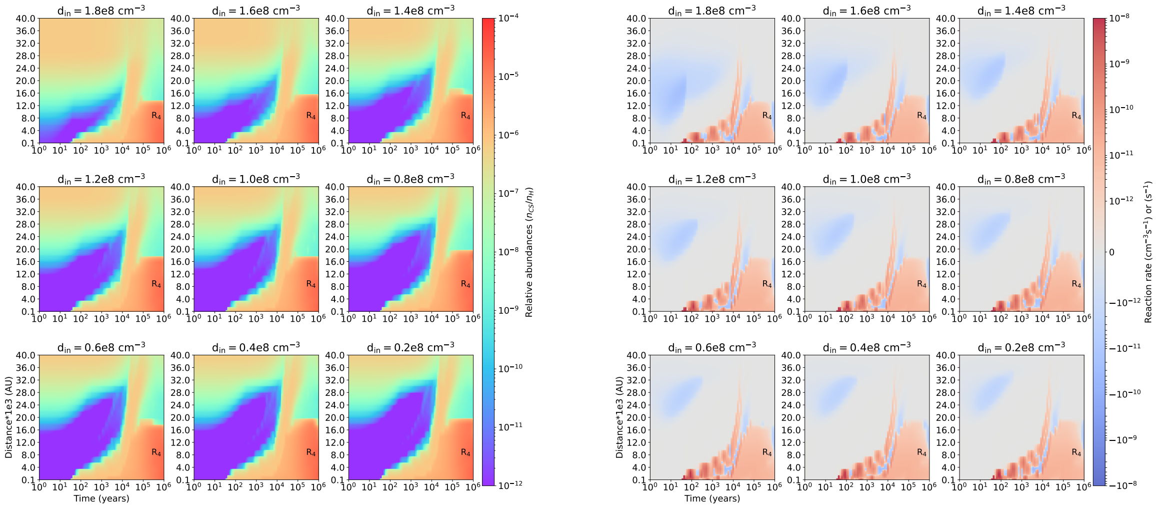

(a) (b)

Figure A.17: The relative abundances of CS and total reaction rate of CS as a function of time (x-axis) and distance from the center of molecular cloud (y-axis) in different inner density of molecular cloud: **a. relative abundances** $n_{\mathbf{CS}}/n_{\mathbf{H}}$, **b. Total reaction rate of CS**

A.3 Influence of density distribution of the molecular cloud

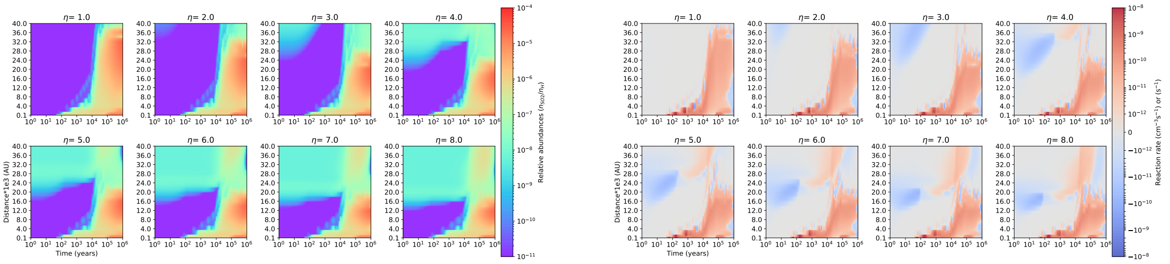

(a) (b)

Figure A.18: The relative abundances of SO_2 and total reaction rate of SO_2 as a function of time (x-axis) and distance from the center of molecular cloud (y-axis) in different Plummer function (η): **a. relative abundances $n_{\mathbf{SO_2}}/n_{\mathbf{H}}$, b. Total reaction rate of $\mathbf{SO_2}$**

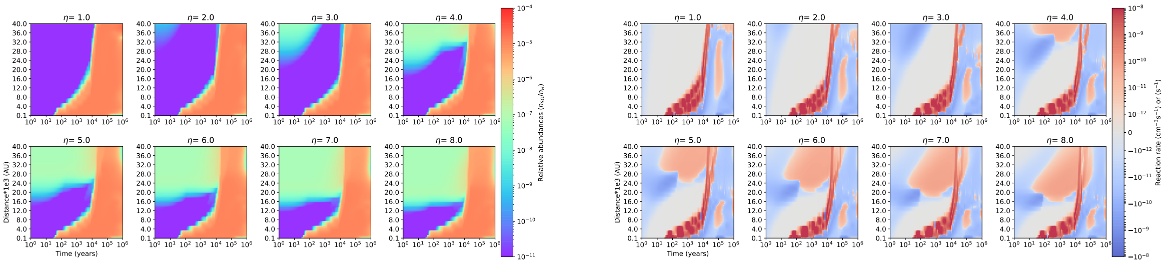

(a) (b)

Figure A.19: The relative abundances of SO and total reaction rate of SO as a function of time (x-axis) and distance from the center of molecular cloud (y-axis) in different Plummer function (η): **a. relative abundances $n_{\mathbf{SO}}/n_{\mathbf{H}}$, b. Total reaction rate of SO**

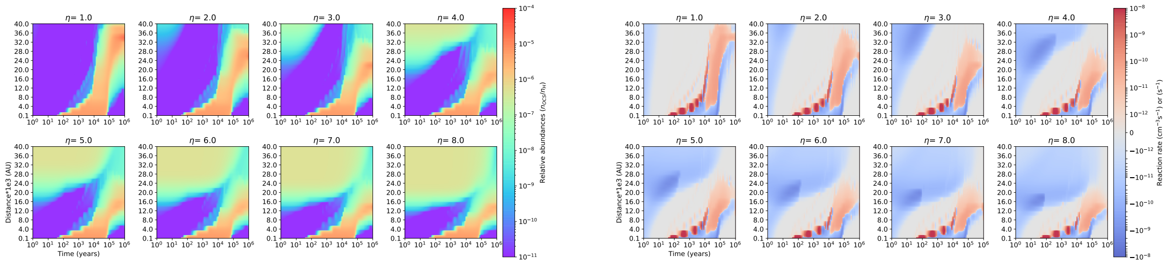

(a) (b)

Figure A.20: The relative abundances of OCS and total reaction rate of OCS as a function of time (x-axis) and distance from the center of molecular cloud (y-axis) in different Plummer function (η): **a. relative abundances** $n_{\mathbf{OCS}}/n_{\mathbf{H}}$ **, b. Total reaction rate of OCS**

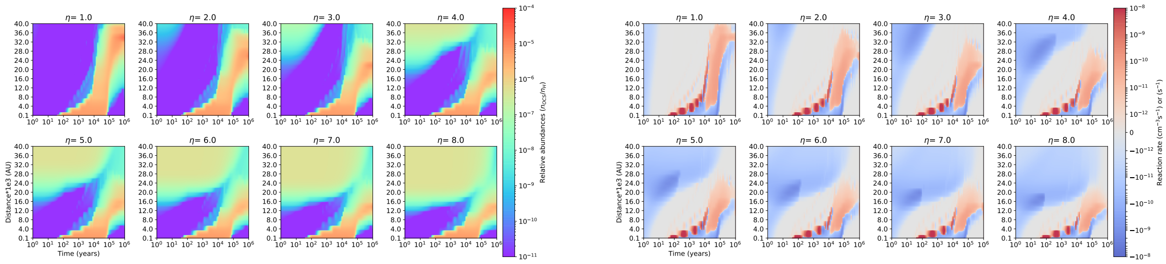

(a) (b)

Figure A.21: The relative abundances of OCS and total reaction rate of OCS as a function of time (x-axis) and distance from the center of molecular cloud (y-axis) in different Plummer function (η): **a. relative abundances** $n_{\mathbf{OCS}}/n_{\mathbf{H}}$ **, b. Total reaction rate of OCS**

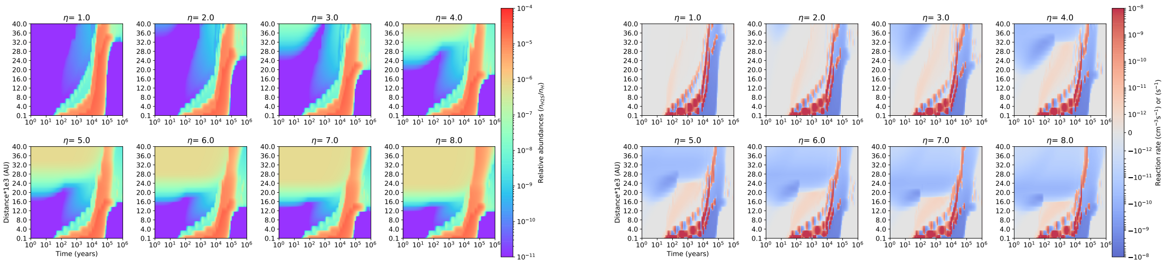

(a) (b)

Figure A.22: The relative abundances of H_2S and total reaction rate of H_2CS as a function of time (x-axis) and distance from the center of molecular cloud (y-axis) in different Plummer function (η): **a. relative abundances $n_{\mathbf{H_2CS}}/n_{\mathbf{H}}$, b. Total reaction rate of $\mathbf{H_2S}$**

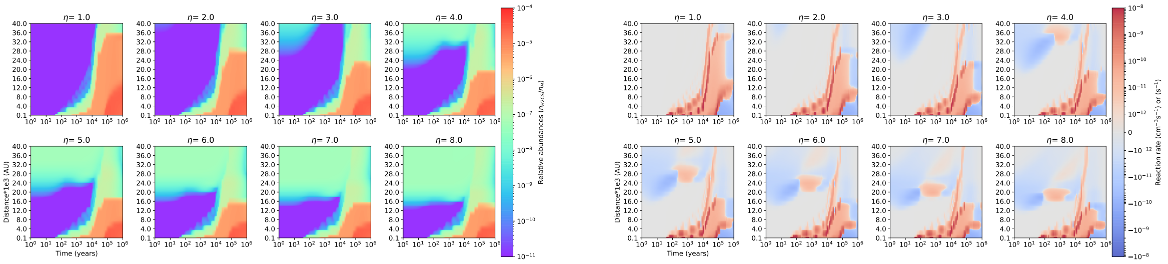

(a) (b)

Figure A.23: The relative abundances of H_2CS and total reaction rate of H_2CS as a function of time (x-axis) and distance from the center of molecular cloud (y-axis) in different Plummer function (η): **a. relative abundances $n_{\mathbf{H_2CS}}/n_{\mathbf{H}}$, b. Total reaction rate of $\mathbf{H_2CS}$**

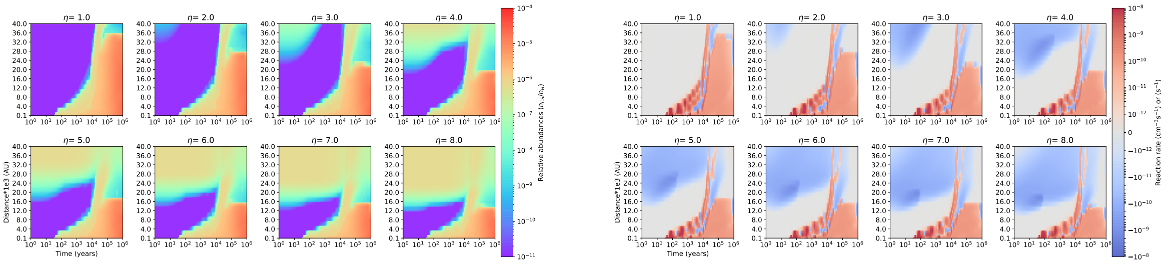

(a) (b)

Figure A.24: The relative abundances of CS and total reaction rate of CS as a function of time (x-axis) and distance from the center of molecular cloud (y-axis) in different Plummer function (η): **a. relative abundances $n_{\mathbf{CS}}/n_{\mathbf{H}}$, b. Total reaction rate of CS**

A.4 Influence of thermal evolution of the cloud

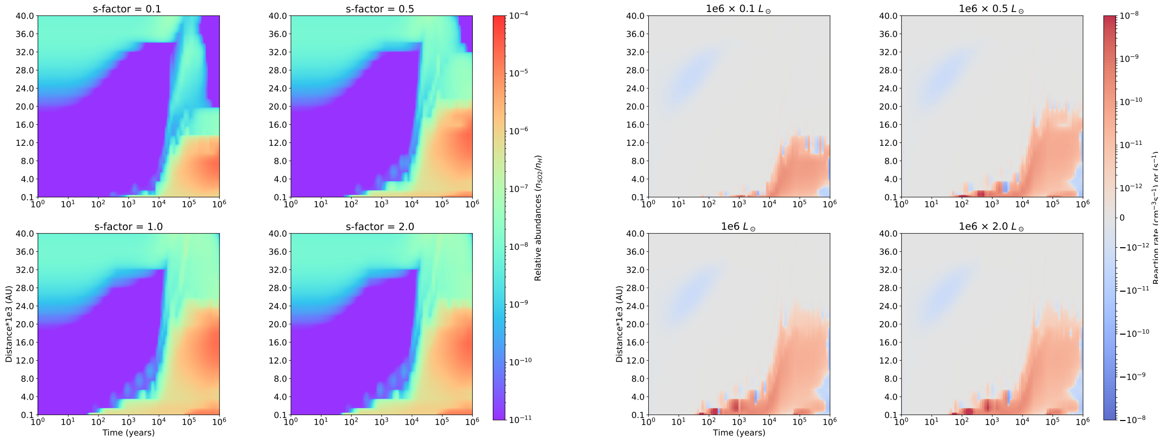

(a) (b)

Figure A.25: The relative abundances of SO_2 and total reaction rate of SO_2 as a function of time (x-axis) and distance from the center of molecular cloud (y-axis) in different thermal evolution condition: **a. relative abundances** $n_{\mathbf{SO_2}}/n_{\mathbf{H}}$, **b. Total reaction rate of** $\mathbf{SO_2}$

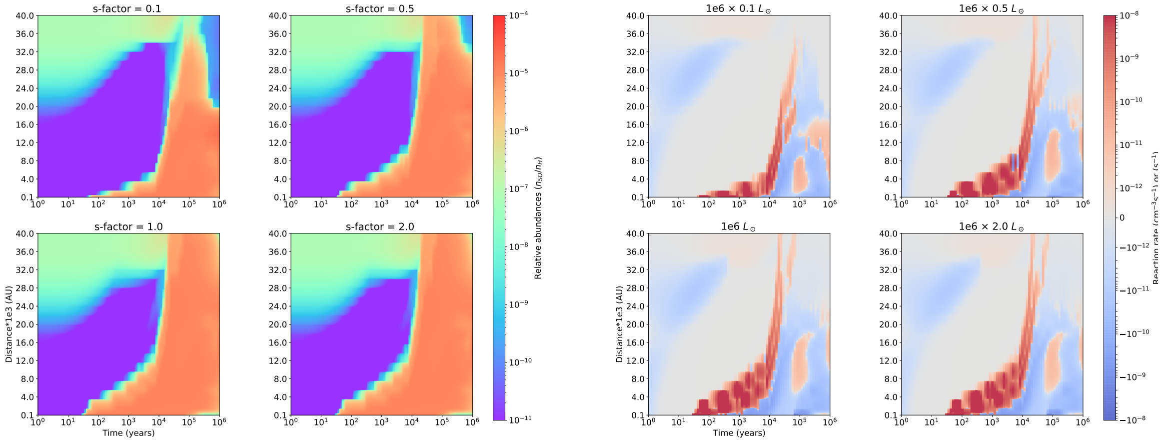

(a) (b)

Figure A.26: The relative abundances of SO and total reaction rate of SO as a function of time (x-axis) and distance from the center of molecular cloud (y-axis) in different thermal evolution condition: **a. relative abundances** $n_{\mathbf{SO}}/n_{\mathbf{H}}$, **b. Total reaction rate of SO**

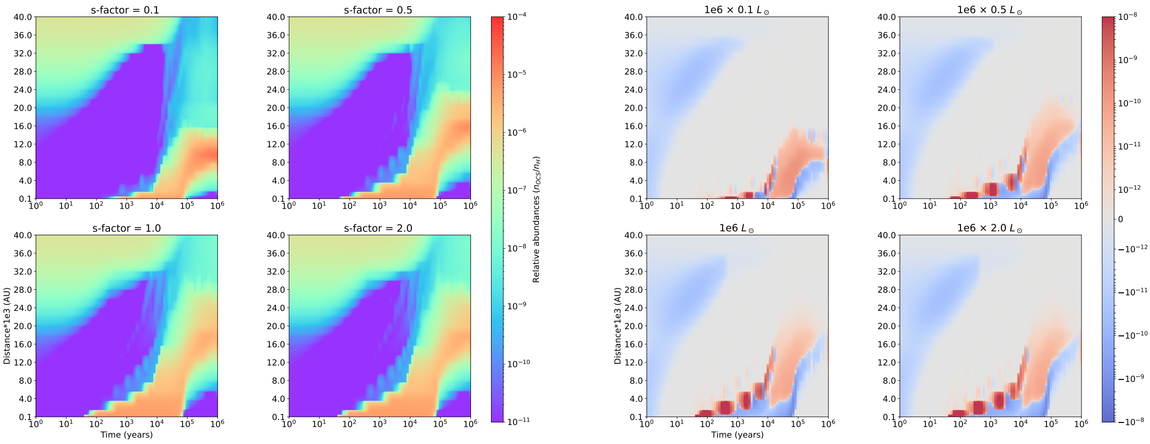

(a) (b)

Figure A.27: The relative abundances of OCS and total reaction rate of OCS as a function of time (x-axis) and distance from the center of molecular cloud (y-axis) in different thermal evolution condition: **a. relative abundances $n_{\mathbf{OCS}}/n_{\mathbf{H}}$, b. Total reaction rate of OCS**

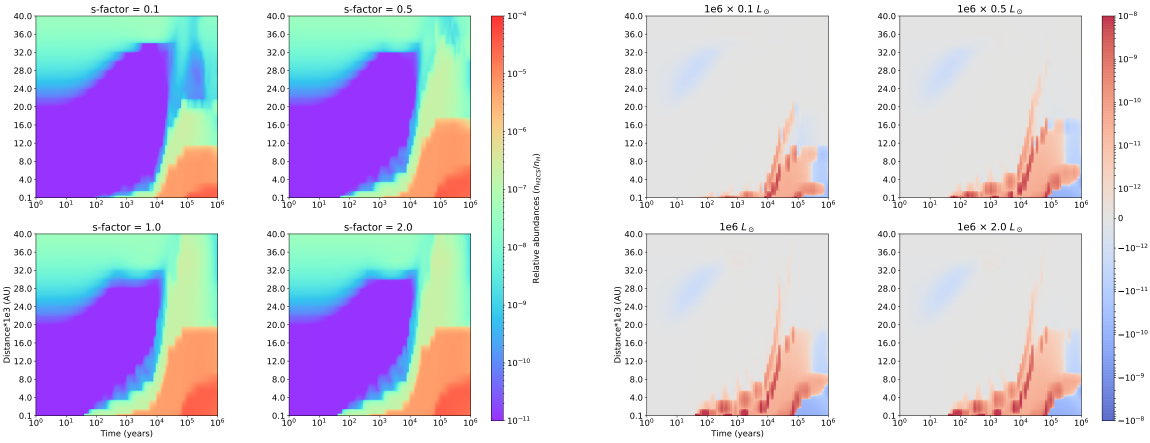

(a) (b)

Figure A.28: The relative abundances of H_2CS and total reaction rate of H_2CS as a function of time (x-axis) and distance from the center of molecular cloud (y-axis) in different thermal evolution condition: **a. relative abundances $n_{\mathbf{H_2CS}}/n_{\mathbf{H}}$, b. Total reaction rate of H_2CS**

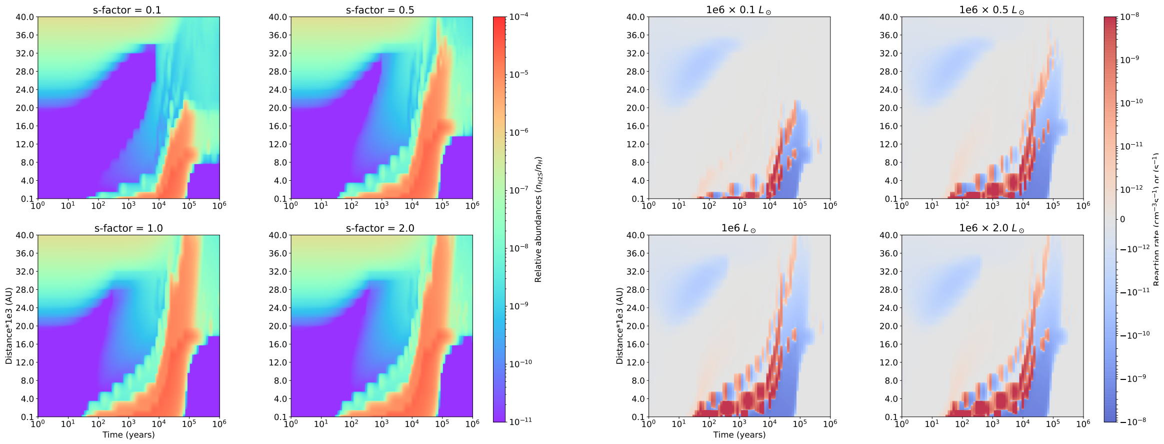

(a) (b)

Figure A.29: The relative abundances of CS and total reaction rate of CS as a function of time (x-axis) and distance from the center of molecular cloud (y-axis) in different thermal evolution condition: **a. relative abundances $\mathbf{n_{H_2S}/n_H}$, b. Total reaction rate of $\mathbf{H_2S}$**

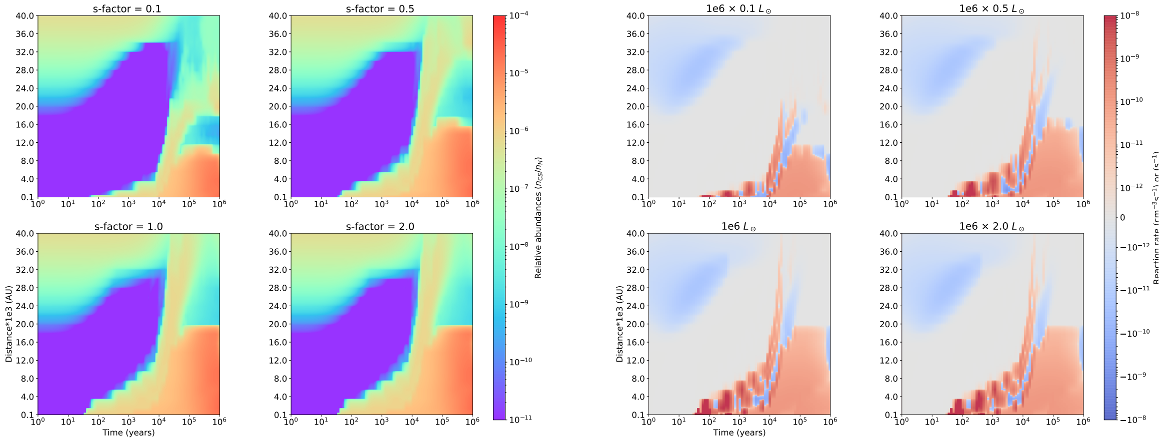

(a) (b)

Figure A.30: The relative abundances of CS and total reaction rate of CS as a function of time (x-axis) and distance from the center of molecular cloud (y-axis) in different thermal evolution condition: **a. relative abundances $\mathbf{n_{CS}/n_H}$, b. Total reaction rate of CS**

Appendix B

Comparision data vs astrochemical model

B.1 CS vs SO_2

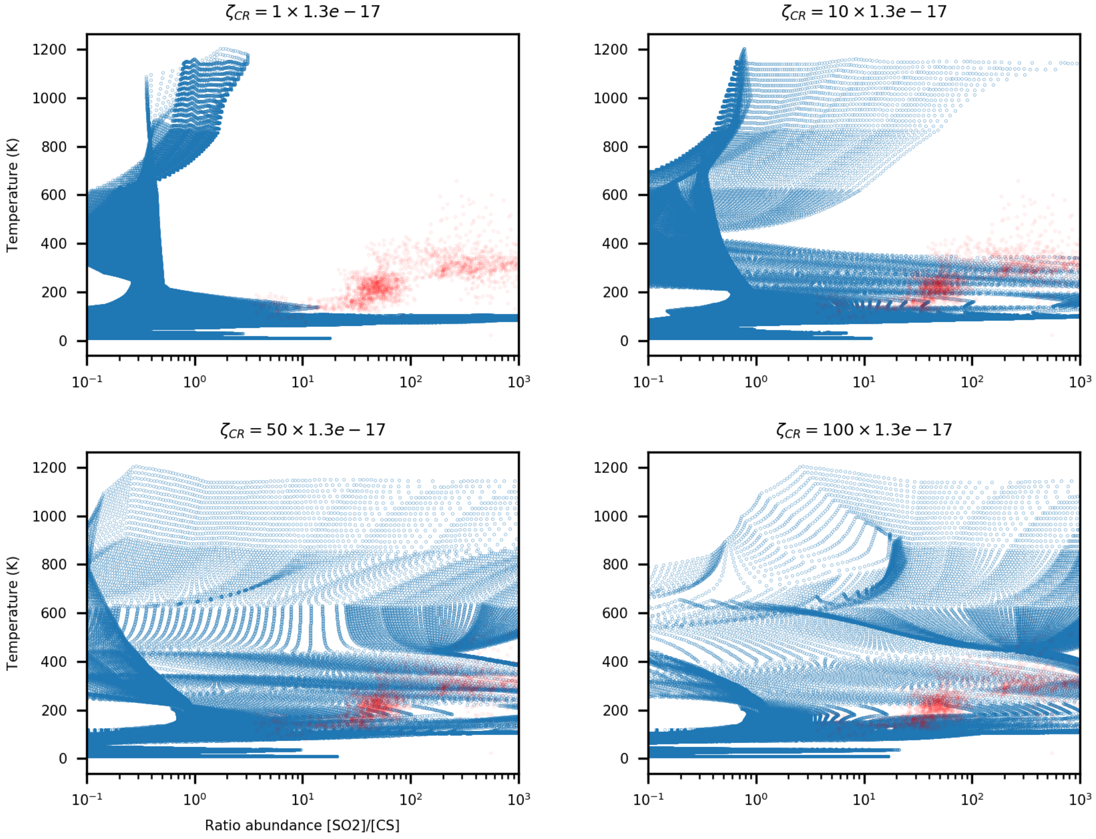

Figure B.1: The comparison observational results (red dots) and astrochemistry models (blue dots) of CS and SO_2 in difference cosmic-ray ionization rate condition

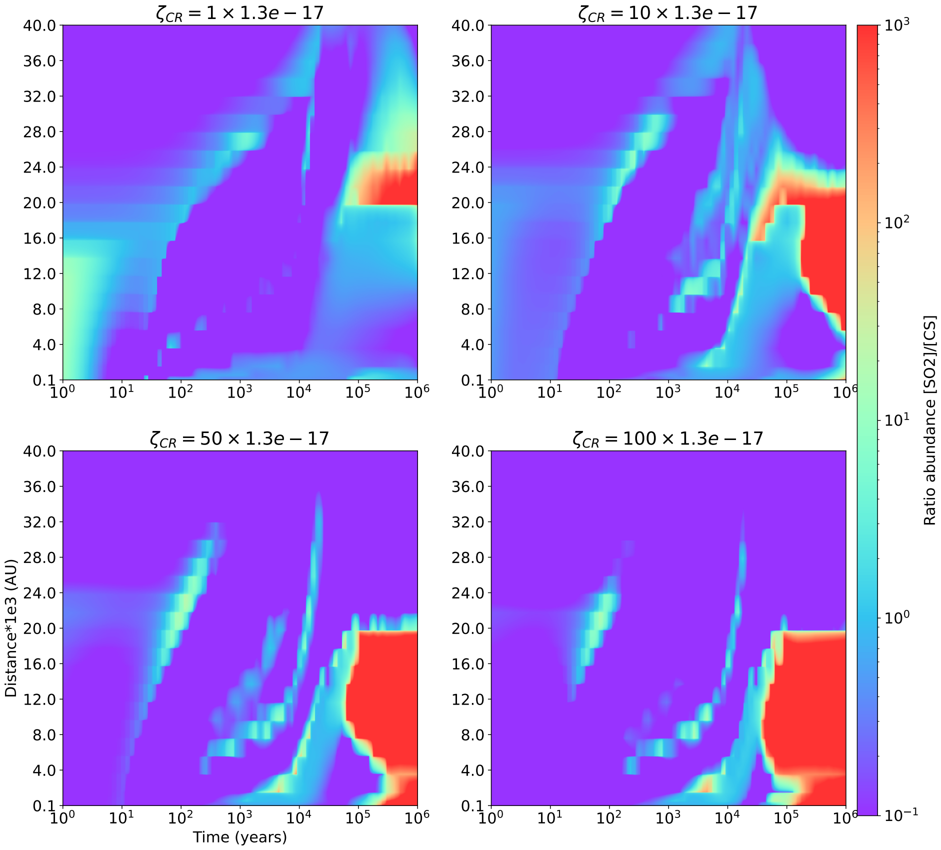

Figure B.2: The abundances ratio of CS and SO_2 in difference cosmic-ray ionization rate condition

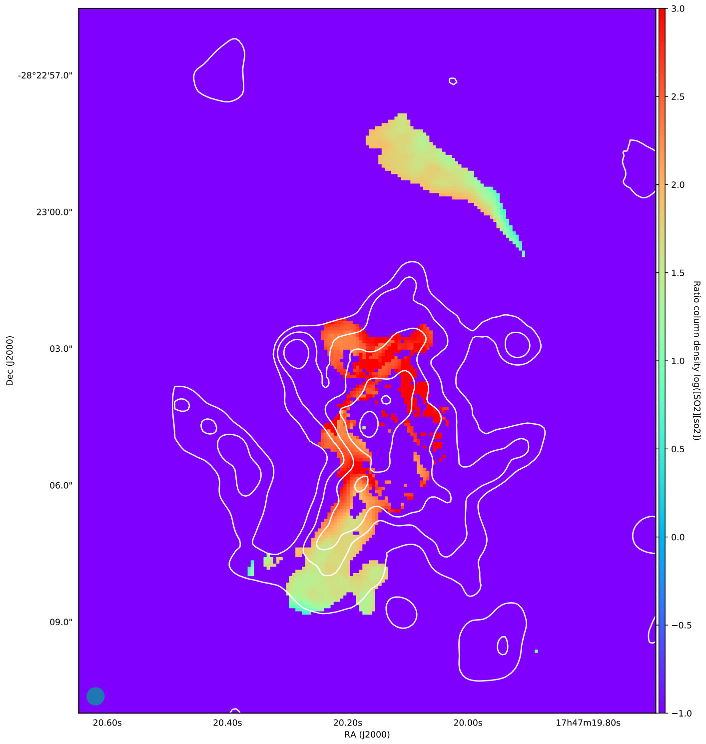

Figure B.3: The spatial abundances ratio of CS and SO_2 in Sgr B2 (Main)

Figure B.2 shows the changing of abundance ratio of $[SO_2]/[CS]$ in cosmic rays conditions, the enhancement of CRIR lead to the ratio of $[SO_2]/[CS]$ enhance. In addition, Figure B.3 shows the spatial distribution of the ratio $[SO_2]/[CS]$ in Sgr B2 (M), which shows how the ratio change in the whole Sgr B2(M).

Figure B.1 shows the comparison of abundance ratio of $[SO_2]/[CS]$ in observation and simulation results. the figure shows how consistent the results are when we enhance CRIR.

B.2 H_2CS vs SO_2

Thioformaldehyde H_2CS molecules are found in the core, where is the warm region. In agreement with Sgr B2(M) (Möller et al., 2021), they found a single warm component, and they have not seen any low-temperature contribution of H_2CS, as described by (Belloche et al., 2013).

In the case of H_2CS, the observation results are in the simulation results in CR10, CR50, and CR100, and we can conclude that the observational results are consistent with the modeling results. However, the number of observational results is less, and most of them concentrate in the southern and next to the hot core.

By comparing the observational results and simulation, we see that only the case CR10 results are compatible with the simulation. At the last time step (t $\sim 10^6$ years), the ratio of $[SO_2]/[H_2CS]$ are high (around 10 - 100) and agreeable to the observational results. Nevertheless, in the case CR50 and CR100, the ratios are higher ($> 10^3$) and higher than the observational results.

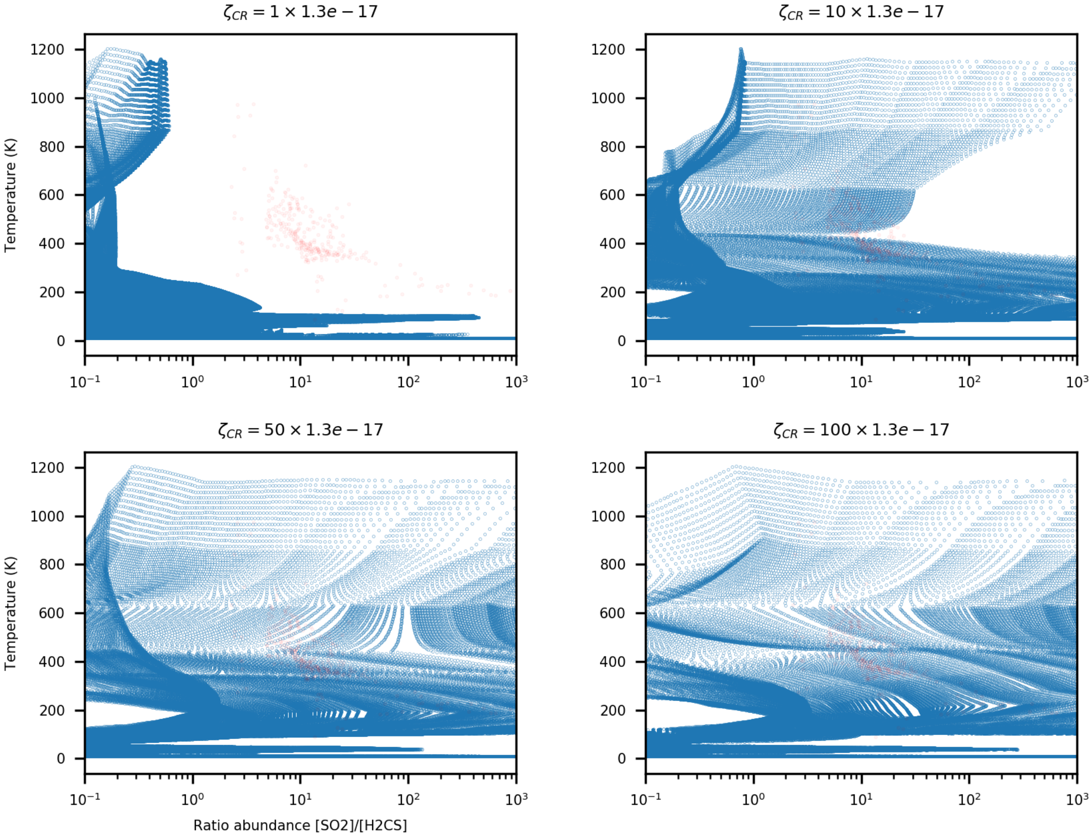

Figure B.4: The comparison observational results (red dots) and astrochemistry models (blue dots) of H_2CS and SO_2 in difference cosmic-ray ionization rate condition

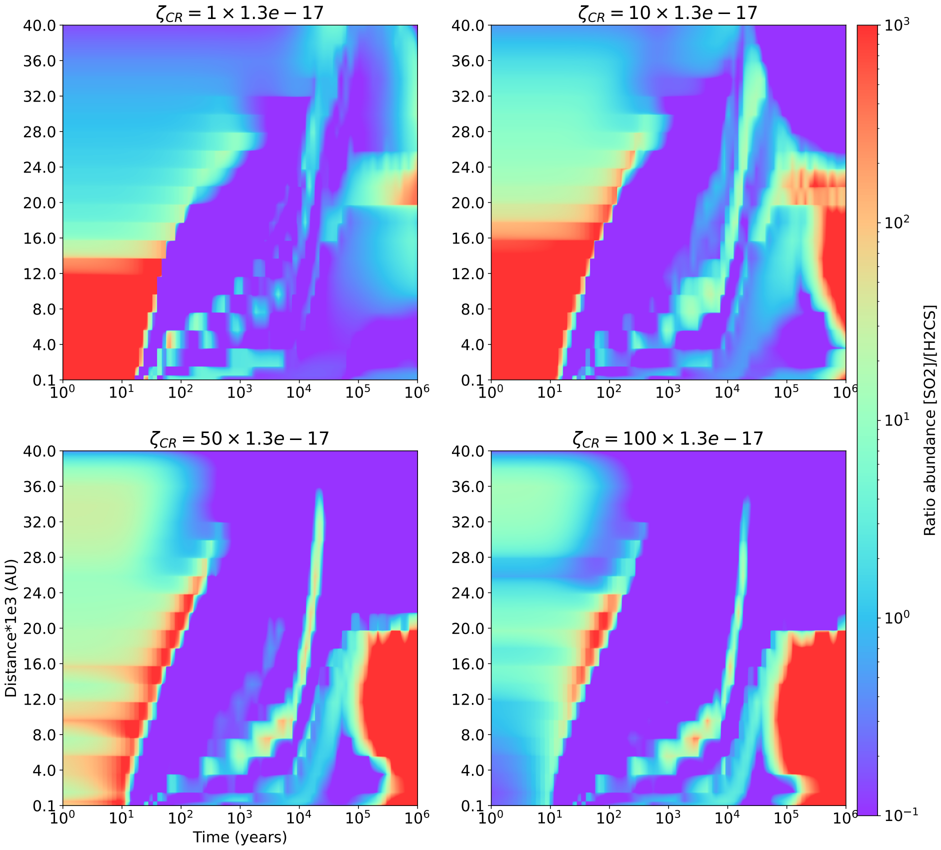

Figure B.5: The abundances ratio of H_2CS and SO_2 in difference cosmic-ray ionization rate condition

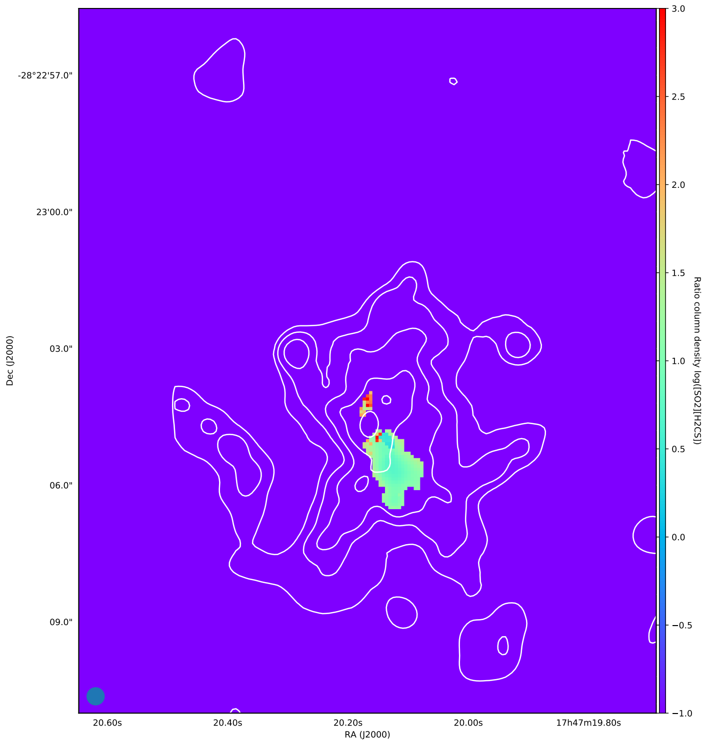

Figure B.6: The spatial abundances ratio of H_2CS and SO_2 in Sgr B2 (Main)

Figure B.5 shows the changing of abundance ratio of $[SO_2]/[H_2CS]$ in cosmic rays conditions, the enhancement of CRIR lead to the ratio of $[SO_2]/[H_2CS]$ enhance. In addition, Figure B.6 shows the spatial distribution of the ratio $[SO_2]/[H_2CS]$ in Sgr B2 (M), which shows how the ratio change in the whole Sgr B2(M).

Figure B.1 shows the comparison of abundance ratio of $[SO_2]/[CS]$ in observation and simulation results. the figure shows how consistent the results are when we enhance CRIR.

B.3 H_2S vs SO_2

Hydrogen sulfide H_2S molecules are found in the cloud, which is in agreement with (Möller et al., 2021), they found line emission and absorption of H_2S molecule and its isotopologues. Still, they are self-absorption and weakly detected.

In the case of H_2S, the observation results are in the simulation results in CR1. However, by comparing the observational results and simulation, we see that only the outer part of the simulation results is consistent with the observational results. Moreover, from the previous comparison (SO, OCS, CS, and H_2CS), we conclude that the CR10 condition is agreeable to the observation. So, we should move to the case CR10 condition. In CR10 condition, the ratio of $[SO_2]/[H_2S]$ in observation is consistent with the simulation only at the temperature < 200 K. Since the number of lines of H_2S in the given frequency range (ALMA band 6) is only two lines, and most of them are blended by other molecules in the center (high temperature), and self-absorption , which makes it hard to make reliable estimates. The blended of the molecules lead to inconsistent observation and simulation results in the high temperature.

Figure B.8 shows the changing of abundance ratio of [SO_2]/[H2S] in cosmic rays conditions, the enhancement of CRIR lead to the ratio of [SO_2]/[H2S] enhance. In addition, Figure B.9 shows the spatial distribution of the ratio [SO_2]/[H2S] in Sgr B2 (M), which shows how the ratio change in the whole Sgr B2(M).

Figure B.7 shows the comparison of abundance ratio of [SO_2]/[H2S] in observation and simulation results. the figure shows how consistent the results are when we enhance CRIR.

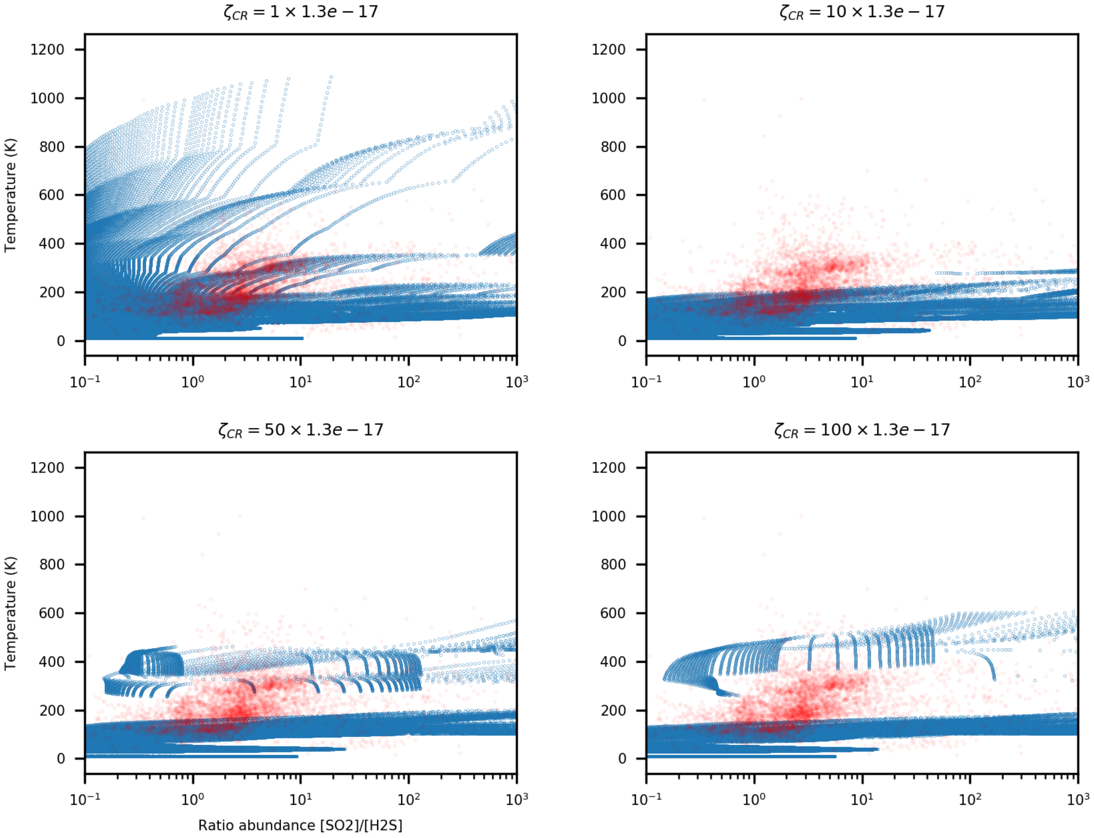

Figure B.7: The comparison observational results (red dots) and astrochemistry models (blue dots) of H_2S and SO_2 in difference cosmic-ray ionization rate condition

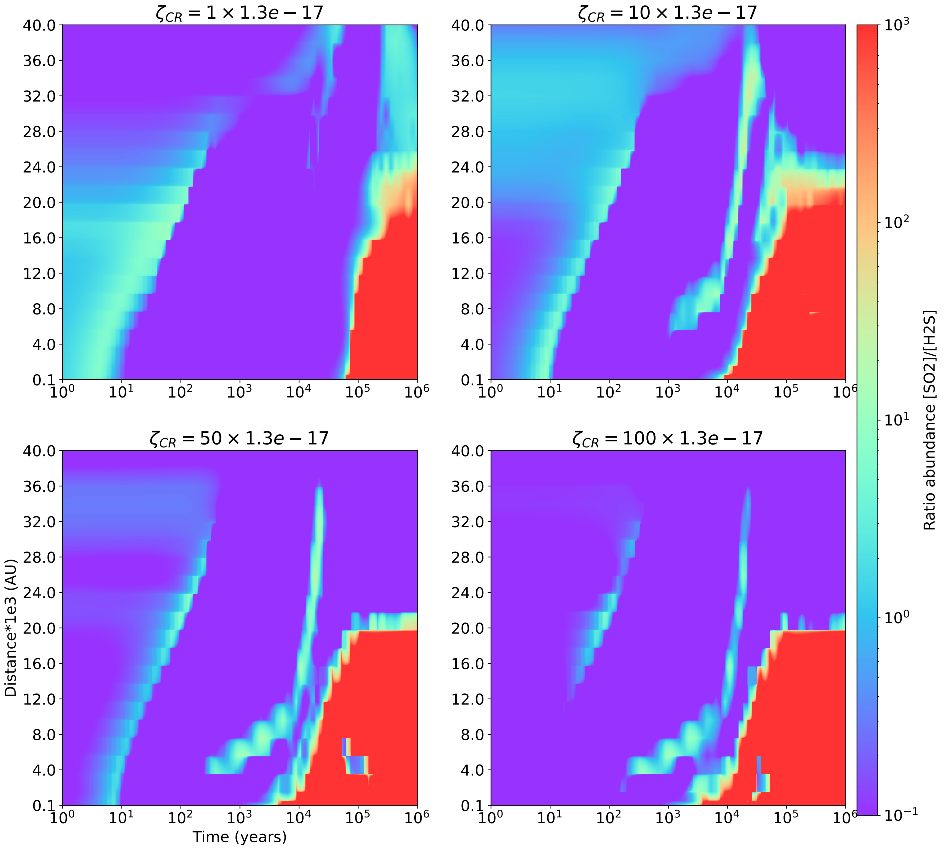

Figure B.8: The abundances ratio of H_2S and SO_2 in difference cosmic-ray ionization rate condition

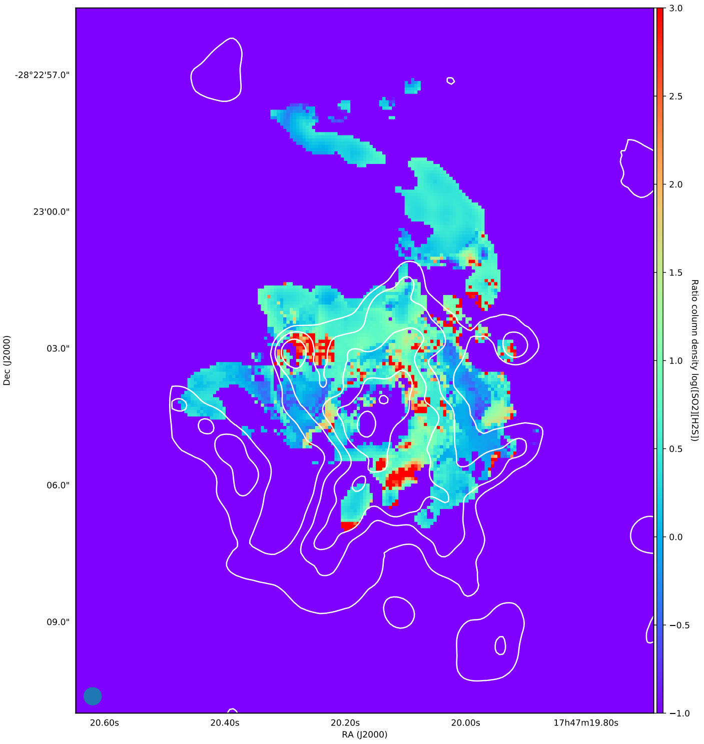

Figure B.9: The spatial abundances ratio of H_2S and SO_2 in Sgr B2 (Main)